Mechanisms responsible for asymmetric aurora between the conjugate hemispheres

Jone Peter Reistad

Dissertation for the degree of Philosophiae Doctor (PhD)

Department of Physics and Technology
University of Bergen

April 2016

Preface

This synthesis and collection of papers are submitted for the degree of philosophiae doctor (PhD) in physics at the Department of Physics and Technology, University of Bergen.

The thesis is divided into an introductory part and a part consisting of four papers published/accepted for publication in international peer reviewed journals.

Paper I J. P. Reistad, N. Østgaard, K. M. Laundal, and K. Oksavik, On the non-conjugacy of nightside aurora and their generator mechanisms, *Journal of Geophysical Research*, Vol. 118, doi:10.1002/jgra.50300, 2013

Paper II J. P. Reistad, N. Østgaard, K. M. Laundal, S. Haaland, P. Tenfjord, K. Snekvik, K. Oksavik, and S. E. Milan, Intensity asymmetries in the dusk sector of the poleward auroral oval due to IMF B_x, *Journal of Geophysical Research*, Vol. 119, doi:10.1002/2014JA020216, 2014

Paper III P. Tenfjord, N. Østgaard, K. Snekvik, K. M. Laundal, J. P. Reistad, S. Haaland, and S. E. Milan, How the IMF By induces a By component in the closed magnetosphere and how it leads to asymmetric currents and convection patterns in the two hemispheres, *Journal of Geophysical Research*, Vol. 120, doi:10.1002/2015JA021579, 2015

Paper IV J. P. Reistad, N. Østgaard, P. Tenfjord, K. M. Laundal, K. Snekvik, S. Haaland, S. E. Milan, K. Oksavik, H. U. Frey, and A. Grocott, Dynamic effects of restoring footpoint symmetry on closed magnetic field-lines, *Journal of Geophysical Research*, Vol 121, doi:10.1002/2015JA022058, 2016

During my PhD studies, I have also contributed to the following papers. They are not a part of this thesis.

A S. Haaland, J. P. Reistad, P. Tenfjord, J. Gjerloev, L. Maes, J. DeKeyser, R. Maggio, C. Anekallu, N. Dorville, Characteristics of the flank magnetopause: Cluster observations, *Journal of Geophysical Research*, Vol. 119, doi:10.1002/2014JA020539, 2014

B N. Østgaard, J. P. Reistad, P. Tenfjord, K. M. Laundal, K. Snekvik, S. E. Milan, S. Haaland, What are the mechanisms that produce auroral asymmetries in the conjugate hemispheres?, AGU Monograph Series, Auroral Dynamics and Space Weather, Editors: Yongliang Zhang and Larry Paxton, 2015

C K. M. Laundal, S. E. Haaland, N. Lehtinen, J. W. Gjerloev, N. Østgaard, P. Tenfjord, J. P. Reistad, K. Snekvik, S. E. Milan, S. Ohtani, B. J. Anderson, Birkeland current effects on high-latitude ground magnetic field perturbations, *Geophysical Research Letters*, doi:10.1029/2015GL064831, 2015

D N. Y. Ganushkina, M. W. Liemohn, S. Dubyagin, I. A. Daglis, I. Dandouras, D. L. De Zeeuw, Y. Ebihara, R. Ilie, R. Katus, M. Kubyshkina, S. E. Milan, S. Ohtani, N. Østgaard, J. P. Reistad, P. Tenfjord, F. Toffoletto, S. Zaharia, O. Amariutei, Defining and resolving current systems in geospace, *Annales Geophysicae*, 33, 1369-1402, doi:10.5194/angeo-33-1369-2015, 2015

E K. M. Laundal, J. W. Gjerloev, N. Østgaard, J. P. Reistad, S. Haaland, K. Snekvik, P. Tenfjord, S. E. Milan, The impact of sunlight on high-latitude equivalend currents, *Journal of Geophysical Research*, Vol. 121, doi:10.1002/2015ja022236, 2016

Contents

Preface iii

Abstract vii

Acknowledgements ix

1 Introduction 1

2 Relevant background 5
- 2.1 Plasma flow in the near-Earth space . . . 5
  - 2.1.1 Large-scale circulation: The Dungey cycle . . . 5
  - 2.1.2 A dynamic description: The expanding/contracting polar cap paradigm . . . 8
- 2.2 Symmetries in the near-Earth space . . . 10
- 2.3 Asymmetries in the near Earth space . . . 11
  - 2.3.1 Hemispheric differences in solar illumination . . . 11
  - 2.3.2 Hemispheric differences in Earth's magnetic field . . . 12

3 Mechanisms for producing asymmetric Birkeland currents and aurora 15
- 3.1 Asymmetric solar wind dynamo . . . 15
- 3.2 Asymmetric response to IMF B_y . . . 19
  - 3.2.1 Motivation from earlier studies . . . 19
  - 3.2.2 An updated understanding of the induced B_y effect . . . 21

4 Global auroral imaging 29
- 4.1 Instrument design . . . 29
  - 4.1.1 IMAGE FUV . . . 29
  - 4.1.2 Polar VIS Earth . . . 33
- 4.2 Interpretation . . . 34
  - 4.2.1 Relating the camera signal to particle precipitation . . . 34
  - 4.2.2 Comparing auroral intensities in the two hemispheres . . . 38

4.2.3 Identification of conjugate regions 40
4.2.4 Auroral intensity as a proxy for upward Birkeland current . . . 41

5 Results and discussion **43**
5.1 Summary of papers 43
5.1.1 Paper I 43
5.1.2 Paper II 43
5.1.3 Paper III 44
5.1.4 Paper IV 45
5.2 Discussion of papers 46
5.2.1 The validity of using global auroral images as a proxy for upward Birkeland current 46
5.2.2 The effect of dipole tilt 50

6 Conclusions **55**

7 Future prospects **57**
7.1 Asymmetric SW dynamo 57
7.2 Restoring symmetry process 57

Abbreviations **59**

References **61**

Paper I: On the non-conjugacy of nightside aurora and their generator mechanisms **73**

Paper II: Intensity asymmetries in the dusk sector of the poleward auroral oval due to IMF B_x **89**

Paper III: How the IMF By induces a By component in the closed magnetosphere and how it leads to asymmetric currents and convection patterns in the two hemispheres **103**

Paper IV: Dynamic effects of restoring footpoint symmetry on closed magnetic field-lines **123**

Abstract

The work presented in this thesis is part of ongoing research within one of the research groups at the Birkeland Centre for Space Science (BCSS) at the Department of Physics and Technology, University of Bergen. Members of this group have earlier found that the two hemispheres can exhibit large asymmetries in the auroral display, contrary to what have usually been assumed. The group at BCSS is focusing on aspects of the solar wind - magnetosphere - ionosphere interactions that can lead to a different outcome in the two polar hemispheres in terms of e.g. convection speeds, magnetic field perturbations, electric currents, and auroral emissions.

As a part of this ongoing effort, this thesis investigates two mechanisms proposed to be important in creating north-south asymmetries in the auroral display. To do this, simultaneous images from space of both the aurora borealis and the aurora australis are used to identify periods and regions when asymmetric aurora occurs. During the work on this thesis, a systematic search was performed resulting in the hitherto largest dataset of such simultaneous global imaging of the Earth's dual auroras.

In Paper I [*Reistad et al.*, 2013] we find that non-conjugate aurora, being features only visible, or significantly brighter in one hemisphere, is rather common during active auroral displays. Furthermore, we found that 10 out of 15 identified non-conjugate features were consistent with at least one of the two mechanisms investigated in detail in this thesis.

Two mechanisms has been investigated in detail to learn more about their importance. In Paper II [*Reistad et al.*, 2014] we find that the poleward part of the dusk side auroral oval in the northern hemisphere is on average brighter when the Interplanetary Magnetic Field (IMF) is pointing away from the Sun, compared to when IMF is pointing toward the Sun, during southward directed IMF. The opposite result is found when looking at the dusk side auroral oval in the southern hemisphere. We interpret the results as a possible effect of the asymmetric Solar Wind (SW) dynamo, suggested to be responsible for asymmetric energy transfer from the SW into the conjugate hemispheres. This mechanism has been suggested to explain event studies of asymmetric aurora, but this is the first time it is investigated statistically. Therefore, these results suggest that this mechanism can be of general importance and its accumulative effect

of asymmetric energy transfer from the SW into the conjugate hemispheres might be important.

The second mechanism investigated is related to the dynamic effects from IMF B_y on how field-lines convect from the nightside toward the dayside. It has earlier been suggested that IMF B_y could affect the two hemispheres differently but a detailed description has been lacking. Our group at BCSS has developed an updated understanding that can explain, with a higher level of detail than earlier, how the SW forcing during IMF B_y can lead to hemispheric asymmetries in convection speeds, Birkeland currents, and aurora along a closed field-line. This is presented in Paper III [*Tenfjord et al.*, 2015]. In Paper IV [*Reistad et al.*, 2016] we show observations that support this understanding, where an event with highly displaced aurora between the hemispheres are presented, together with observations of asymmetric ionospheric convection and Birkeland currents, consistent with our understanding of the IMF B_y influence.

The main conclusions in this thesis are:

→ Non-conjugate features are common in active auroral displays

→ IMF B_x influences the duskside auroral intensity during southward IMF oppositely in the two hemispheres

→ The opposite auroral response to IMF B_x in the conjugate hemipsheres is consistent with a more efficient SW dynamo on average in one hemisphere compared to the other

→ Field-lines with asymmetric footpoints (induced by IMF B_y) will release magnetic stress into one hemisphere as they convect toward and around the Earth from the nightside. We name this the *process of restoring symmetry*

→ Signatures consistent with the process of restoring symmetry are observed in both ionospheric convection data and in average maps of BCs, suggesting that this mechanism can be responsible for substantial asymmetric forcing of the two hemispheres

Acknowledgements

This thesis is the result of six years of work at the University of Bergen in the Department of Physics and Technology, first as a master student and then as a PhD candidate. Here is just mentioned some of the people that I have had the pleasure to know throughout this time. You have all contributed in a unique way making this period unforgettable.

First of all I would like to thank my supervisor Nikolai Østgaard for all his guidance, discussions, and positive attitude. You have been a true inspiration, both scientifically through all your ideas, and personally with your everyday enthusiasm. I would also thank my supervisor Kjellmar Oksavik for all your constructive and prompt feedback and advices. Thank you to all the fellow students and staff at the Birkeland Centre for Space Science in Bergen. I have truly enjoyed your everyday company the last years. A special thank to the Q1 team: Nikolai, Kalle, Paul, Kristian, Theresa, Stein, and Steve for the fruitful collaboration. It has been a pleasure to work with you. I would also thank Harald and Sabine Frey for their great hospitality and collaboration during my stay at UC Berkeley.

This thesis would not have happened without the use of imaging data provided by the IMAGE-FUV team at Berkeley, and the Polar VIS group in Iowa. A special thank to Karl M. Laundal and Harald Frey for patiently educating me on the many complicated aspects of auroral imaging from space.

A great thank also to my parents for always encouraging my curiosity. Last but not least, I will thank my wonderful wife Silje for her everlasting support.

Bergen, April 2016
Jone Peter Reistad

Chapter 1

Introduction

The Earth's magnetic field shields our living environment from the continuous flow of plasma in the Solar Wind (SW). However, the outermost regions of the magnetosphere are in direct contact with the shocked SW and its embedded interplanetary magnetic field (IMF). The interactions at this interface are responsible for mass, momentum, and energy transfer into the magnetosphere and hence represent a coupling to space that affect our living environment.

How the Earth is coupled to space has been subject for research for more than a century. The charged particles populating the magnetosphere flow freely along the magnetic field. Hence, the polar regions are of special interest for the interaction between the SW and the magnetosphere, as only the magnetic field-lines at high-latitudes couple to this region in space. The near-Earth manifestations of the SW-magnetosphere interactions have been studied in a number of ways. One example is the aurora, which is produced in the upper atmosphere, typically from 100-300 km. The light is emitted by atoms and molecules in the atmosphere after being excited due to collisions with charged particles. More precisely, it is secondary electrons produced when charged particles precipitate along Earth's magnetic field and collide with the atmosphere, that excites the atmospheric atoms and molecules which eventually emit the aurora. The aurora therefore serves to light up the footpoint of disturbed magnetic field-lines. Hence, the aurora can be used as a diagnostic tool for remote sensing the more distant processes in the magnetosphere.

The two polar hemispheres can to some extent represent two separate experiments when investigating how Earth interacts with the SW. Hence, studies looking at the simultaneous response in the two hemispheres can be used to test our understanding of the SW-magnetosphere-ionosphere interactions. This approach is of special interest as the global understanding of how Earth is coupled to space is largely based on observations from only one hemisphere. This thesis makes use of global simultaneous imaging of the aurora from both hemispheres to achieve further insight into the mechanisms that

produce the disturbances manifested by the aurora. As the Earth's magnetic field interacting with the SW is largely symmetric between the hemispheres, it is expected that the large-scale processes leading to the aurora should be rather similar in the two hemispheres. However, observations have shown that this is not always the case, suggesting that the global aurora can be substantially modified by mechanisms affecting the conjugate hemispheres differently. Little is known about such mechanisms, much due to the sparse amounts of simultaneous data available from conjugate regions. This thesis specifically investigates mechanisms proposed to influence how the two polar hemispheres are asymmetrically coupled to space. In particular we have investigated the following mechanisms:

1. The asymmetric SW dynamo
2. Asymmetric forcing of the magnetosphere due to IMF B_y
3. Effects from interhemispheric currents associated with ionospheric conductivity gradients

This work gives constraints and aims at expanding our knowledge about the two first mechanisms.

In Paper I we identify features of the global aurora that is seen only in one hemisphere, or is significantly brighter in one hemisphere. We show that these observations can to a large extent be explained by one or more of the three earlier proposed mechanisms listed above, and suggest that the SW dynamo and IMF B_y mechanism could be of greatest importance among the three.

Paper II specifically investigates the importance of the SW dynamo mechanism by studying the average auroral response during favourable and not favourable conditions. We find that the aurora is significantly brighter during conditions favourable for this mechanism to operate compared to non-favourable conditions.

An updated and more detailed understanding of how IMF B_y leads to asymmetric forcing of the two hemispheres has emerged during collaborative work at the Birkeland Centre for Space Science (BCSS) that this PhD project has been a part of. This updated description is the topic of Paper III.

We have also done a systematic search for all available conjunctions of conjugate imaging from space by the IMAGE and Polar spacecraft. This resulted in more than 10 times the amounts of data previously analysed. From this extended dataset we managed to find an event suitable for investigating the IMF B_y mechanism in great detail to explore the validity of our updated understanding. In Paper IV we show observations of aurora, ionospheric convection, and associated Birkeland currents that support our understanding of how the two hemispheres are oppositely forced due to IMF B_y. These

observations demonstrate the asymmetric influence of this mechanism at a level of detail never shown before.

In the next chapter we give a brief description of the large-scale physical processes relevant for understanding the Earth-space connection. In Chapter 3 we give a detailed description of mechanisms one and two listed above. Chapter 4 introduces the main instrumentation used (global imaging of the Earth's aurora). The main findings from the four papers are summarized and discussed in Chapter 5. In Chapter 6 we list our main conclusions with emphasis on what we have learned with regard to the two mechanisms under consideration. Chapter 7 points at unsolved questions that should be addressed in the future to further enhance our understanding of the two mechanisms.

Chapter 2

Relevant background

This thesis investigates two specific mechanisms that can affect the global transport of energy throughout the near-Earth space differently in the conjugate hemispheres. Before going into details regarding how the two hemispheres can be affected differently, we set the stage by presenting a first order symmetric view of how plasma is circulated in the near-Earth space. This is a concept referred to as the 'Dungey-cycle' named after the first scientist to suggest that this circulation is driven by the process of magnetic reconnection [*Dungey*, 1961].

2.1 Plasma flow in the near-Earth space

By near-Earth space we mean the region around the Earth dominated by the Earth's magnetic field and its interaction with the SW. As illustrated in Figure 2.1, this is typically within 20 Earth radii (R_E) in the sunward direction, but can extend a few hundred R_E in the anti-sunward direction. Throughout the thesis we will use the Geocentric Solar Magnetic (GSM) coordinate system to define geometry and directions in the near-Earth space. The GSM x-axis refers to the direction toward the Sun from the Earth. The z-axis, pointing northward, lies in the plane normal to the x-direction along the projection of Earth's magnetic dipole axis in this plane. The y-axis completes the system pointing in a duskward direction. Hence, when writing 'northwards' or 'southwards' IMF, we refer to the GSM z-component being > 0 or < 0, respectively.

2.1.1 Large-scale circulation: The Dungey cycle

The large-scale circulation of plasma driven by reconnection was first described by *Dungey* [1961] and is schematically illustrated in Figure 2.1. Reconnection is a process that allows efficient plasma transport throughout the near-Earth space by merging different magnetic domains. In the near-Earth space, reconnection takes place when the

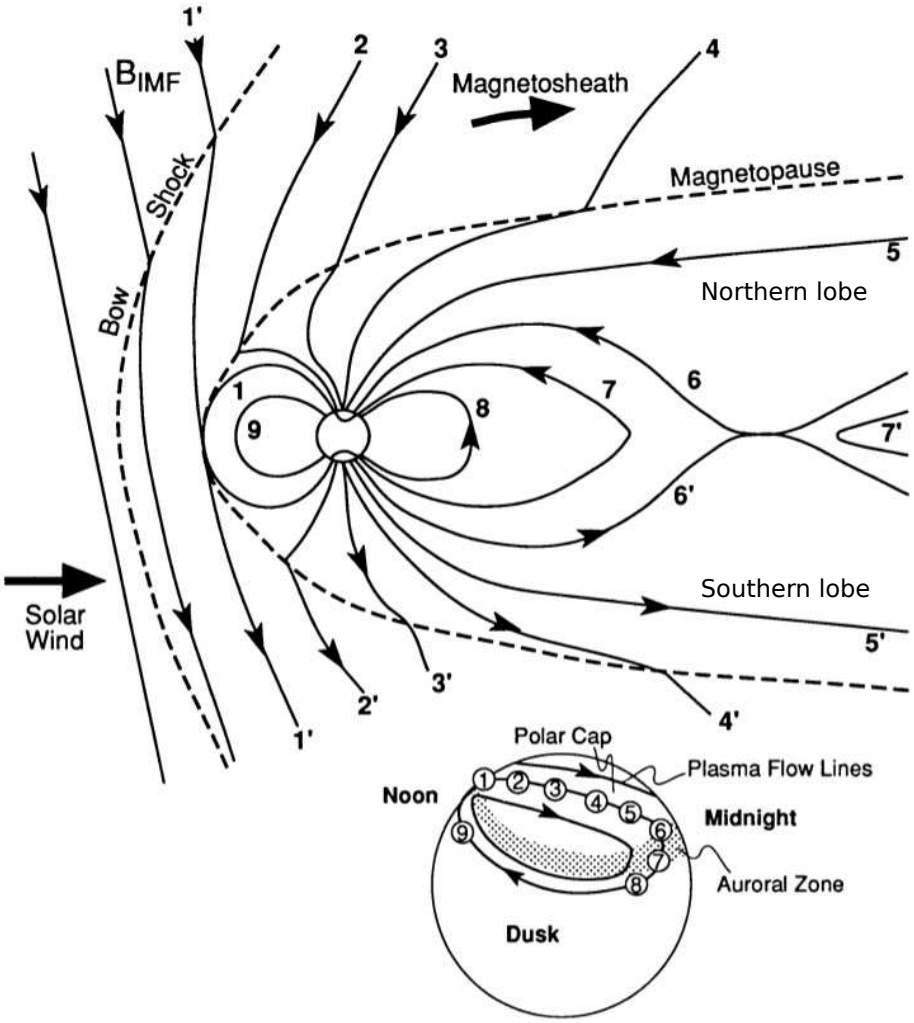

Figure 2.1: Schematic illustration of the plasma circulation in the open magnetosphere. 1: The SW with a southward directed IMF approaches the Earth on the dayside where reconnection occurs, opening magnetic flux. 2-5: Newly opened field-lines are draped downtail and added to the lobes at equal rates in both hemispheres. 6: Magnetic reconnection between lobe field-lines closes magnetic flux in the tail. 7-9: Newly closed field-lines convect toward the dayside to complete the circulation. The ionospheric footpoint of this circulation with corresponding numbers are seen in the inset at the bottom. After *Hughes* [1995].

IMF and the Earth's magnetic field have components anti-parallel to each other and are brought together [*Crooker*, 1979; *Gonzalez and Mozer*, 1974]. Since the SW impinges head-on to the subsolar magnetopause, a southward directed IMF will be anti-parallel to the northward directed terrestrial field and hence provide the most favourable conditions for subsolar reconnection, as indicated by step 1 in Figure 2.1. After reconnecting with the Earth's magnetic field, the field-line that previously had both footpoints on Earth (referred to as a closed field-line) is now split into two separate field-lines both having one footpoint on Earth and the other end extending back to the Sun (referred to as open field-lines). By definition, the same number of open field-lines are created in each hemisphere. That is needed for the Maxwell equation $\nabla \cdot \mathbf{B} = 0$ to be fulfilled. Hence, the rate at which magnetic flux is opened is equal in both hemispheres. As illustrated in steps 2-5 in Figure 2.1, the field-lines opened on the dayside are transported tailward due to the anti-solar SW velocity and are added to the magnetospheric lobes in both hemispheres. The magnetospheric convection described here is also seen in the upper atmosphere. The ionospheric large-scale convection pattern resembles a manifestation of the magnetospheric convection discussed above. In the inset in the bottom of Figure 2.1 one can see the corresponding ionospheric convection cycle with numbers referring to the stages illustrated in the magnetosphere.

As flux is added at the same rate in the two lobes, open field-lines are forced toward the centre of the magnetotail. The open lobe field-lines point in opposite direction in the two hemispheres, and when they are brought sufficiently close, they can again reconnect in the tail. The result of reconnection of two such open field-lines is one new closed field-line connected to the Earth, and one plasmoid embedded in the SW, not magnetically connected to Earth. As this process creates closed field-lines (again at the same rate in both hemispheres) it increases the amount of closed magnetic flux and is therefore often just referred to as closure of flux. This is illustrated in stage 6 in Figure 2.1. The highly stretched field-line in stage 6 is subject to a tension force that leads to convection toward the Earth (6-8). As this process continues (stages 1-8), closed flux is eroded on the dayside (stage 1). The newly closed flux on the nightside will therefore convect toward the dayside (stage 9) in response to pressure imbalances associated with the changes in magnetospheric shape as the erosion of flux on the dayside continues [*Milan*, 2015], completing the cycle of plasma transport in the magnetosphere. Hence, reconnection (change of field topology) is what allows the large-scale convection in which can be explained through both the magnetic tension and pressure forces.

2.1.2 A dynamic description: The expanding/contracting polar cap paradigm

The description of the open magnetosphere suggested by *Dungey* [1961] provided a theoretical framework to understand the large-scale structure and dynamics of the SW-magnetosphere-ionosphere system. In the years that followed this new conceptual understanding, satellites started to explore the near-Earth space, and observations supporting reconnection, (e.g. *Aubry et al.* [1970] and *Sonnerup and Ledley* [1979]) showed that the magnetosphere is indeed open. In the following decades, it was realized that the process of nightside reconnection not necessarily followed directly after dayside reconnection, but should be treated as a fundamentally different process, exciting flows deep within the magnetospheric tail [*Freeman and Southwood*, 1988; *Siscoe and Huang*, 1985]. This two stage description of the large-scale plasma transport in the magnetosphere-ionosphere system is commonly known as the 'expanding/contracting polar cap' paradigm (ECPC) and was first completely formulated by *Cowley and Lockwood* [1992]. Their central point was that the flow within the system was not associated with the amount of existing open magnetic flux, but with changes in the open flux caused by reconnection events at the dayside magnetopause or in the tail [*Cowley*, 2015]. Further, *Cowley and Lockwood* [1992] realized that it was the erosion of open flux (tail reconnection) or closed flux (dayside reconnection) that lead to deformations in the magnetosphere, in which the magnetosphere responds to return to a more symmetric state, as can be described by the tension and pressure forces. The flows excited in the magnetosphere would also be visible in the ionosphere, effectively bringing the boundary between open and closed field-lines back to a more symmetric configuration also there.

The excitation and decay of magnetospheric and ionospheric flows in response to the opening of magnetic flux by dayside reconnection is illustrated in Figure 2.2 (after Figures 5 and 6 in *Cowley and Lockwood* [1992]). The upper row in Figure 2.2 illustrates the closed magnetosphere when looking down on the equatorial plane. It contains all closed flux (gray shade), which is the total magnetic flux associated with Earth's dipole, F_{tot}, minus the open flux F. The second row illustrates a cross-section of the magnetotail when looking toward the Earth from the tail. The closed flux is indicated by the grey shaded region and corresponds to the plasma sheet. Above and below this region is the open flux F. In the bottom row is the corresponding situation in the polar ionosphere when looking down at the pole where the solid black line indicates the boundary between open and closed flux. In the second column is shown the magnetic topology with respect to open and closed field-lines just after a small amount of flux, dF, has been opened by dayside reconnection. Associated flows in the closed magneto-

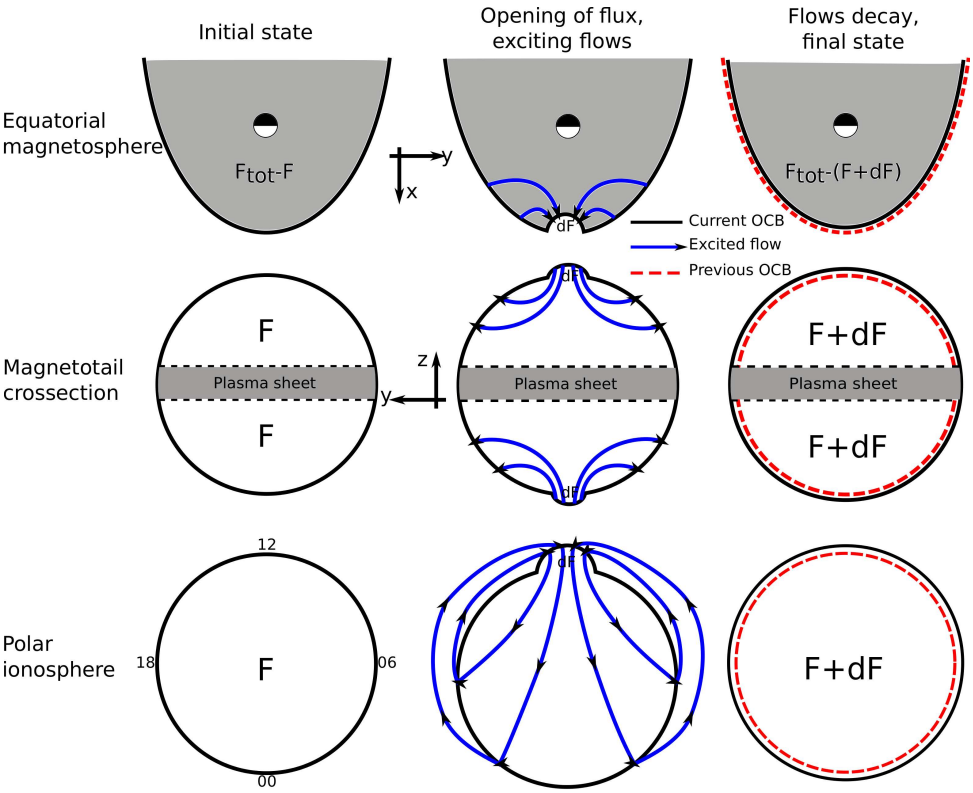

Figure 2.2: A dynamic description of the Dungey cycle, stages 1-5 in Figure 2.1, known as the ECPC paradigm. The three columns represent three different stages. Left: initial state of the magnetosphere before opening of flux. Middle: the dynamic response of the magnetosphere due to opening of flux, quantified as dF. Blue arrows represent the excited flows. Right: the reconfigured magnetosphere after flux has been added. The previous shape of the magnetosphere is indicated with red dashes for reference. The three rows represent different perspectives. Top: looking down at the equatorial plane, grey indicate the closed field-line region. Middle: cross-section of the magnetotail looking from the tail toward Earth. F indicate the amount of initial open flux. Bottom: Looking down at the polar ionosphere. After Figures 5 and 6 of *Cowley and Lockwood* [1992].

sphere (upper), magnetospheric lobes (middle), and in the ionosphere (lower) is shown as blue flow-lines. These flows are excited by reconnection and decays as the boundaries between open and closed flux relax to a more symmetric configuration. Note that flow across the open-closed boundary here only occurs where and when closed flux is eroded on the dayside, i.e. between the first and the second column. In the last column, the new symmetric boundary between open and closed flux is shown from the three perspectives as solid black lines. For comparison, the previous symmetric boundary before flux opening is shown as red dashed lines (same as solid black lines in the left column). For flux closure due to tail reconnection, a similar sketch could be made (not shown here) emphasizing its influence on the boundary between open and closed flux and the subsequent excited flows that bring the boundaries toward a symmetric situation.

The expected large-scale behaviour predicted from the ECPC paradigm has been investigated in great detail using observations and found to generally show very good agreement with this understanding [*Chisham et al.*, 2008; *Clausen et al.*, 2012; *Milan et al.*, 2007, 2009]. Hence, knowledge of the open-closed boundary (OCB) location and the plasma flow relative to it are key parameters needed to describe the dynamics of the large-scale solar wind-magnetosphere-ionosphere coupling.

2.2 Symmetries in the near-Earth space

Since magnetic monopoles are not known to exist in nature, $\nabla \cdot \mathbf{B} = 0$ must hold everywhere. Hence, the amount of open flux is the same in both hemispheres. Therefore, the number of field-lines opened and closed by dayside and nightside reconnection, respectively, is identical in the two hemispheres, resulting in the same net magnetic flux circulation in both hemispheres. However, plasma circulation cells that do not contribute to any net plasma circulation may exist and can be different in the two hemispheres. This could be convection cells entirely on open field lines (e.g. lobe convection cells [*Burch et al.*, 1985; *Crooker and Rich*, 1993; *Reiff and Burch*, 1985]), or convection cells entirely on closed field-lines (e.g. due to viscous interactions [*Axford and Hines*, 1961; *Reiff and Burch*, 1985].

At the surface of the Earth, the magnetic field is relatively structured due to contributions from crustal fields, but dominated by a dipole configuration. However, the structured part of the field decreases faster with radial distance than the dipole contributions (e.g. equation 5.79 in *Griffiths and College* [2008]), leaving the IMF to interact with a highly symmetric dipole-like field at the magnetopause at ~ 10 Earth radii (R_E) upstream. Therefore, there are no significant local-time variations of the magnetic field

strength at magnetopause distances due to magnetic anomalies on the ground that could affect the SW - magnetosphere coupling.

The aurora is caused by atmospheric loss, also called precipitation, of charged particles mirroring between hemispheres while trapped inside the magnetosphere. Due to the north-south symmetric topology of the magnetosphere, the scattering of charged particles into the loss cone (e.g. due to waves or stretching of the tail) are assumed to be highly symmetric between the hemispheres due to the symmetric structure of the magnetosphere. This has traditionally been the first order approximation when considering the large-scale conjugacy aspects of the aurora.

2.3 Asymmetries in the near Earth space

There are also important factors that set the stage for hemispheric differences in the electrodynamic solar wind - magnetosphere - ionosphere coupling. The next chapter describes the two specific mechanisms for asymmetric influence investigated in this thesis. Before going into details regarding those two mechanisms, we will give a brief introduction to two of the most evident properties that is different in the conjugate hemispehres. That is solar illumination and magnetic field strength. Although not being the main focus of this thesis, these considerations are important to keep in mind to understand the coupled system.

2.3.1 Hemispheric differences in solar illumination

One important asymmetry in the system is related to the orientation of the magnetic axis of the Earth (often referred to as the dipole axis) relative to the Sun direction (approximately representing the direction of the SW). A measure of this asymmetry is quantified by the dipole tilt angle, defined as 90° minus the angle between the vector pointing at the Sun and the dipole axis vector, see Figure 2.3. Hence, for the perpendicular (symmetric) case, the dipole tilt equals 0 and the high magnetic latitudes in the two hemispheres are similar exposed to solar illumination. This is the case in the symmetric situation shown in Figure 2.1. From this definition (Figure 2.3), positive dipole tilt angle corresponds to summer in the northern hemisphere. Due to the misalignment of the magnetic and rotational axis of the Earth, the dipole tilt angle exhibits a $\pm 11^\circ$ diurnal variation in addition to the seasonal variation of $\pm 23^\circ$ due to the fixed orientation of the rotation axis as the Earth orbits the Sun. Hence, for quantifying hemispheric differences in solar exposure in magnetically conjugate regions, the dipole tilt angle is a much more accurate description than day of year. The larger absolute value of the

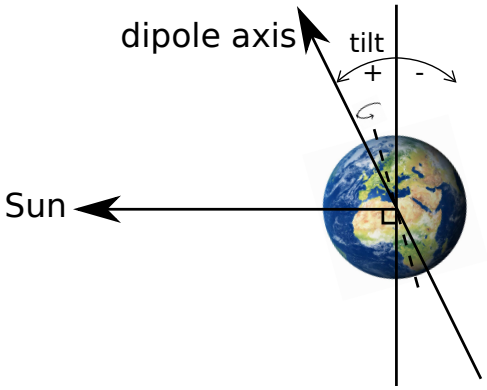

Figure 2.3: Definition of the dipole tilt angle: 90° minus the angle between the vector pointing at the Sun and the dipole axis vector. The dipole tilt angle is therefore 0 when the dipole is illuminated equally in the two hemispheres, positive during summer in the norhtern hemisphere, and negative during the northern winter.

dipole tilt angle the larger will the differences in solar exposure at magnetically conjugate regions be.

The dynamics of the near-Earth space is often expressed in terms of electric currents. Hence, the ionospheric conductivity is of great importance when describing the system. On the dayside, solar Extreme Ultraviolet (EUV) radiation is the most important source of ionization in the ionosphere. On the nightside the situation is quite different as particle precipitation is the only source of ionization. Although particle precipitation and associated BC in each end of a closed field-line are connected through the same magnetospheric region, the different ionospheric conductivity in the two ends can lead to significant differences in precipitation characteristics and BC strength in the two hemispheres. In particular, the dark end of a field-line is found to have more energetic particle precipitation and stronger BCs than the conjugate sunlit end for field-lines on the nightside [*Green et al.*, 2009; *Newell et al.*, 2010; *Ohtani et al.*, 2009]. This has been suggested to be related to an ionospheric feedback mechanism [*Lysak*, 1991; *Newell et al.*, 2010; *Ohtani et al.*, 2009], but this is still debated.

2.3.2 Hemispheric differences in Earth's magnetic field

As mentioned earlier, asymmetries in the Earth's main field are insignificant at distances larger than a few R_E. However, within the ionosphere the differences can be substantial. In general, the magnetic field is more uniform in the northern hemisphere. In the southern hemisphere the field strength decreases rapidly toward the South Atlantic Anomaly. At these longitudes, the magnetic field is about twice as strong in the

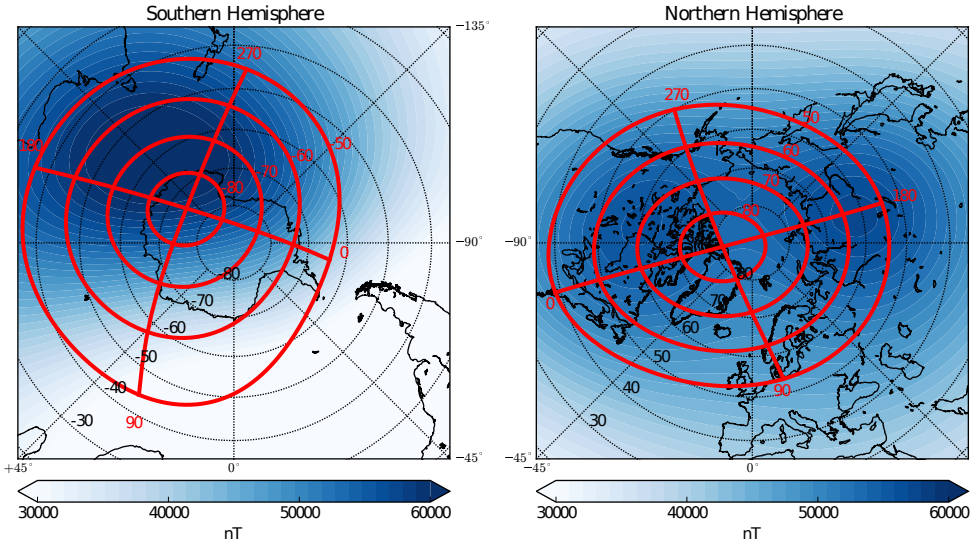

Figure 2.4: Polar map of southern hemisphere (left) and northern hemisphere (right) where black parallels and meridians correspond to geographic coordinates. International Geomagnetic Reference Field (IGRF) strength at 130 km computed for the year 2001 is shown on the map in color. On top is shown the apex magnetic coordinate system in red.

northern hemisphere compared to the conjugate location (at 50° MLAT (Magnetic latitude)), see Figure 2.4. The differences magnetic field strength can lead to a number of effects that will be slightly different in the two hemispheres as e.g. mirroring altitude, size of the loss cone, and ionospheric conductivity [equation 1 in *Cnossen et al.* [2011]].

Although hemispheric differences in e.g. solar illumination seen on a magnetic grid is to a large degree described by the dipole orientation, non-dipole contributions from the Earth's magnetic field leads to further differences. When representing electrodynamic quantities observed close to Earth (e.g. aurora or F-layer plasma drift or current densities oriented with respect to Earth's magnetic field), a more realistic model than a centered dipole is needed. Most commonly used is the Altitude Adjusted Corrected Geomagnetic coordinates (AACGM) [*Baker and Wing*, 1989] or the apex coordinate system [*Richmond*, 1995; *VanZandt et al.*, 1972]. Figure 2.4 shows the apex coordinate system plotted in red on top of a geographic grid. One can see that the more uniform field strength in the northern hemisphere results in a more uniform magnetic grid. In this coordinate system (taking the realistic magnetic field into account), the geomagnetic pole in the southern hemisphere has a larger offset from the geographic pole compared to the northern hemisphere. This is clearly seen in Figure 2.4 by comparing the geographic and magnetic grids. The difference in offset of the geomagnetic

poles are $\sim$ 800 km, demonstrating that a centred dipole description is inadequate as it would have given the same offset in North and South. The larger geomagnetic pole offset leads the southern hemisphere end of a field-line to experience larger variations in solar exposure during the course of a day than the northern hemispheric end.

The effect of different magnetic field-strength can also affect the convection speeds at conjugate locations. Since the large-scale plasma circulation is determined by opening and closure of magnetic flux, the net plasma circulation must be the same in the two hemispheres. The travel time of a closed field-line returning toward the dayside from the tail must be the same in the two hemispheres to have equal flux transport rate. However, measured in the geographic frame (m/s), the speed will be different in the two ends whenever the field-strength is different between the two foot-points to fulfil the requirement of equal flux transport on average.

Chapter 3

Mechanisms for producing asymmetric Birkeland currents and aurora

The topic of this thesis is how the two hemispheres can be affected differently by the solar wind-magnetosphere-ionosphere coupling. *Østgaard and Laundal* [2012] suggested that the observed hemispheric asymmetries in Earth's aurora could be explained by interhemispheric or asymmetric Birkeland currents. Based on earlier findings, they suggested three mechanisms that could play an important role in this regard. This thesis investigates two of these mechanisms in more detail in order to learn more about their importance. This chapter gives a detailed description of these mechanisms believed to affect the global aurora differently in the two hemispheres.

3.1 Asymmetric solar wind dynamo

Although opening and closure of magnetic flux by reconnection is by far the main driver of large-scale plasma circulation within the magnetosphere, the energy transfer from the solar wind into the magnetosphere is a much more complex process [*Koskinen and Tanskanen*, 2002; *Tenfjord and Østgaard*, 2013]. One aspect of the energy transfer process is what is known as the solar wind dynamo [e.g. *Cowley*, 1981b; *Koskinen and Tanskanen*, 2002; *Siscoe et al.*, 2000]. After subsolar reconnection during southward IMF, newly reconnected flux tubes are draped down the magnetotail. During this process, tangential stresses act on the on these flux tubes and serves to slow them down as they are added to the lobes. This process represents conversion of kinetic energy from the solar wind into driving the magnetopause current at high latitudes. This is known as the solar wind dynamo as this perpendicular current is directed opposite to the electric field due to the plasma motion.

When the IMF has a significant x-component in addition to being southward, the

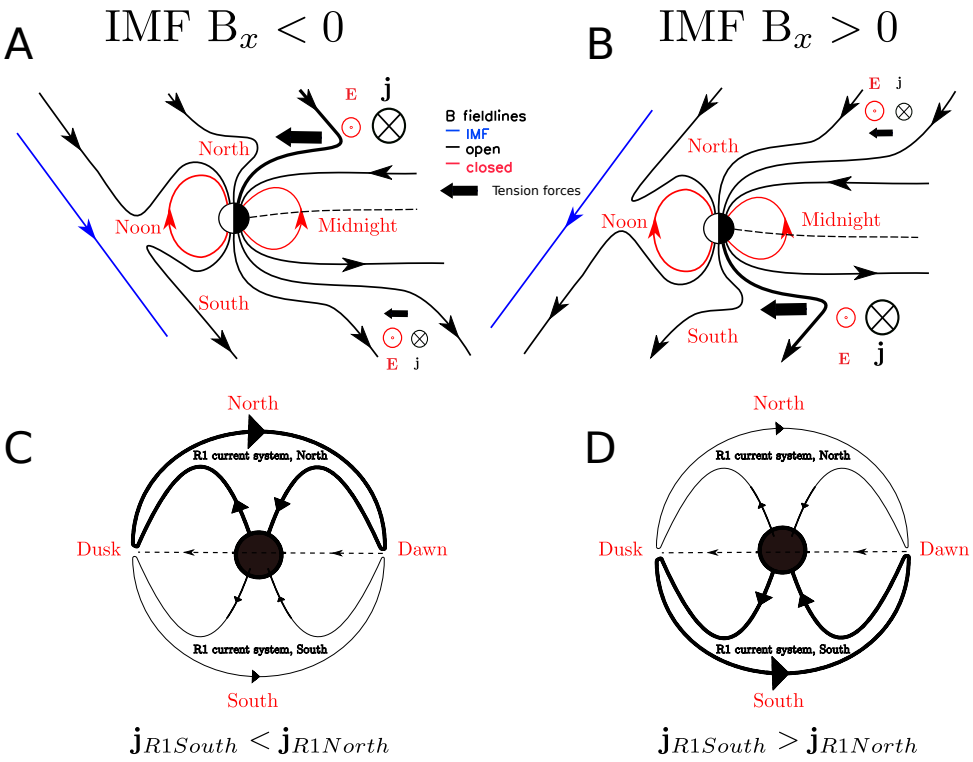

Figure 3.1: A: The presence of a negative x-component in the IMF during southward IMF B_z resulting in different magnetic tension forces (illustrated with large black arrows) on open field lines possibly affecting the energy transfer at the magnetopause differently in the two hemispheres. Lines in blue, black, and red show the interplanetary, open, and closed field-lines, respectively. At high latitudes, tailward of the terminator, the tension force will decelerate plasma and affect the magnetopause current density. This is indicated with the black arrow going into the figure in this region. This figure is adopted from *Cowley* [1981b]. B: Corresponding figure during IMF B_x positive. C: Associated changes in current density for negative IMF B_x of the Region 1 current system that are generated across the high-latitude magnetopause [*Guo et al.*, 2008; *Siscoe et al.*, 1991, 2000]. Here the Earth is viewed from the tail. D: Corresponding figure during positive IMF B_x.

tangential stress, or magnetic tension force on the flux tubes being draped downtail, is believed to differ in the two hemispheres. As this scenario can affect the energy transfer at the magnetopause differently in the two hemispheres, it represents a hemispheric asymmetry in the solar wind dynamo, referred to as the asymmetric SW dynamo. This asymmetric scenario was first pointed out by *Cowley* [1981b] and later supported by others [*Laundal and Østgaard*, 2009; *Østgaard and Laundal*, 2012]. Figure 3.1 shows simplified sketches (adopted from *Cowley* [1981b]) of how the two IMF B_x directions can affect the magnetic field topology differently in two hemispheres. Figures 3.1A and 3.1B show the meridional plane in the magnetosphere during southward and negative/positive IMF B_x focusing on field-lines having an open topology (only one foopoint on the Earth). The magnetic tension force on open field-lines is illustrated with filled black arrows. Where the radius of curvature is small (large tension), these arrows are large, whereas where the radius of curvature is greater (less tension), the corresponding arrows are tiny. Neglecting particle pressure gradients, the magnetohydrodynamic (MHD) momentum equation for a quasi-neutral (one fluid) plasma is

$$\rho_m \frac{d\mathbf{v}}{dt} = \mathbf{j} \times \mathbf{B} \tag{3.1}$$

where ρ_m is mass density and $\frac{d\mathbf{v}}{dt}$ is the total derivative of the plasma bulk velocity. The $\mathbf{j} \times \mathbf{B}$ term can be rewritten into two terms:

$$\mathbf{j} \times \mathbf{B} = \frac{B^2}{\mu_0 R_C}\hat{\mathbf{n}} - \nabla_\perp \left(\frac{B^2}{2\mu_0} \right) \tag{3.2}$$

Here, R_C is the radius of curvature and $\hat{\mathbf{n}}$ is a unit normal pointing toward the centre of curvature. Hence, the $\mathbf{j} \times \mathbf{B}$ force depends on the tension force (first term in equation 3.2) and the gradient in magnetic pressure perpendicular to the magnetic field (second term in equation 3.2). Taking the cross product with $\mathbf{B}$ on both sides and using vector identities, equation 3.1 takes the form

$$\mathbf{j}_\perp = \frac{\rho_m \mathbf{B} \times \frac{d\mathbf{v}}{dt}}{B^2}. \tag{3.3}$$

Applied to the solar wind-magnetosphere system, $\mathbf{j}_\perp$ represents the magnetopause current density perpendicular to the magnetic field resulting from the combined effect of the two terms on the right side of equation 3.2. Due to the expected influence on radius of curvature from IMF B_x as indicated in Figures 3.1A and 3.1B, the magnitude of the first term on the right side in equation 3.2 can be altered therefore affecting $\mathbf{j}$. This is reflected by the different sized (between hemispheres) $\mathbf{j}$ arrows in Figures 3.1A and 3.1B.

Results from MHD modelling of magnetospheric current systems [e.g. *Guo et al.*,

2008; *Siscoe et al.*, 2000; *Tanaka*, 2000] suggest that the perpendicular currents generated at the high latitude magnetopause, is coupled to the Region 1 type Birkeland currents [*Ganushkina et al.*, 2015; *Iijima and Potemra*, 1978]. This textbook picture of the region 1 - magnetopause current system (suggested earlier by e.g. *Siscoe et al.* [1991]) is shown in Figures 3.1C and 3.1D for negative and positive IMF B_x, respectively. Here, the perspective is from inside the magnetotail looking toward the nightside Earth. The magnetopause and Region 1 currents are shown with thickness reflecting the suggested influence due to IMF B_x. One can see that for negative IMF B_x, the solar wind dynamo is more efficient in the northern hemisphere, possibly generating stronger Region 1 currents in the same hemisphere. For positive IMF B_x this is expected to have an opposite influence (stronger currents in the southern hemisphere). The strongest aurora are typically associated with precipitating electrons carrying an upward Birkeland Current (BC) [*Dubyagin et al.*, 2003; *Mende et al.*, 2003a, b; *Paschmann et al.*, 2002; *Waters et al.*, 2001]. Therefore, the dusk side aurora close to the open/closed boundary (OCB) is expected to be affected by this mechanism as this is where the Region 1 current is upward.

Not much work has been done on geomagnetic activity due to IMF B_x as it has been thought to be less geoeffective than other upstream parameters as IMF B_y, IMF B_z, solar wind velocity, and solar wind dynamic pressure. Also, due to the classic garden-hose orientation of the IMF, the B_x and B_y components are highly anti-correlated making it challenging to isolate the separate effects of the two.

Earlier studies looking specifically at IMF B_x and auroral brightness include the studies by *Baker et al.* [2003]; *Elphinstone et al.* [1990]; *Liou et al.* [1998]; *Shue et al.* [2002]. They all look at northern hemisphere aurora using global UV imaging from space. Although the auroral display is highly variable in intensity, there appears to be a consensus in all of these works to observe brighter aurora in the northern hemisphere during negative IMF B_x. This is what would be expected from the asymmetric solar wind dynamo effect during southward IMF, as was the case in the statistical studies by *Baker et al.* [2003]; *Liou et al.* [1998]; *Shue et al.* [2002]. However, they did not relate their findings to this possible explanation. More recently, *Laundal and Østgaard* [2009] showed an event during strong positive IMF B_x, where the aurora was simultaneously captured in both hemispheres by the IMAGE (Imager for Magnetopause-to-Aurora Global Exploration) [*Burch*, 2000] and Polar [*Acuña et al.*, 1995] satellites showing stronger auroral brightness this time in the southern hemisphere, consistent with the expected influence from the asymmetric solar wind dynamo mechanism. These studies motivated the further investigation of the importance of the asymmetric solar wind dynamo in generating asymmetric aurora between the two hemispheres. This is one of the main topics investigated in this thesis.

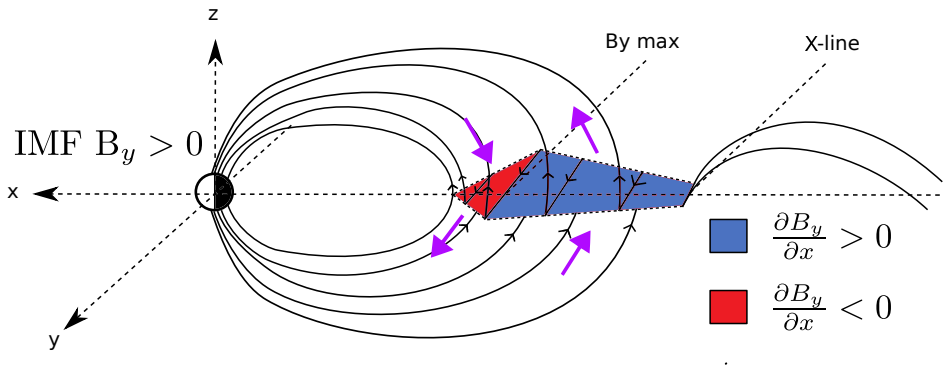

Figure 3.2: Topology of closed field-lines in the tail as presented by *Stenbaek-Nielsen and Otto* [1997]. A B_y component on closed field-lines in the tail is known to be positively correlated with IMF B_y. *Stenbaek-Nielsen and Otto* [1997] argued that the magnitude of this induced B_y should increase toward a maximum region at the inner edge of the plasma sheet, giving rise to two regions of $\frac{\partial B_y}{\partial x}$ as indicated with red and blue. According to Amperér's law, this would require a current in the z-direction, indicated with purple arrows that *Stenbaek-Nielsen and Otto* [1997] suggested could be interhemispheric currents possibly creating asymmetries in the aurora at conjugate locations, consistent with their observations.

3.2 Asymmetric response to IMF B_y

Our understanding of how IMF B_y can lead to asymmetric response in the two hemispheres has significantly advanced during the work at BCSS that this thesis is a part of. In this section we present this updated understanding that is the main results of Paper III. Although Paul Tenfjord did most of the work and was the lead author of Paper III, the new understanding of the dynamic effects of an induced B_y was a result of long and intense discussions among all the co-authors. As I played an important role in these discussions, and this work lies the foundation for Paper IV, I have included this paper [*Tenfjord et al.*, 2015] in this thesis.

This section start with introducing how earlier studies have explained how IMF B_y can lead to asymmetric aurora. Then a thorough self-consistent explanation of how B_y is induced in the closed magnetosphere is given, leading to the updated explanation model of how this leads to asymmetric forcing of the two hemispheres.

3.2.1 Motivation from earlier studies

A mechanism proposed to be responsible for hemispheric asymmetries in the magnetosphere - ionosphere coupling related to the dawn-dusk component of the IMF was suggested by *Stenbaek-Nielsen and Otto* [1997] based on conjugate auroral imaging from

an aircraft campaign between 1968 and 1971 [*Belon et al.*, 1969; *Stenbaek-Nielsen et al.*, 1972, 1973]. In the conjugate aircraft data, discrete aurora close to the poleward edge of the oval was frequently seen in one hemisphere only. In the light of further knowledge of the structure of the magnetosphere, *Stenbaek-Nielsen and Otto* [1997] proposed a mechanism that could explain their earlier conjugate flight observations. They argued that interhemispheric field-aligned currents should be present due to the non-uniform distribution of B_y within the closed magnetotail during periods of significant IMF B_y. The presence of B_y within the magnetosphere in response to IMF B_y is often referred to as 'IMF B_y penetration' in the literature, which we will later in this section argue is a misleading term. We therefore use the term 'induced B_y' instead. *Stenbaek-Nielsen and Otto* [1997] pointed out that a non-zero $\frac{\partial B_y}{\partial x}$ in the equatorial plane would require a current in the z-direction (Ampére's law). This magnetospheric configuration, in which they associated with periods during substantial IMF B_y, is shown in Figure 3.2 together with the interhemispheric currents they suggested (purple arrows). This simplified picture was based on observations of how the magnetospheric B_y was related to IMF B_y at various locations in the magnetosphere. It was based on two studies: 1) A study by *Lui* [1984] who found that B_y in the plasma sheet between 10 and 30 R_E downtail was positively correlated with IMF B_y with a magnitude of about 50% of the IMF B_y. 2) *Wing et al.* [1995] observed a similar correlation closer to Earth at geosynchronous orbit, but with a larger magnitude corresponding to about 80% of IMF B_y. They explained this increase in B_y toward the Earth due to pile-up of magnetic flux from Earthward convection. This was also supported by their analysis of a 2D MHD model. Due to the stiffness of the inner magnetosphere, the induced B_y should become zero when moving sufficiently close the Earth. Hence, they argued that the gradient of B_y in the x-direction would point in either direction from the maximum region (the red and blue region in Figure 3.2), requiring oppositely directed currents in the z-direction (the purple arrows) in which they interpreted as interhemispheric currents. We will later in this section argue that the term interhemispheric currents was misleading as the currents are driven independently into the two hemispheres from a common magnetospheric source, and not from one hemisphere into the other. These currents should therefore rather be referred to as asymmetric BCs.

Although *Stenbaek-Nielsen and Otto* [1997] did not have any IMF observations during the conjugate flights to validate their theory, this mechanism was subsequently suggested to explain new observations of asymmetric aurora [*Liou et al.*, 1998; *Østgaard et al.*, 2011a; *Shue et al.*, 2001]. However, no direct evidence of these interhemispheric currents has been shown, motivating the further investigation of this subject. This PhD project has been a part of a detailed investigation of this mechanism in the BCSS group. We have developed an updated conceptual dynamic understanding of how the induced

B_y in the magnetosphere can affect the two hemispheres differently to produce asymmetries in conjugate convection speeds, BC, and aurora. In the model presented by *Stenbaek-Nielsen and Otto* [1997] in Figure 3.2, the explanation regarding how the magnetospheric configuration could affect the ionosphere in the two hemispheres included very few details. Our updated dynamic description gives a more detailed description of how we believe B_y is first induced in the magnetosphere, and then how the closed magnetosphere evolves toward a symmetric configuration as the B_y-stress is released primarily into one hemisphere.

3.2.2 An updated understanding of the induced B_y effect

In the following, the dynamic effects of an induced B_y in the closed magnetosphere is introduced. Although this material is also covered in Paper III and in the introduction in Paper IV, this section will focus more on the conceptual understanding that laid the foundation for Paper III and Paper IV.

It was early noted that IMF B_y is important in controlling the direction of ionospheric currents in the polar cap [*Friis-Christensen and Wilhjelm*, 1975; *Friis-Christensen et al.*, 1972]. Since then, a large number of papers have documented how the magnetosphere and ionosphere respond to dawnward or duskward directed IMF. During southward IMF, the ionospheric convection is widely known to deviate from the classical twin cell pattern when there is a significant y-component [e.g. *Haaland et al.*, 2007; *Heppner and Maynard*, 1987; *Pettigrew et al.*, 2010; *Weimer*, 1995]. One cell tends to be more crescent and the other more round, often referred to as the 'banana' and the 'orange' cell, respectively, with locations approximately mirrored across the noon-midnight meridian in the two hemispheres. For positive IMF B_y, the dawn cell tends to be more banana-like in the northern hemisphere, while its corresponding dawn cell in the southern hemisphere is more orange-like.

The main motivation for the further investigation of this mechanism is based on the firmly established fact that footpoints can become asymmetric between hemispheres [*Liou and Newell*, 2010; *Østgaard et al.*, 2004, 2005, 2011b; *Wang et al.*, 2007], controlled to a large extent by IMF B_y. Knowing how asymmetric footpoints are established and evolves with time is therefore likely a key to understand its effect in the conjugate hemispheres. As already mentioned, such effects on auroral intensities has been suggested [*Liou et al.*, 1998; *Østgaard et al.*, 2011a; *Shue et al.*, 2001; *Stenbaek-Nielsen and Otto*, 1997], but without any detailed explanation, motivating the further investigation.

The asymmetric influence on the magnetosphere due to IMF B_y can be understood from considering the forces acting on the field-lines participating in the Dungey cycle,

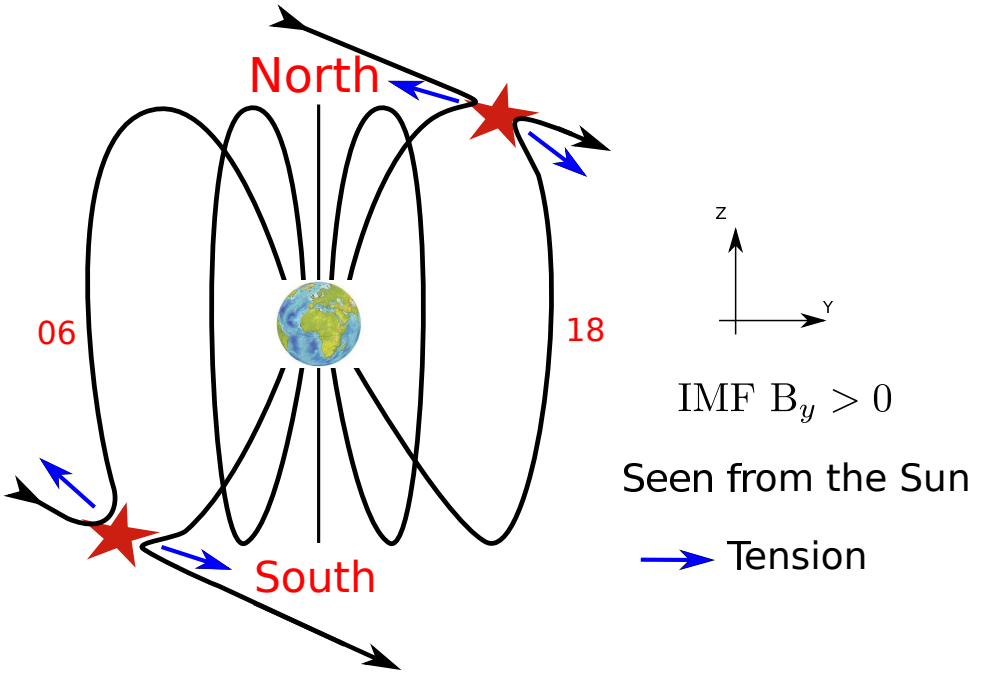

Figure 3.3: Reconnection geometry for southward IMF with a positive B_y-componenet. Magnetic tension forces on the newly opened field-line will point in opposite directions in the two ends (north and south), affecting the magnetosphere differently in the two hemispheres.

being the tension and magnetic pressure forces as described in Chapter 2. This was discussed in detail by *Cowley* [1981a] who attributed the IMF B_y asymmetries in ionospheric convection patterns on the dayside to the action of magnetic tension forces on the newly opened field-lines. When IMF is southward and has a significant B_y component, the magnetic flux-circulation deviates from the 2D meridional picture in Figure 2.1. The magnetic tension force on a newly opened field-line on the dayside will now have a substantial y-component pulling it towards dawn or dusk depending on the sign of IMF B_y. Importantly, this y-directed tension will also be opposite in the two ends (north and south) of the field-line that was recently opened. The dayside reconnection geometry for this situation is sketched in Figure 3.3 where the opposite tension forces are indicated with blue arrows. For positive IMF B_y, this results in moving magnetic flux from the northern hemisphere dayside dusk merging site toward the northern hemisphere high-latitude lobe on the dawn side. Due to the reconnection geometry, this will be opposite in the southern hemisphere. Magnetic flux is efficiently eroded from the dayside merging region and added asymmetrically to the lobes in the two hemispheres. This can be seen in Figure 3.4 where the magnetic pressure derived from a global MHD simulation is shown on a spherical shell of $8R_E$ centred at the Earth. Fig-

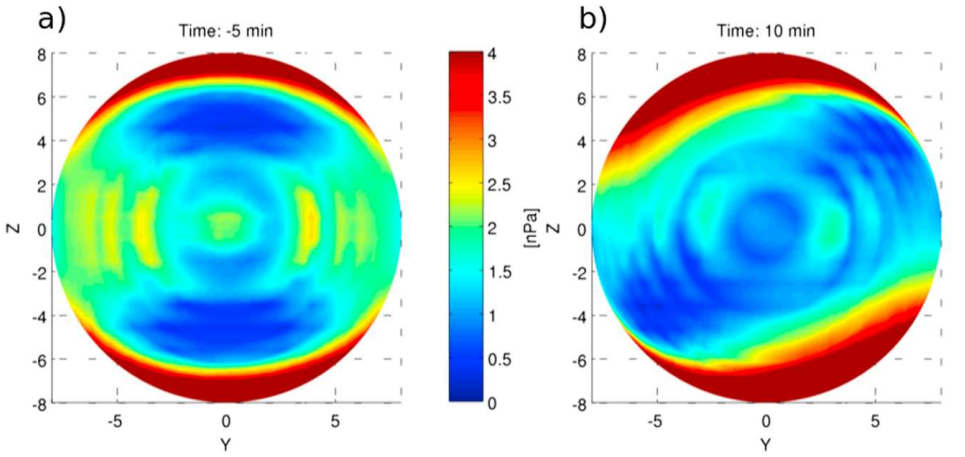

Figure 3.4: Magnetic pressure from MHD simulation projected on a half sphere centred around Earth with radius 8 R_E. The center of the plot therefore corresponds to $x = 8$ R_E. (a) Prior to arrival of IMF B_y the pressure distribution is north-south symmetric. (b) 10 min after arrival of IMF $B_y = 10$ nT a large north-south asymmetry is seen towards the edges, corresponding to locations at $x \sim 0$.

ure 3.4 is the same as Figure 3 in Paper III. Figure 3.4a) shows the magnetic pressure from a MHD simulation run with purely southward IMF. It clearly shows a symmetric magnetic pressure distribution between the two hemispheres. Figure 3.4b) shows the simulated magnetic pressure distribution 10 min after the arrival of a 10 nT IMF B_y at the magnetopause (IMF clock angle $= 135°$). Now one can clearly see the signature of asymmetric erosion of flux at the dayside (blue) and asymmetric loading of magnetic flux at high latitudes towards the edges (red) where $x \sim 0$ since the figure is a half-sphere.

The induced By within the closed magnetosphere is explained as a result of the asymmetric magnetic pressure distribution. Although confined to a limited region in space (close to the terminator plane), the enhanced magnetic pressure due to the asymmetric loading immediately forces incoming and surrounding field-lines to accelerate, affecting a large region, as the magnetosphere attempts to restore pressure balance. In Figure 3.5 (Figure 3a from *Liou and Newell* [2010]) the asymmetric loading process and its effect on the magnetospheric convection and magnetic field is illustrated for the IMF $B_y > 0$ situation. Here, a cross-section of the magnetotail is seen looking from the tail toward the Earth. The magnetosphere responds to the asymmetric loading of flux by imposing magnetospheric convection to restore pressure balance, indicated by the bold arrows in the lobes. The asymmetric lobe convection eventually affects the closed field-lines (grey region), representing a shear flow. These shear flows (bold arrows in-

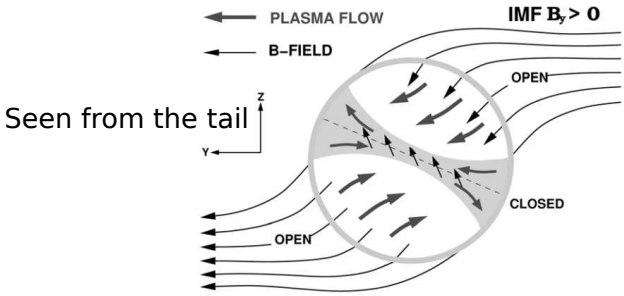

Figure 3.5: Asymmetric loading of magnetic flux in the tail durting IMF $B_y > 0$ leading to asymmetric convection in the two lobes. Closed field-lines (grey region) are affected from the different convection in the two lobes resulting in a velocity shear on closed field-lines (bold arrows inside grey region) leading to an induced B_y on closed field-lines. Adopted from Figure 3a in *Liou and Newell* [2010].

side the grey region) lead to the induced By as the field is forced in opposite directions in the northern and southern part, seen by the thin arrows in the central part of Figure 3.5. Hence, B_y can be induced independent of reconnection in the tail. In response to this asymmetric forcing, the ionospheric footpoints will move in opposite directions in the two hemispheres, leading to a longitudinal displacement of conjugate points from the symmetric configuration, which is frequently observed. The neutral sheet is located where the field-lines have their apex, sandwiched between the regions of asymmetric forcing. A pressure balance exist across the neutral sheet forcing it to rotate in response to the asymmetric forcing. This is indicated by the dashed line in Figure 3.5. We note that this description of how B_y is induced on closed field-lines is consistent with what was described by *Khurana et al.* [1996]. As B_y on closed field-lines can be explained through the induced shear flows, we believe that the frequently used term 'IMF B_y penetration' is misleading as the B_y field is not simply a result of vacuum superposition. Therefore we will use the term *induced* B_y.

Having described how a B_y component is induced into the closed magnetosphere, we will now present the 'process of restoring symmetry'. This is a dynamic description of how the stress stored in a closed field-line (having induced B_y and hence asymmetric footpoints) dissipates preferentially into one hemisphere. This leads to asymmetric convection and BCs into that hemisphere. This process is what was mentioned earlier as the updated understanding of the induced B_y effect and represents a more detailed description of the IMF B_y influence first suggested by *Stenbaek-Nielsen and Otto* [1997].

The process of restoring symmetry is schematically illustrated in Figure 3.6. This is the same as Figure 2 in Paper IV and is adopted from Paper III. The upper part of this figure shows a field-line in the tail and how it is connected to the two polar

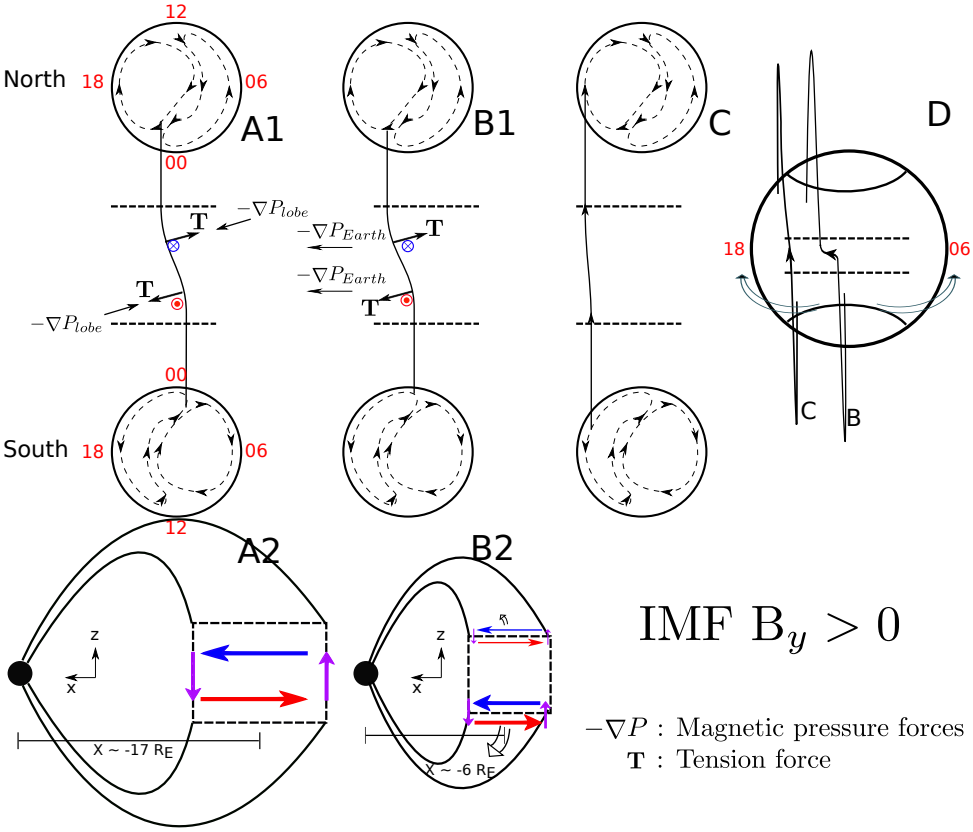

Figure 3.6: A-C: Evolution of a closed field-line with asymmetric footpoints in the dusk convection cells during IMF B_y positive conditions. The upper panels show how a field-line with asymmetric footpoints connects to the dusk convection cells in the two hemispheres at three different times. The lower panels (A2, B2) show the associated current systems with colored arrows, seen from the dusk side. A1: In the mid-tail region the asymmetric pressure forces due to IMF B_y ($-\nabla P_{lobe}$) and the magnetic tension forces (**T**) on the field-line balance. Currents close locally as indicated in A2. B1: At a later stage the field-line moves earthward and is affected by the gradient of the total pressure surrounding the Earth (plasma and magnetic field, $-\nabla P_{Earth}$). Now the forces do not balance. In the Southern Hemisphere the indicated forces point in the same direction. Hence, most of the stress is transmitted into this hemisphere and the southern footpoint will catch up with the northern counterpart to restore symmetry, as seen in C. D: The situation in B and C viewed from the tail. This figure is the same as Figure 2 in Paper IV and is adopted from Paper III.

hemispheres. In this projection the magnetosphere is the region between the two polar regions, and the apex of the field-line is located between the two horizontal dashed lines in each panel. Figure 3.6A1 shows a field-line in the mid-tail having asymmetric footpoints during IMF B_y positive. This is a result of the shear plasma flows between the two hemispheres induced by the asymmetric loading [*Khurana et al.*, 1996; *Liou and Newell*, 2010], illustrated by the $-\nabla P_{lobe}$ force. For this field-line the force is balanced by the tension acting on the curved field-line, **T**. Associated with this illustrated bend close to the field-line apex due to the induced B_y, Ampère's law requires a current in the x-direction, as illustrated by the red and blue arrows in and out of the page. Figure 3.6A2 shows the same field-line in the meridional plane, seen from the dusk side. Again, the apex of the field-line is indicated with dashed lines. We here consider an idealized extent in the x-direction of the induced B_y, meaning that B_y is zero on either side of this box. This requires a pair of currents in the z-direction, as indicated by the purple arrows. In this situation, when the forces balance (Figure 3.6A1), one can see that the current closes locally and no field-aligned current into the ionosphere is present.

A later stage in the evolution of this field-line is presented in the two B panels. Now the field-line has convected closer to Earth, and we consider a field-line convecting earthward on the dusk side. Closer to Earth, the forces from the asymmetric loading decreases and the forces from Earth's total pressure (plasma and magnetic), $-\nabla P_{Earth}$, becomes important. This pressure gradient has a duskward component along the entire field-line as we have chosen to consider a field-line on the dusk side. In this situation $-\nabla P_{Earth}$ and **T** add in one end of the field-line but subtract in the other end. Now, the stored B_y-stress in the field-line will mostly propagate in the direction where the forces add, being the southern hemisphere in this situation. The release of stress due to force-imbalance will likely occur gradually as the field-line convects toward the dayside and will be released as Alfvèn waves with a current system associated with it (due to the gradients in B). This is illustrated in Figure 3.6B2. The ionospheric signature will be faster convection in the hemisphere receiving the stress since one footpoint will need to travel further to catch up as symmetry is restored. This will also lead to increased BCs as the direction of BCs associated with the stress release (Figure 3.6B2) will always be in the same direction as the pre-existing Region 1/ Region 2 (R1/R2) BCs associated with the ionospheric convection channel [*Iijima and Potemra*, 1978] (upward/downward BC in the poleward/equatorward part of the convection channel for this case). This process will continue until the stress is dissipated and the field-line has become symmetric again (symmetric footpoints), representing a lower energy state. The symmetric stage is illustrated in Figure 3.6C. In Figure 3.6D the situation in panels B and C is illustrated in a more realistic projection as seen from the tail toward the

Earth. For a field-line returning toward the dayside via dawn, most of the B_y-stress will be transmitted to the northern hemisphere during the positive IMF B_y situation (not shown here) using the same arguments as above. For opposite sign of IMF B_y, this reverses.

The process of restoring symmetry outlined above represents a magnetospheric process that affects the two hemispheres differently by imposing asymmetric convection and BC in conjugate regions. In order to investigate this effect using data, it is essential to know how the two hemispheres are magnetically connected, as this process is believed to become more important the more displaced the footpoints in the nightside are between the hemispheres. For this task, simultaneous global auroral imaging from both hemispheres can be of great value as the aurora serves to light up magnetically connected regions in the two hemispheres. From such data, the hemispheric displacement from quiet conditions can be estimated, sometimes in multiple locations.

This updated understanding of the effects of an induced B_y in the magnetosphere emerged from the observations and explanations from *Liou et al.* [1998]; *Østgaard et al.* [2004, 2005]; *Shue et al.* [2001]; *Stenbaek-Nielsen and Otto* [1997], and Paper I. The process of restoring symmetry describes the effects in terms of asymmetric stress release leading to asymmetric convection and BCs. Therefore, any associated auroral signatures is likely a result of these processes. Hence, it is highly relevant to survey literature investigating the relationship between these quantities (convection and BCs) and IMF B_y to investigate the importance of the restoring symmetry process.

The most similar physical process described in the literature is the azimuthal fast plasma flows observed in both the ionosphere and magnetosphere along a field-line on the nightside during IMF B_y conditions [*Grocott et al.*, 2004, 2005, 2008, 2007; *Pitkänen et al.*, 2015]. Although first predicted by *Nishida et al.* [1998], these observations were interpreted as the necessary motion needed for one end of a field-line to catch up with the other end during the convective motion from the nightside toward the dayside. This is in fact the same process as we consider, only explained with less details. We note that the aforementioned observations were mainly during northward IMF conditions. Although being less investigated, northward IMF in combination with a B_y-component is expected to stir, or rearrange magnetic flux asymmetrically (in contrast to add asymmetrically during southward IMF) [*Burch et al.*, 1985; *Crooker and Rich*, 1993; *Reiff and Burch*, 1985]. This will also eventually lead to asymmetric field-lines in the nightside [*Milan*, 2015] with asymmetric footpoints [*Østgaard et al.*, 2011b]. However, this thesis only consider the southward IMF case in detail.

The high-latitude current systems (horizontal and field-aligned) have also been extensively investigated in response to IMF direction and season [e.g. *Friis-Christensen and Wilhjelm*, 1975; *Green et al.*, 2009; *He et al.*, 2012; *Lukianova et al.*, 2012]. These

studies all show results indicative of influence from the process of restoring symmetry.

To explore the validity of the updated understanding of the system response to IMF B_y, we conducted a case study to investigate the predictions in an event when the field-lines in the nightside were highly displaced from its symmetric configuration. This is reported in Paper IV.

Chapter 4

Global auroral imaging

This chapter discusses the use of auroral imaging as a tool for investigating magnetospheric processes. Global auroral imaging from space is the main instrumentation used in this thesis. Although capable of remote sensing a large portion of the magnetosphere, the data has undergone extensive processing and its interpretation in terms of physical quantities are subject to assumptions. In this chapter we explain how the data is processed and can be interpreted for the purposes relevant for this thesis.

4.1 Instrument design

4.1.1 IMAGE FUV

For imaging in the northern hemisphere, the FUV [*Mende et al.*, 2000a] (Far Ultraviolet, $100-200$ nm) instrument suite on the IMAGE spacecraft [*Burch*, 2000] is used. It consists of three cameras observing FUV emissions at different wavelengths. In this thesis we mainly use the Wideband Imaging Camera (WIC) [*Mende et al.*, 2000b] as it provides the best signal to noise ratio. WIC is sensitive to the Lyman-Birge-Hopfield (LBH) band from N_2 and a few atomic N-lines in the 140-190 nm range. The bright Oxygen line at 130.4 nm is almost entirely excluded. The FUV instrument suite also consists of the Spectrographic Imager 12 (SI12) measuring the Doppler shifted Lyman$-\alpha$ line at 121.8 nm and rejecting the geocoronal 'cold' Lyman$-\alpha$ [*Mende et al.*, 2000c]. The measured signal is therefore only due to proton precipitation. The third camera, the SI13, measures the atomic Oxygen line at 135.6 nm, spectrally separated from the bright atomic Oxygen line at 130.4 nm.

The orbit of the IMAGE satellite is highly elliptical with a 90.0° inclination such that the entire auroral zone is observed from apogee. The satellite has a 123 s spin period ($3^\circ s^{-1}$). For the WIC camera, the Field-Of-View (FOV) is 30° in the direction of rotation and 17° in the perpendicular direction. Each stationary feature therefore

spends 10 s within the FOV. To take advantage of the entire period the camera looks at the aurora, a single image is put together by superimposing raw images taken at 30 frames per second, and suitably offsetting from one image to the next to compensate for the spacecraft rotation in a process known as Time Delay Integration (TDI) [*Mende et al.*, 2000a]. The final WIC image has 256×256 pixels corresponding to a pixel size of ~ 100 km at apogee. The two SI cameras share primary optics. Their FOV is $15^\circ \times 15^\circ$, integration time is 5 s, and their final image has 128×128 pixels.

The pointing of the camera is calculated from attitude data coming from the on-board star-tracker. Further minor corrections were applied so that the predicted location of a known FUV star aligned with its observed location in the image, limited by the point spread function whose full width at half maximum was 2 pixels for WIC. This correction was done on a routinely basis by the IMAGE FUV team, but instances where the pointing is bad still exist in the dataset. For the case studies presented in Papers I and IV we manually checked that the pointing was reliable. This was not done in the statistical study in Paper II. However, we did a manual inspection of all processed images entering the statistics and removed images when the pointing was obviously wrong. Knowing the pointing of each pixel and the spacecraft location, each pixel on Earth gets a geographic coordinate assuming that the height of the aurora is 130 km. For analysis purposes, it is convenient to present the image on a magnetic grid. The locations are therefore converted to MLAT/MLT (Magnetic Local Time) coordinates based on a realistic magnetic field model using modified apex coordinates [*Richmond*, 1995; *VanZandt et al.*, 1972]).

To account for environmental and instrument variations throughout the mission, the processing scheme takes into account the present temperature and applied voltages. Also, imaging of FUV stars with known luminosity is used to monitor the sensitivity of the detector. To correct for sensitivity variations across the detector a flat-field correction is applied. The flat-field variations change with time and are determined from images of the Earth from Perigee passes where both the satellite zenith and solar zenith angles are roughly constant across the image. These corrections are built-in features in the FUVIEW3 software[1] that we use to obtain the images. After these corrections, the images are represented in what is often referred to as *corrected counts*. Throughout this thesis we only use the term *counts* when discussing the camera intensities, although it refers to the *corrected counts* unless otherwise specified.

Before a value of the auroral luminosity can be obtained one must remove signals from non-auroral sources. Scattered sunlight from the atmosphere as well as FUV emissions from atmospheric states excited by solar EUV radiation represent the day-

[1]Can be obtained from the IMAGE FUV website: `http://sprg.ssl.berkeley.edu/image/`

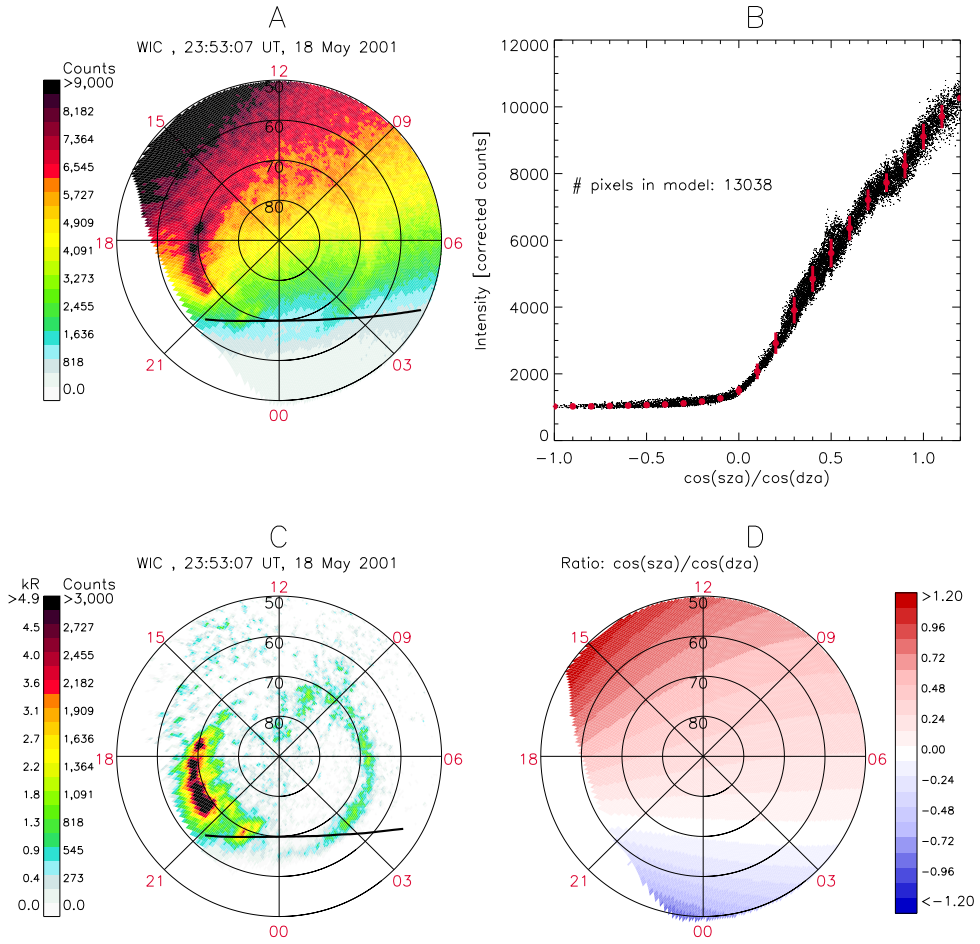

Figure 4.1: An example showing how the background from non-auroral sources in the WIC image is subtracted. A: The original image from FUVIEW3 in corrected counts mapped on a magnetic MLAT/MLT grid. B: Intensity from pixels outside the auroral oval as a function of the ratio cos(sza)/cos(dza). Pixels in the auroral zone are assumed to follow the same dependence of this ratio. C: The image with the modelled background subtracted. D: The distribution of the ratio over the high-latitude region. This is the same image as shown in Figure 4A in Paper IV.

glow signal in the images. We remove the dayglow and the now flat background separately for each image as the flat background varies with time. To remove contributions from dayglow in regions where also auroral emissions occur, a model of the dayglow is first constructed. The dayglow intensity in a pixel is proportional to the cosine of the Solar Zenith Angle (SZA) at that pixel [e.g. Figure 13 in *Meier*, 1991]. In addition, the intensity also increases for increasing Satellite Zenith Angle (DZA) as the atmosphere is optically thin in wavelengths dominating the WIC signal. This relationship has been found empirically to be close to $\cos^{-1}(DZA)$ for the WIC camera. Hence, the dayglow intensity is roughly proportional to the ratio $\frac{\cos(SZA)}{\cos(DZA)}$. How the dayglow intensity varies as a function of this ratio is shown as black dots in Figure 4.1B for pixels outside the auroral oval, obtained from the image shown in Figure 4.1A. One can see that there is a linear relationship for values of the ratio greater than ~ 0.1. Below this value the curve flattens out, corresponding to the flat noise floor in the detector as no dayglow is seen on the nightside. The median intensity within 0.1 wide increments of the ratio is shown as red dots with the corresponding ± 1 standard deviation. This model, represented by the red dots, can then be used on pixels where also auroral activity occurs as their dependence on the ratio should be the same. The dayglow intensity for auroral pixels is found from the model by linear interpolation between the red dots for the ratio of the corresponding pixels, and then subtracted. Figures 4.1A and 4.1C show the image before and after the modelled background has been subtracted, respectively. Figure 4.1D shows how the ratio varies in the mapped image. In making Figure 4.1 only pixels $< 70°$DZA are drawn on the map and used in the model. For larger DZA the method performs less accurate. This is likely due to a combination of different effects as e.g. limb brightening/darkening [*Frank and Sigwarth*, 2003] and errors from inaccurate pointing.

After subtracting the background (noise floor + dayglow), the remaining signal represents the auroral emissions, still in units of counts. Auroral brightness is frequently represented in the unit of *Rayleigh*, or column intensity, where $1R = 10^6 \frac{photons}{cm^2 \cdot s}$ from a column of unspecified length [*Hunten et al.*, 1956]. From in-flight calibration using stars with known FUV spectra, it was found that in the region of maximum spectral response of WIC (around 150 nm), 1 kR ($10^9 \frac{photons}{cm^2 \cdot s}$) produced 613 counts during the 10 s exposure. We note that the kR values determined for WIC does not directly compare with other FUV instruments, as the number of photons is highly dependent on the spectral width of the instrument and which lines observed.

How the signal from auroral emissions can be related to physical quantities associated with the particle precipitation (average energy and energy fluxes) is discussed in section 4.2.1.

4.1.2 Polar VIS Earth

The Polar spacecraft [*Acuña et al.*, 1995] was launched in February 1996 into a highly elliptical polar orbit. Its apogee reached $9R_E$ and was initially located at 68°N and moved northward. Perigee was at 2 R_E and the orbital period was 18 h. Due to apsidal precession of the orbit, apogee eventually moved south and by 2001 it was located above the equator, still in a polar orbit. This configuration allowed imaging of the southern hemisphere aurora for up to a few hours each time Polar exited from perigee. During the work of this thesis a systematic search for conjunctions between IMAGE and Polar was performed. A total of ~ 600 intervals each more than 20 min were found where the two satellites are located above opposite polar regions at the same time while observing the aurora. Hence, the IMAGE/Polar conjunctions are by far the largest existing dataset of simultaneous global auroral imaging.

Since we use data close to perigee, a large FOV is desirable. The Polar spacecraft included two auroral imaging suites. The Ultraviolet Imager (UVI) [*Torr et al.*, 1995] observed the LHB-band, similar to IMAGE WIC. It had a narrow FOV so the entire oval was only seen around apogee. In the $1-2$ h after perigee when the southern hemisphere aurora could be seen, the UVI instrument only saw a fraction of the entire oval. The other imaging suite on Polar is the Visible Imaging System (VIS) [*Frank et al.*, 1995]. VIS is a set of three cameras. Two of them look at visible wavelengths of the aurora. The third camera is actually a UV camera and was included to monitor the directions of the FOV of the visible cameras. Hence, it had a relatively wide FOV. This is the camera we use on the Polar spacecraft, known as the VIS Earth camera.

Unlike IMAGE, Polar has a despun platform that the VIS Earth instrument is mounted on. Hence, it has the advantage of staring at the aurora all the time. Images are usually provided every 54 s using a 32.5 s exposure time. The VIS Earth camera is sensitive to the $124-149$ nm wavelength range [*Frank et al.*, 1995]. The brightest FUV line in the aurora is the 130.4 nm Oxygen emission [*Frey et al.*, 2003]. Hence, this is the main contributing emission to the VIS Earth signal [*Frank and Sigwarth*, 2003].

The VIS Earth images were downloaded from NASA's Space Physics Data Facility[2] and processed using the XVIS 2.40 software[3]. When presented, the VIS Earth images are plotted using the same magnetic coordinate system as used for the WIC camera (modified apex [*Richmond*, 1995]). A conversion factor of 4.32 counts/kR has been frequently used for this camera [*Laundal and Østgaard*, 2009].

[2] `ftp://cdaweb.gsfc.nasa.gov/pub/data/polar/vis/vis_earth-camera-full/`
[3] `http://vis.physics.uiowa.edu/vis/software/`

4.2 Interpretation

4.2.1 Relating the camera signal to particle precipitation

The auroral emissions observed by WIC and VIS Earth are caused by precipitating charged particles, mainly electrons, but to some extent also protons [*Hubert et al.*, 2001]. In principle, the signal (counts) measured by a camera is proportional to the convolution of the spectrum of emissions reaching the detector, $S(\lambda)\left[\frac{photons}{cm^2 \cdot s \cdot sr \cdot nm}\right]$, with the normalized spectral transmission profile, $T(\lambda) \in [0,1]$ for $\lambda \in [\lambda_{start}, \lambda_{stop}]$, to be known from laboratory calibrations, integrated over the passband and observed time [*Laundal*, 2010]:

$$counts \propto \int_0^t \int_{\lambda_{start}}^{\lambda_{stop}} S(\lambda) T(\lambda) d\lambda dt \tag{4.1}$$

One can see from this equation that the challenge in deriving physical information regarding the precipitation relies on resolving the spectral information of $S(\lambda)$ due to the precipitation, as the observed counts only give the integrated value, and $T(\lambda)$ and the calibration is generally known.

IMAGE FUV

For the FUV instrumentation on the IMAGE satellite, effort has been made to derive physical quantities of the precipitation based on the observations in different wavelengths together with the modelled response of the atmosphere due to particle precipitation [*Gérard et al.*, 2001, 2000; *Hubert et al.*, 2001, 2002; *Solomon*, 2001]. A detailed presentation of this procedure leading to maps of mean electron energies and energy fluxes of protons and electrons separately, was given by *Frey et al.* [2003]. In the following we touch on some of the physics and limitations in deriving the precipitation characteristics using the IMAGE FUV instrument suite. Although the papers in this thesis are not taking full advantage of the method outlined in this subsection, its description is included here to provide understanding of what the camera eventually observes.

How the atmosphere respond in FUV wavelengths to particle precipitation was simulated for electrons by *Solomon* [2001]; *Solomon et al.* [1988] and protons by *Gérard et al.* [2000]; *Hubert et al.* [2001]. The energetic charged particle interaction with the atmosphere is a highly complex problem. In order to obtain excitation rates one has to consider how the primary energy flux degrades and produces secondary electrons and neutral H beams. One limitation when modelling the atmosphere response is the inability to estimate the incident mean proton precipitation energy, unless higher spec-

tral resolution images than what provided by the IMAGE FUV instrument are available. Although proton precipitation is generally less efficient in generating FUV emissions, it can in some cases (most important during quiet conditions [*Hubert et al.*, 2002]) constitute a significant part of the WIC and SI13 signal as secondary electrons are produced due to proton precipitation resulting in emissions in the LBH band and from atomic Oxygen and Nitrogen [*Frey et al.*, 2003; *Hubert et al.*, 2001]. One therefore needs to subtract the contributions from proton precipitation in the WIC and SI13 images before inferring information regarding the electron precipitation. When accounting for this, the model needs to assume an average proton energy and energy distribution as this determines the altitude of energy deposition and hence how much absorbed the signal will be as it propagates back to the imager in space. In the FUV wavelengths, O_2 is an important absorber agent at altitudes below 150 km [*Meier*, 1991]. Hence, its altitude profile is an important part of the atmosphere model.

For a unit proton energy flux ($1\ mW/m^2$) with an assumed mean energy of the precipitating protons (also assuming the protons follow a Kappa distribution with $\kappa = 3.5$), $S(\lambda)$ due to the proton precipitation is provided by the model [see e.g Table I in *Frey et al.*, 2003]. Using the camera calibration, $S(\lambda)$ can be convolved with the respective instrument passband $T(\lambda)$ (Equation 4.1) for each of the FUV cameras to calculate the expected signal per unit proton energy flux. To subtract the proton signal in WIC and SI13 one must first estimate the energy flux of the precipitating protons. Since the SI12 channel was designed to only measure the Doppler shifted Lyman$-\alpha$ line at 121.8 nm, its entire signal is due to the precipitating protons. Using the above assumptions and model results, one can estimate the precipitating proton energy flux $\left[\frac{mW}{m^2}\right]$ directly from the observed count rates in SI12 by dividing it by the count rates per unit energy flux for the given mean energy.

As the contribution to the WIC and SI13 signal from protons can be determined and subtracted when knowing the precipitating proton energy flux, one is left with a signal originating from only electron precipitation. Based on the atmospheric model, the FUV spectral response to electron precipitation can be determined assuming a Maxwellian distribution of electrons inside the loss cone [see e.g.Table II in *Frey et al.*, 2003]. Since we have two independent measurements of the electron precipitation (WIC and SI13), two quantities can be determined (mean energy and energy flux). Again, using the in-flight calibrations from stars with known FUV intensity, the WIC and SI13 response (counts) for 1 $\frac{mW}{m^2}$ electron precipitation can be estimated from the atmosphere model as a function of mean energy. Although the energy flux is yet unknown, the ratio of the two cameras shows a clear energy dependence, linear in the $3-30$ keV regime [Figure 7 in *Frey et al.*, 2003] and can be used to estimate the average energy for each pixel. Having the mean electron energy, one can finally estimate the electron energy

flux for each pixel by dividing the observed count rate by the count rate from the model obtained using the estimated mean energy for 1 mW/m^2 electron energy flux.

The energy dependence on the observed FUV spectrum $S(\lambda)$ is related to

1. Emission rates at the energy deposition altitude. Higher energies deposit their energy at lower height. This affects LBH and the 135.6 nm emissions differently as the N_2 density increases toward the ground while the O density decreases

2. Absorption of the signal on its way to the detector. Absorption by O_2 is more efficient at lower altitudes as the O_2 density increases toward the ground.

The altitude profiles of N_2, O, and O_2 are therefore important quantities going into the model. However, the altitude profiles of these species are known to vary with geomagnetic activity, reducing the O/N_2 ratio during geomagnetically active periods [*Drob et al.*, 1999; *Strickland et al.*, 1999]. Hence, one should exercise care when adopting the model values for $S(\lambda)$ from *Frey et al.* [2003], being inferred from moderately disturbed geomagnetic conditions. However, *Frey et al.* [2003] conclude that this method usually provides values within a factor 2 when compared to in-situ particle measurements.

VIS Earth

We are not aware of any published detailed information regarding the instrument passband $T(\lambda)$ in VIS Earth (from now referred to as only VIS). Our knowledge of the VIS response is based on Table I in *Frank and Sigwarth* [2003] showing the relative response in VIS when viewing from nadir at the dayglow. Then, 83% of the response is due to the 130.4 nm atomic Oxygen line, 7% from the 135.6 nm atomic Oxygen line, and 9% from the LBH band. According to *Meier* [1991] Table 2, the average daytime FUV dayglow seen from nadir at 600 km above the equator has the corresponding intensities: 10498 R for 130.4 nm, 1068 R for 135.6 nm, and 4560 R for the entire LBH band. However, the VIS passband only covers the short wavelength part of the LBH emissions at $124 - 149$ nm [*Frank et al.*, 1995]. In that spectral region, the LBH intensity is only 1756 R.

However, we are only interested in emissions due to particle precipitation (aurora). The modelled intensity (R) of these lines from emissions produced by electron precipitation during moderately disturbed geomagnetic conditions per unit energy flux can be found in Table II in *Frey et al.* [2003]. Their modelled spectral intensity from electron

Table 4.1: Upper part: Average daytime FUV spectrum of dayglow during moderately active solar conditions, looking nadir from 600 km at 130.4 nm, 135.6 nm, and LHB band [*Meier*, 1991]. The fraction of each line or band to their total intensity is shown, to be compared to the relative response to dayglow in VIS as presented in *Frank and Sigwarth* [2003]. Values in parenthesis represent the case when only emissions within the VIS passband are considered. Lower part: Spectral response to 1 mW/m^2 electron precipitation for various mean electron energies taking atmospheric absorption into account [from Table II in *Frey et al.*, 2003]. The fraction of each line or band to the total intensity is shown. In the lower part the LBH emissions refer to the WIC passband.

	130.4 nm	**135.6 nm**	**LBH**	**Total**
		Dayglow		
Intensity [R]	10498	1068	4560 (1756)	16126 (13322)
Fraction of total	0.65 (0.79)	0.07 (0.08)	0.28 (0.13)	
VIS response	83%	7%	9%	
		1 mW/m^2 electron precipitation		
0.2 keV: [R]	2907	756	1629	5292
Fraction of total	0.55	0.14	0.31	
1.0 keV: [R]	1606	440	2390	4430
Fraction of total	0.36	0.10	0.54	
5.0 keV: [R]	621	153	2320	3094
Fraction of total	0.20	0.05	0.75	
25.0 keV: [R]	116	18	1010	1144
Fraction of total	0.10	0.02	0.88	

precipitation is reproduced together with the dayglow intensities from *Meier* [1991] in Table 4.1. Based on the dayglow considerations, the spectral transmission profile $T(\lambda)$ must be rather flat across the passband as the relative VIS response reported by *Frank and Sigwarth* [2003] (see Table 4.1) closely resembles the relative contributions to the total brightness in the passband (parenthesis values in Table 4.1). To investigate the contributors to the auroral signal observed in VIS, one can once again look at the modelled auroral intensities from 1 mW/m^2 electron precipitation when taking atmospheric absorption into account [*Frey et al.*, 2003]. Their modelled spectral brightnesses are presented in the lower part of Table 4.1 for various energies. One can see that for 0.2 keV mean electron energy precipitation, the 130.4 nm line dominates the FUV spectra. However, as the mean precipitation energy increases, the LBH emissions dominate from around 1 keV. Based on the roughly flat response identified from the dayglow considerations, this suggest that when looking at aurora, being primarily caused by electron precipitation [*Germany et al.*, 1997; *Ishimoto et al.*, 1988], the VIS signal is likely dominated by the 130.4 nm OI line in regions of low energy precipitation. In regions of higher energies ($>$ 1 keV), LBH emissions might dominate.

One important note when discussing the LBH response in VIS is the fact that the VIS passband is only observing the short wavelength part of the LBH band. It is known that the O_2 absorption cross section is greater in the short wavelength part of the LBH band (e.g. Figure 47 in *Meier* [1991]) leaving that part of the LBH spectra more damped for higher energy precipitation. As the LBH brightness due to electron precipitation presented in Table 4.1 includes the longer wavelength LBH emissions in the WIC passband, the printed fractions of LBH intensity to the total intensity are likely too high when considering the VIS passband.

To summarize, the VIS response to electron precipitation is dominated by both 130.4 nm OI and LBH (short wavelengths). The relative importance of the two is unknown, but contributions from LBH is likely increasing for increasing mean energy.

4.2.2 Comparing auroral intensities in the two hemispheres

This thesis utilizes simultaneous global auroral imaging from both hemispheres to investigate the solar wind - magnetosphere - ionosphere coupling. It is therefore essential to know to what extent the auroral images from the two hemispheres can be compared. In Paper I and Paper IV we choose to present images from the WIC camera when comparing to the simultaneous VIS images from the southern hemisphere. As discussed in the previous subsection, the response to particle precipitation in VIS is known to a less degree than for the FUV instruments. We know, however, that both the 130.4 nm and LBH (short) emissions contribute to the VIS signal, where the 130.4 nm line

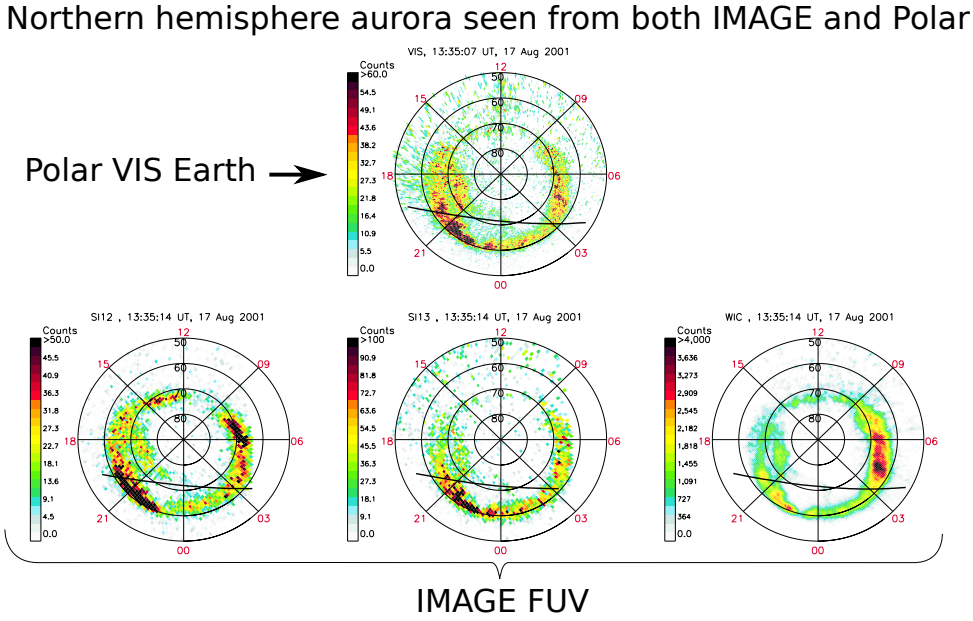

Figure 4.2: An example of the northern hemisphere aurora observed from both IMAGE FUV and Polar VIS Earth cameras.

have the greatest response during soft precipitation (< 1 keV). For harder precipitation, the VIS camera sensitivity to LBH emissions increases, but to an unknown extent. In the nightside region during active geomagnetic conditions (which was the case in Paper I and Paper IV), the mean energy of the electron precipitation is usually of the order of several keV [*Chua et al.*, 2001; *Hardy et al.*, 1985]. Also, the winter hemisphere is known to exhibit harder precipitation than the summer hemisphere [*Newell et al.*, 2010], further motivating the comparison of VIS against WIC when VIS is in the winter hemisphere. Together with the better signal to noise ratio and four times more pixel elements in WIC compared to SI12 and SI13, this represent the motivation of presenting the VIS images together with WIC.

To illustrate how VIS responds compared to the IMAGE FUV instrumentation, one can look at simultaneous images from the same hemisphere. One example is shown in Figure 4.2 where the northern hemisphere aurora on August 17, 2001 is captured by both spacecraft. The VIS image is shown in the top row and compared with images from the three FUV cameras. The center of exposure time is only differing by 7 s in this example. The WIC image closely resembles the features that are simultaneously observed in VIS. Furthermore, the combination of fewer pixel elements and poorer signal to noise ratio makes it harder to identify structures in SI12 and SI13 compared to WIC. When comparing the intensity distribution, WIC seems to observe an overall

similar brightness distribution as VIS. However, relatively brighter aurorae are seen in the dawn region in WIC compared to VIS. Also, relatively brighter aurora are seen close to 18 MLT in VIS compared to SI13. This example serves to illustrate that comparing intensities between the two cameras are not straight forward. However, identifying the same features proves to be a much easier task, especially when using the WIC camera.

The different spectral sensitivity of WIC and VIS will likely result in a different instrument response when the altitude profiles of N_2, O_2, and O change for the reasons presented in the previous subsection. Since the two hemispheres are not symmetric with respect to solar illumination and magnetic field strength, possibly affecting the O/N_2 ratio, it is clear that a fixed relationship between counts (or kR) in WIC and VIS can not be used to firmly establish intensity asymmetry, as this will vary with time. In Paper I we therefore restricted the analysis to only consider cases when an auroral feature appeared to be absent in one hemisphere in a region where conjugacy could be firmly established from the similarity of surrounding auroral forms.

4.2.3 Identification of conjugate regions

One of the biggest advantages of conjugate auroral imaging is the ability to identify truly conjugate regions as the aurora serves to light up magnetospheric processes. Thus, one does not need to rely on a modelled trajectory of the magnetic field-line from one hemisphere to the other. The inferred mapping can therefore tell us about the geometry of the magnetosphere and provide useful context to complementary observations.

Nightside auroral features are frequently displaced in longitude [*Liou et al.*, 2001; *Østgaard et al.*, 2004, 2011b; *Stenbaek-Nielsen et al.*, 1972]. In order to objectively determine this longitudinal shift, we use a correlation analysis, similar to that presented in *Østgaard et al.* [2011a]. This method was used in both Paper I and Paper IV and can be explained as follows:

1. Transform a limited region in the nightside corrected images (typically 3-5 MLT sectors wide) into rectangular $m \times n$ matrices (north and south separately)
2. Calculate the correlation between vectors constructed from the simultaneous rectangular images
3. While holding one hemisphere fixed, step 1 and 2 is repeated with a 0.1 MLT shift in the other hemisphere
4. The longitudinal shift (in MLT) is determined from the shift giving the largest linear correlation

An example illustrating this process can be seen in Figure 4 in Paper IV.

4.2.4 Auroral intensity as a proxy for upward Birkeland current

Although the WIC and VIS response to proton precipitation may be significant in some regions as noted in section 4.2.1, the main signal is usually due to electron precipitation. This is especially evident in the poleward part of the dusk sector oval where the R1 BC is directed out of the ionosphere, carried by precipitating electrons [*Dubyagin et al.*, 2003; *Mende et al.*, 2003a, b; *Paschmann et al.*, 2002]. This region, the 12-24 MLT dusk sector, is also the region where monoenergetic electron precipitation (also known as inverted-V's, with typically keV energies) is most often seen [*Newell et al.*, 2009]. Electron precipitation with $\sim$ keV energy is the most efficient contributor to LHB emissions (Figure 7 in *Frey et al.* [2003]). Therefore, the WIC camera is highly sensitive to inverted-V precipitation. It has also been shown that the dark hemisphere on average receives more energy from particle precipitation than the sunlit hemisphere, where the difference is mainly due to increased mean energy rather than number flux, and most evident in the inverted-V precipitation [*Newell et al.*, 2010]. Therefore, the dusk side auroral emissions seen by WIC can be used as a proxy for the R1 BC density, especially during winter conditions when the current is carried by the electron energies responsible for making bright auroras. This is supported by *Ohtani et al.* [2009] showing a linear relationship between the precipitating electron enegy flux and the R1 BC density in the dusk sector. These are the arguments we use in Paper II when we suggest that the asymmetric auroral response in this sector due to IMF B_x could be related to the asymmetric SW dynamo. Further discussion on this topic is given in Chapter 5.

Chapter 5

Results and discussion

This thesis investigate the importance of two specific mechanisms responsible for hemispheric differences in the solar wind - magnetosphere - ionosphere coupling. In this chapter we first summarize the main findings from the papers with emphasis on how one result lead to the next. Then follows a section where we discuss the papers.

5.1 Summary of papers

5.1.1 Paper I

The first step in this investigation was to analyse the database of simultaneous global conjugate imaging. At that time this dataset was 10 sequences with durations from 1 to 5 h, adding to a total of 19 h, during active geomagnetic conditions. In Paper I we show that among the 15 features identified in this dataset, 7 could be related to the asymmetric SW dynamo mechanism, 5 could be related to the induced B_y effect, 3 were consistent with a third mechanism related to ionospheric conductivity, and two were not consistent with the influence from any of the three mechanisms considered. Because 2 features were consistent with two different mechanisms, the numbers add up to 17. Based on these results, our main conclusions was that 1) non-conjugate auroral features are common during active geomagnetic conditions and 2) the mechanisms considered can be important in describing asymmetries in the solar wind - magnetosphere - ionosphere coupling. However, the importance of the individual mechanisms can not be inferred from these case studies.

5.1.2 Paper II

Motivated by the findings from Paper I, a statistical study was performed to investigate the importance of the asymmetric SW dynamo mechanism. Although MHD mod-

elling has indicated a pronounced north-south asymmetric influence on the bow shock, magnetosheath and magnetopause during IMF B_x dominated conditions [*Peng et al.*, 2010], which is the regions where the region 1 currents are believed to originate (see section 3.1 for details and references), it has only been speculated that the asymmetric SW dynamo can affect the two hemispheres differently [*Cowley*, 1981b; *Laundal and Østgaard*, 2009]. If this mechanism really affects the aurora differently in the two hemispheres, we would expect the average auroral intensity to be affected during certain favourable conditions in specific locations. Paper II shows that this is indeed the case in both hemispheres. Although the difference between the auroral intensity in the poleward dusk sector for positive and negative IMF B_x is only moderate, the accumulative effect might be important since the results were obtained during conditions when $|\text{IMF } B_x| > 2$ nT, which is typically the case in the SW due to the typical Parker spiral configuration of the heliospheric current sheet [*Parker*, 1958]. Paper II is the first study of its kind aiming to directly investigate the importance of the asymmetric SW dynamo mechanism using observations. Similar investigations has been made from the northern hemisphere, but from a much smaller dataset. *Shue et al.* [2002] made similar average auroral plots (as our Figures 2 and 3 in Paper II) sorted by IMF B_x. During winter and southward IMF (corresponding to our selection criteria) they found a similar trend as we did in Paper II, namely stronger aurora in the northern hemisphere during IMF B_x negative compared to IMF B_x positive conditions. To our knowledge, the same analysis has never been done in the southern hemisphere before. The strongest indication that this is an effect of the asymmetric SW dynamo is that the hemispherical asymmetry is opposite for $B_x > 0$ and $B_x < 0$. Paper II is hence providing further support that this mechanism has a real effect on the aurora.

5.1.3 Paper III

When investigating the simultaneous aurora in the two hemispheres, identification of conjugate features is done on a routinely basis. As shown and discussed in section 4.2.2, the identification of conjugate features in WIC and VIS can often be done without ambiguity. The longitudinal displacement of conjugate features represent important context when analysing the global system, and has been shown to be strongly related to IMF B_y. We therefore pursued the investigation of the second mechanism introduced in Chapter 3, describing asymmetric effects of IMF B_y on the global system. Although it has been firmly established that the footpoints of a closed field-line can be displaced from the nominal configuration, the question of how and if this configuration could be related to asymmetric forcing of the two hemispheres has not been understood. This motivated the investigation that led to the description of how stress induced on closed

field-lines can dissipate preferentially into one hemisphere. In this work we used simulations from a global MHD model (the Lyon-Fedder-Mobarry (LFM) model [*Lyon et al.*, 2004]) to develop the theoretical description presented in this paper of how IMF B_y induces a B_y-component into the closed magnetosphere and how it leads to asymmetric currents and convection patterns in the two hemispheres. Paper III therefore lies the foundation of how we believe the two hemispheres can be forced asymmetrically when magnetic flux is added asymmetrically during southward and B_y dominated IMF.

This paper was written by Paul Tenfjord. My contribution was mainly in the discussions leading to the updated understanding of how the B_y-stress can be induced, and then dissipate asymmetrically.

5.1.4 Paper IV

To enhance our understanding of the theoretical framework presented in Paper III, Paper IV is an observational paper investigating, from both hemispheres, the global aurora, convection, and BCs when the nightside field-lines are highly displaced from the symmetric configuration. During the presented event, conjugacy is firmly established showing a very large longitudinal displacement of conjugate points, ΔMLT, of 3 h, being the largest displacement reported from auroral imaging. During this event, ionospheric convection measurements from SuperDARN (Super Dual Auroral Radar Network) were available in both hemispheres, and the nightside convection throat region was identified, also showing a 3 h MLT displacement between hemispheres. Line-of-sight (LOS) convection velocities derived from the SuperDARN observations also indicated faster sunward convection on closed field-lines in the dusk cell in the southern hemisphere compared to the conjugate region in the northern hemisphere dusk cell, consistent with the model presented in Paper III. Average BC maps from both hemispheres were also presented during the same seasonal and IMF conditions as the event. The hemispheric differences in BC density closely resembled the predicted influence as suggested in Paper III, indicating the importance of this mechanism, here referred to as the 'process of restoring symmetry', referring to the gradual asymmetric dissipation of magnetic stress as a field-line return to the dayside and becomes more symmetric. It is important to realize that the description outlined in Paper III and Paper IV is consistent with what has been shown earlier regarding how the two hemispheres respond during periods of significant IMF B_y. Our contribution is to give a better explanation of the dynamic processes leading to the observed asymmetric response.

5.2 Discussion of papers

5.2.1 The validity of using global auroral images as a proxy for upward Birkeland current

Most important for our interpretation regarding the asymmetric SW dynamo is whether the observed auroral signal can be interpreted as a proxy of the upward BC density. This interpretation requires knowledge of the characteristics of the particle precipitation that is not directly measured. To provide further insight into the relationship between the upward BC, the precipitating particle spectra, and the auroral signal in the poleward part of the dusk side oval (where we expect to observe signatures from the asymmetric SW dynamo), we will here present an event that illustrates this correspondence.

Although not included in any of the papers in this thesis, we have investigated the WIC response to upward BC in the dusk region in more detail. By simultaneously estimating the BC from both in-situ particle measurements and in-situ magnetic field measurements, we investigate the particle carriers of the BC in an event also observed by IMAGE WIC. In Figure 5.1 we show an event from October 26, 2000 where the FAST sattelite (Fast Auroral SnapshoT Explorer [*Pfaff Jr*, 2001]) entered the northern hemisphere auroral oval from the polar cap at around 21 MLT. Low resolution FAST data were downloaded from the FAST webpage[1] at spin (5 s) resolution. Simultaneous images from WIC are shown in Figures 5.1A-D with the FAST track and position overlaid. In this event, the auroral oval resembles quite well the average large-scale R1/R2 upward BC pattern [e.g. *Iijima and Potemra*, 1978]. In the dusk sector, the aurora is seen more poleward compared to the dawnside oval, consistent with the average locations of the upward R1 and R2 BC, respectively.

In Figure 5.1E-F energy spectrograms of electrons within the loss-cone ($0-30^\circ$ pitch angle) and opposite to this direction ($150-180^\circ$ pitch angle) are shown, respectively. One can see that the precipitating fluxes mostly dominates within the oval. In Figure 5.1E, a broadband energy spectrum [*Chaston et al.*, 2000] is seen just at the boundary of the oval followed by inverted-V spectra [*Frank and Ackerson*, 1971] of monoenergetic precipitation [*Newell et al.*, 1996]. From the east-west component of the magnetic field perturbations, the BC density is estimated using Ampére's law in 1D and shown in Figure 5.1G (assuming the current sheets are east-west oriented). Note that there is a data-gap just when the spacecraft crosses into the oval of 20 s in the magnetic data and 5 s in the particle data. By calculating the number flux for each of the 47 energy channels $n(E,t)[\#/m^2 \cdot s]$ from the electron and ion spectra in the two directions (up and precipitating, see Figures 5.1E and 5.1F), the resulting in-situ current density

[1] `http://sprg.ssl.berkeley.edu/fast/scienceops/cdf_download.html`

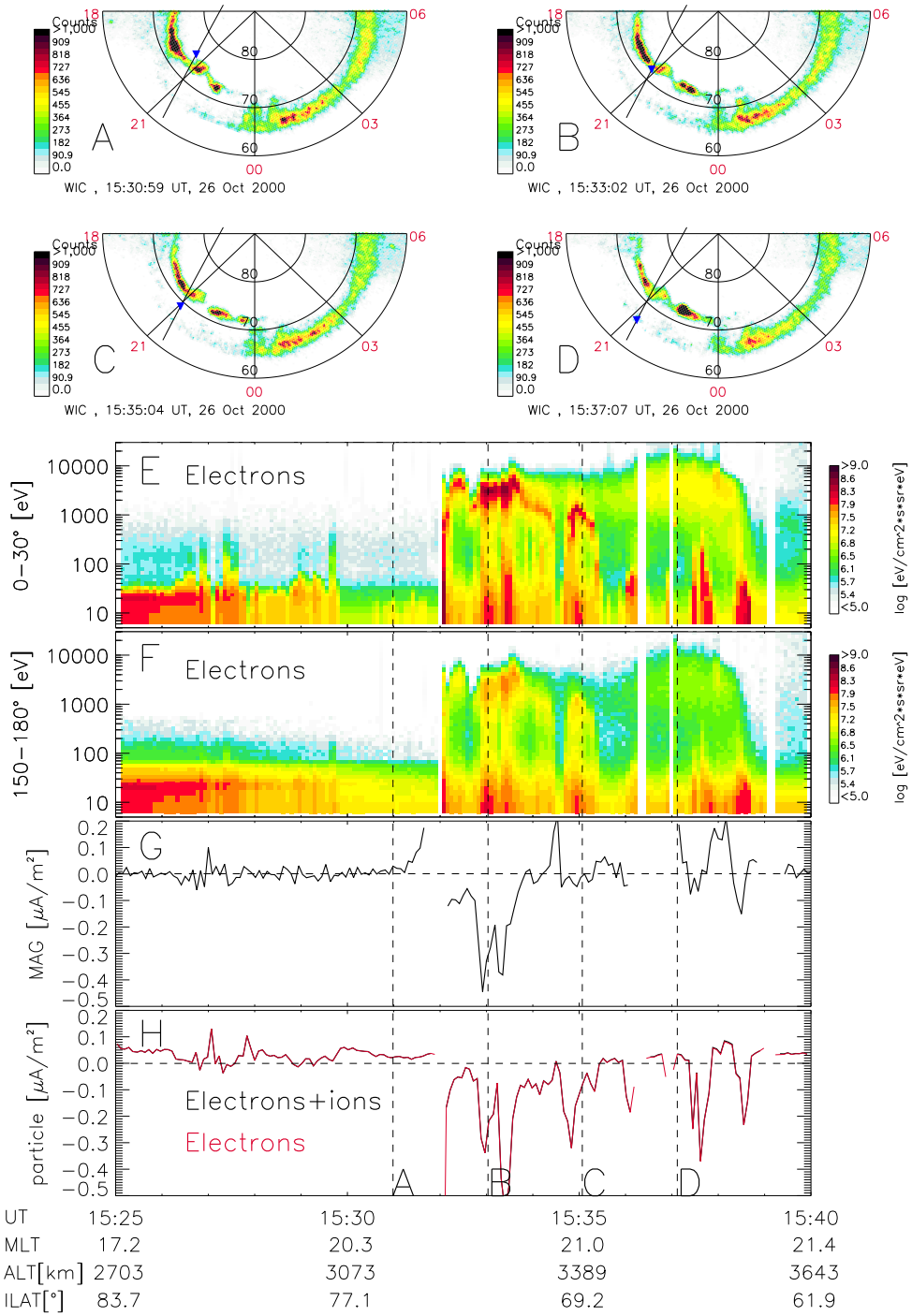

Figure 5.1: A-D: IMAGE FUV-WIC images from October 26, 2000 with the footpoint of FAST indicated. Panel E and F show energy spectrograms of electrons within the loss-cone ($0-30°$ pitch angle) and escaping electrons ($150-180°$ pitch angle), respectively. G: BC density derived from the east-west component of the magnetic field perturbations. H: BC derived from the electron and ion spectrometer data from the two directions in panels E and F.

$j[A/m^2]$ (positive into the ionosphere) is derived through

$$j(t) = \int_E q_i \Big[n(E,t)_{precipitate,i} - n(E,t)_{up,i} \Big] - q_e \Big[n(E,t)_{precipitate,e} - n(E,t)_{up,e} \Big] dE \tag{5.1}$$

where q_i and q_e is the ion and electron charge, respectively, both set to 1.6×10^{-19} C (assuming only electrons and protons). The result is seen in Figure 5.1H. The black line includes the contribution from ions, the red line is when only considering the electrons in equation 5.1. One can see that the ions do not carry a significant current in this energy range [5 eV - 24 keV].

Comparing the BC derived from the particle measurements (Figure 5.1H) to the BC derived from the magnetic perturbations (Figure 5.1G) a good correspondence is seen. For the upward current (negative values) the temporal development as well as the magnitudes compare quite well between the two. The downward current, however, is not easily seen in the particle derived BC. Since only low resolution data were available from the website for this event, this result is expected to be similar, but not as accurate, as what would be obtained using full resolution.

Since the WIC camera is most sensitive to precipitation of a few keV electrons [*Frey et al.*, 2003], it is interesting to investigate how much this energy range contributes to the total BC. From the electron and ion spectrometer data it is possible to calculate the BC within a chosen energy interval. This is shown in Figure 5.2 for five energy intervals constructed from the 47 energy channels. As mentioned in section 4.2.4, the energy channel of interest when comparing to the aurora in the WIC camera is the $1-3.5$ keV interval. Here we have also plotted on top the BC derived from the magnetic perturbations in blue. One can see a striking correspondence in shape of the two curves in the poleward part of the oval. It strongly suggests that the BC in this part of the oval (where WIC observe bright emissions in Figure 5.1B) is carried by keV electrons. The BCs are mainly carried by electrons as they are much more mobile. This is evident in Figure 5.2 as the pure electron line (red) does not significantly deviate from the black line including the ions. The higher energy panels never show any net upward current. The two lowest energy intervals indicate some intervals of larger fluxes up than down. We therefore believe that some of the deviations from the magnetometer derived BC and particle derived BC of upward BC (positive) could be due to low energy electrons below the detection threshold of FAST. During this pass, the spacecraft potential was mostly within $[-10,0]$ V.

This example illustrates that the WIC auroral brightness in the dusk sector during dark conditions could be used as a proxy for upward BCs, as was one of the assumptions when interpreting the results in Paper II. Since this is only one event, we acknowl-

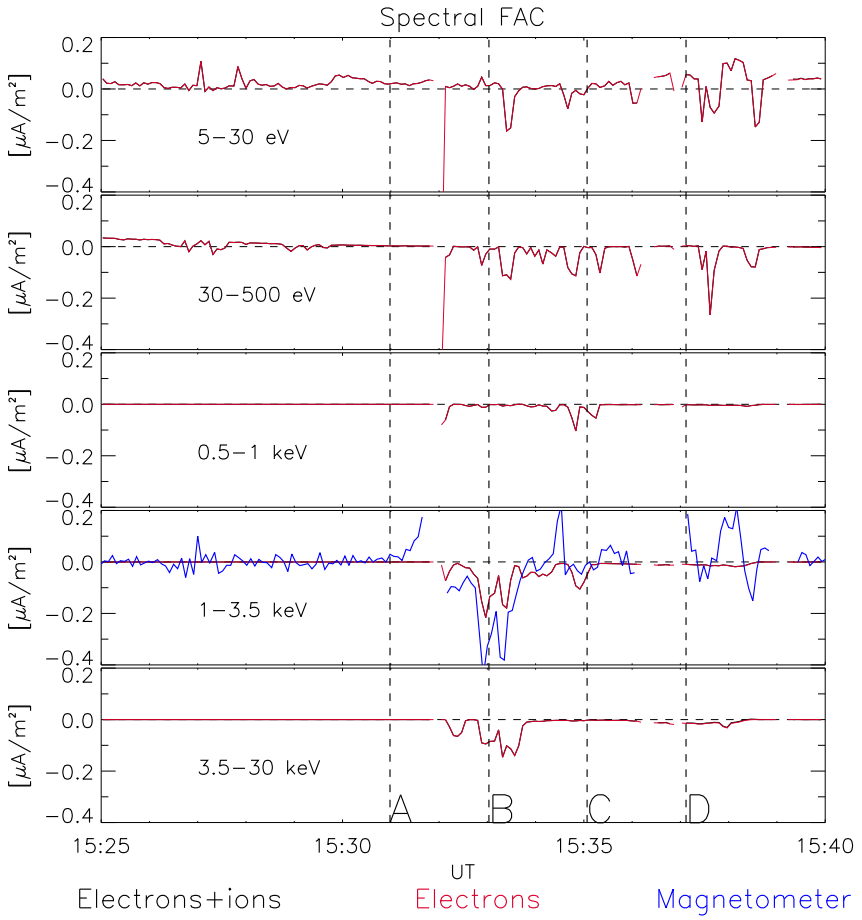

Figure 5.2: BC density derived from FAST electron and ion spectrometer data shown for 5 different energy intervals, increasing from top to bottom. Black lines include contribution from ions, red is only from electrons, and the blue line shown in the 1-3.5 keV panel is the BC density derived from the magnetic perturbations, same as Figure 5.1G.

edge that the correspondence between this type of aurora and upward BC can be more complicated at other instances. Therefore, our results showing asymmetric aurora in this sector during dominating IMF B_x conditions is not a definite proof of asymmetric BC. However, our observations of an opposite trend in the southern hemisphere gives further confidence that our interpretation in terms of asymmetric BC is likely.

5.2.2 The effect of dipole tilt

When introducing the process of restoring symmetry in Chapter 3, only IMF B_y was considered to establish the situation with an induced B_y on closed field-lines and corresponding asymmetric footpoints. In Paper IV we pointed out that also the dipole tilt is likely contributing in a similar manner to induce B_y on closed field-lines in the tail from the warping of the current sheet. This subsection elaborates in more detail how we believe this can be explained. We also discuss whether the effect from warping can contribute to the process of restoring symmetry.

In section 3.2 we explained the induced B_y on the nightside closed field-lines as a result of different convection in the two lobes due to IMF B_y. A similar situation can arise during periods of significant dipole tilt. For non-zero dipole tilt, the current sheet experiences warping [*Petrukovich*, 2011; *Tsyganenko*, 2002]. The warped current sheet is illustrated in the top and bottom part of Figure 5.3 for both signs of the dipole tilt as the grey region. This figure is adopted from Figure 3b in *Liou and Newell* [2010]. As suggested by *Liou and Newell* [2010], the warping is expected to lead to asymmetric convection patterns first in the two lobes (blue arrows), which in turn results in a velocity shear on the closed field-lines (blue arrows inside grey region) leading to an induced B_y. The induced B_y will be in opposite directions in the dawn and dusk flanks due to the symmetric warping, illustrated by the black arrows inside the grey region in Figure 5.3. As for the case with IMF B_y, this will affect the footpoints of the field-line, illustrated in the right part of each panel using the same polar projection as in Figure 3.6. To investigate the footpoint asymmetry, the nightside convection throat is of special interest, being the region in the nightside ionosphere on closed field-lines where there is a transition from duskward to dawnward convection toward the dayside. This region is important as it must be a conjugate feature since a field-line cannot be connected to different convection cells in the two hemispheres. It is known that the nightside convection throat is on average shifted toward a pre-midnight location in both hemispheres [*Haaland et al.*, 2007; *Pettigrew et al.*, 2010; *Ruohoniemi and Greenwald*, 1995], independent of IMF B_y and dipole tilt. It is therefore likely to assume that field-lines in the nightside convection throat region will experience an induced B_y related to the warping determined by the pre-midnight location of its apex. This pre-midnight location is

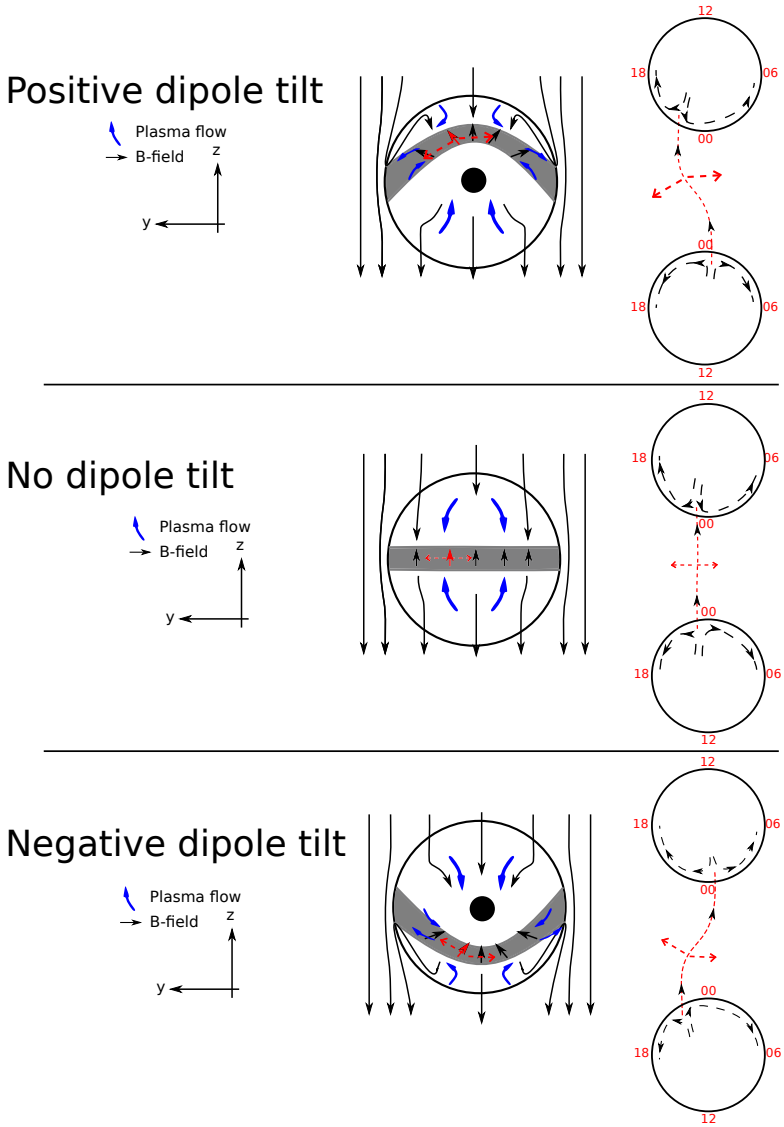

Figure 5.3: How warping of the current sheet due to dipole tilt can lead to an induced B_y on closed field-lines and associated asymmetric footpoints in the ionosphere during positive (top panel) and negative (bottom panel) values of the dipole tilt angle. In each panel, a cross-section of the tail is shown in the left panel (adopted from Figure 3b in *Liou and Newell* [2010]). The warped current sheet is indicated in grey. This warping lead to asymmetric convection patterns first in the two lobes (blue arrows), which in turn results in a velocity shear on the closed field-lines (blue arrows inside grey region) leading to an induced B_y. The induced B_y will be in opposite direction in the dawn and dusk flanks due to the symmetric warping (black arrows inside grey region). The apex of a closed field-line from the ionospheric nightside convection throat region is indicated with the dashed red arrows pointing away from a pre-midnight location. Right part of each panel indicate the geometry of a field-line from the ionospheric convection throat region having the resulting induced B_y and asymmetric footpoints. For comparison, the middle panel show the symmetric situation for no dipole tilt.

illustrated by the dashed red arrows in Figure 5.3. The right part of each panel shows how this field-line connects to the two hemispheres, now having asymmetric footpoints due to its induced B_y from the warping effect at the pre-midight location.

The two processes (IMF B_y and warping induced B_y) are likely present at the same time and their resulting contribution can add or subtract depending on the combination of the two effects. *Ruohoniemi and Greenwald* [1995] found that the combination of positive dipole tilt and positive IMF B_y, as well as negative dipole tilt and negative IMF B_y, on average produced the most extreme early and late, respectively, locations of the nightside convection throat region in the northern hemisphere. *Liou and Newell* [2010] found that this was also the case for the hemispheric longitudinal difference of substorm onset location. This is consistent with our explanation above when considering a pre-midnight field-line. This favourable combination was also the case in the event study in Paper IV, where a longitudinal displacement of 3 h in the nightside was seen during positive IMF B_y and dipole tilt. In Paper IV we use average BC maps from the Iridium constellation of low Earth orbiting satellites, known as AMPERE (Active Magnetosphere and Planetary Electrodynamics response Experiment) [*Anderson et al.*, 2000] and estimate the nightside convection throat region from identifying where the average R1/R2 current system reverse on the nighside during similar conditions as in the event. In Paper IV we only show three selected combinations of IMF B_y and dipole tilt, but Figure 5.4 shows all polarity combinations. The MLT location at which the average R1/R2 current system reverses in the nightside is indicated with a dashed line in each panel. From comparing this location for the different combinations of IMF B_y and dipole tilt, it is evident that both a positive dipole tilt and a positive IMF B_y contribute to an earlier location of the nightside convection throat in the northern hemisphere, and a later location in the southern hemisphere, and opposite when IMF B_y and dipole tilt is negative. Further details regarding how the AMPERE data was processed can be found in Paper IV.

Understanding the contributions to footpoint asymmetry in different regions are of great value when analysing the mapping between hemispheres from simultaneous observations of the global aurora. In many cases, the auroral display can be very different in the two hemispheres making it difficult to understand the mapping. Improved knowledge of what affects the mapping between the conjugate hemispheres can possibly help us interpret how the conjugate hemispheres are connected also during more disturbed conditions.

Whether the warping related B_y and its associated asymmetric footpoints in the nightside could lead to asymmetric stress release and hence asymmetric convection and BC (process of restoring symmetry) as discussed for IMF B_y is not fully understood. Looking at the middle row in Figure 5.4, representing the situation where the

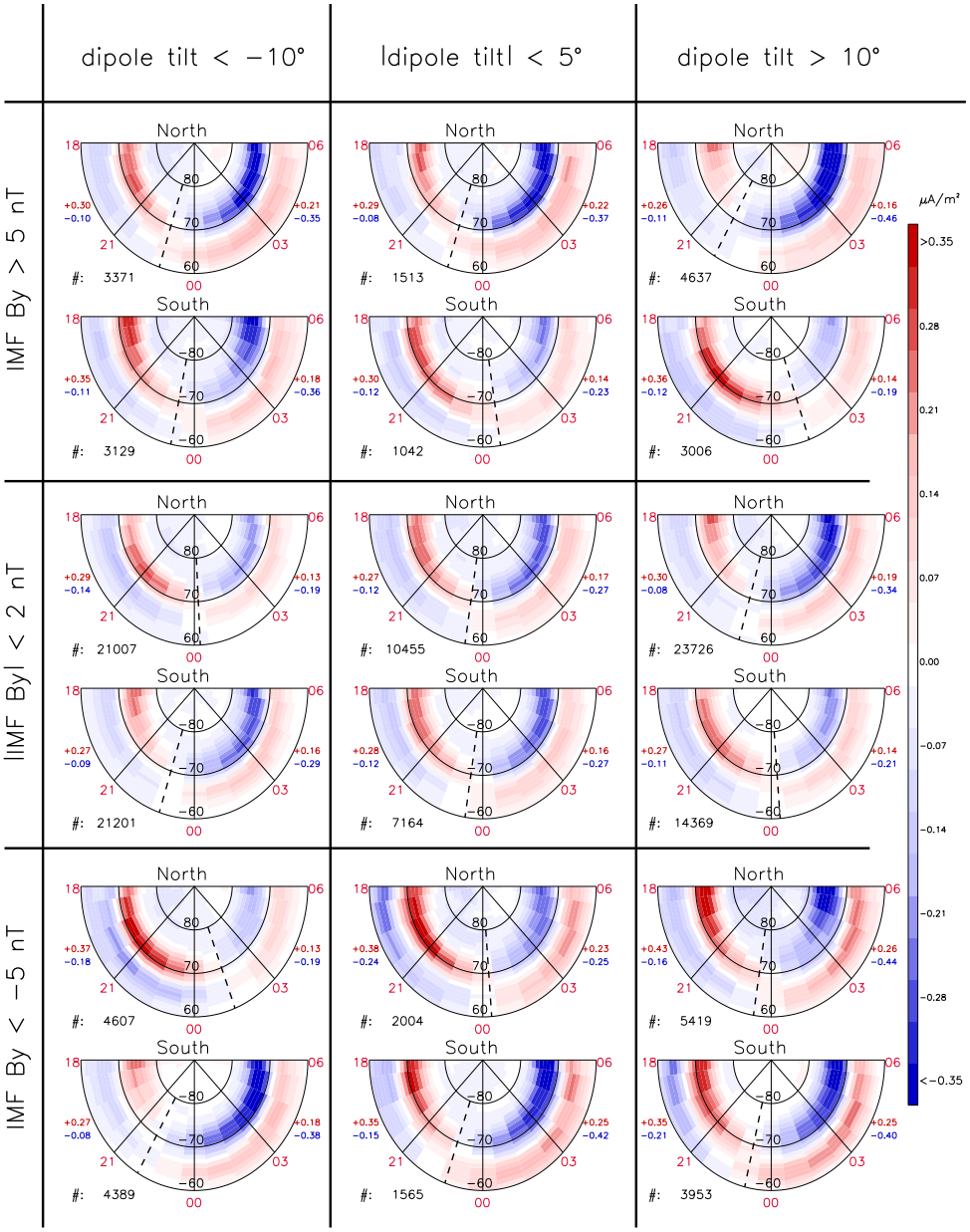

Figure 5.4: Average BC densities in the nightside from AMPERE shown on a MLAT/MLT grid. Both the northern and southern hemispheres are shown for all polarity combinations of IMF B_y and dipole tilt, as indicated by the top row and left column. The meridian likely representing the nightside convection throat region is shown as a dashed line. Maximum and minimum current densities for the dawn and dusk sector, separately, are printed to the right and left, respectively. Also, the total number of individual BC maps entering the analysis is indicated.

average IMF B_y is close to zero, the variations in BCs with dipole tilt are showing opposite dawn-dusk variations in BC densities in the two hemispheres. Although such signatures might be expected related to the process of restoring symmetry, these variations are likely affected also by the different levels of solar exposure. Hence, this trend can also be related to ionospheric conductivity differences. Further investigations are needed to determine the dipole tilt contribution to the process of restoring symmetry. A systematic investigation of the convection in the two hemispheres will likely provide further answers.

Chapter 6

Conclusions

This thesis is an investigation of two specific mechanisms that has been suggested to produce auroral asymmetries between the conjugate hemispheres. Below we summarize our main conclusions of this work:

→ Non-conjugate features are common in active auroral displays

→ IMF B_x influences the duskside auroral intensity during southward IMF oppositely in the two hemispheres

→ The opposite auroral response to IMF B_x in the conjugate hemipsheres is consistent with a more efficient SW dynamo on average in one hemisphere compared to the other

→ Field-lines with asymmetric footpoints (induced by IMF B_y) will release magnetic stress mainly into one hemisphere as they convect toward and around the Earth from the nightside. We name this the *process of restoring symmetry*

→ Signatures consistent with the process of restoring symmetry are observed in both ionospheric convection data and in average maps of BCs, suggesting that this mechanism can be responsible for substantial asymmetric forcing of the two hemispheres

Chapter 7

Future prospects

In this chapter we mention some of the open questions that remains to be answered regarding the two mechanisms investigated in this thesis.

7.1 Asymmetric SW dynamo

If the average auroral intensity asymmetries found in Paper II are related to the asymmetric SW dynamo as we suggest in this thesis, we expect a similar influence on the average BC strength in the same region. Our group at BCSS have looked at this from single events in the AMPERE data (not published), but not found conclusive results. Our understanding of how the asymmetric SW dynamo works may not be complete. The conceptual picture shown in Figure 3.1 might be oversimplified, as processes in the magnetosheath are ignored. Hence, further investigations are needed to better understand this process that could lead to asymmetric energy transfer from the SW into the magnetosphere in the two hemispheres.

7.2 Restoring symmetry process

The SuperDARN and AMPERE observations presented in Paper IV can only give information about the mapping in the nightside convection throat region. In order to further investigate the predictions of the process of restoring symmetry and its influence from the combined effect of IMF B_y and dipole tilt, simultaneous global conjugate imaging is needed as it, at least in principle, can highlight conjugate regions in multiple locations at the same time.

In Paper III and Paper IV we only considered the case when IMF is southward. To which degree one get induced B_y during northward IMF and how it affects the restoring symmetry process is also an open question that should be addressed in the future.

The restoring symmetry process is expected to affect the convection on closed field-lines in a similar way as the BCs. Hence, statistical maps of ionospheric convection on closed field-lines sorted by IMF B_y and dipole tilt is expected to show the same behaviour as for the BCs. This remains to be investigated by a specific study. If such a dependence is found also in the average convection, it would further highlight the importance of asymmetric forcing to understand the global magnetosphere-ionosphere coupling.

Abbreviations

ΔMLT	ΔMLT = MLT_{south} - MLT_{north}, longitudinal difference of conjugate points from its quiet-day location, p. 45
AACGM	Altitude Adjusted Corrected Geomagnetic coordinates [*Baker and Wing*, 1989], p. 13
AMPERE	Active Magnetosphere and Planetary Electrodynamics response Experiment [*Anderson et al.*, 2000], p. 52
BC	Birkeland Current, also known as field-aligned current (FAC), p. 18
BCSS	Birkeland Centre for Space Science, p. vii
DZA	Satellite Zenith Angle, p. 32
ECPC	Expanding/Contracting Polar Cap, p. 8
EUV	Extreme Ultraviolet, p. 12
FAST	Fast Auroral SnapshoT Explorer [*Pfaff Jr*, 2001], p. 46
FOV	Field-Of-View, p. 29
FUV	Far Ultraviolet, p. 29
IGRF	International Geomagnetic Reference Field, p. 13
IMAGE	Imager for Magnetopause-to-Aurora Global Exploration: Satellite used for global UV imaging [*Burch*, 2000], p. 18
IMF	Interplanetary Magnetic Field, p. 1
LBH	Lyman-Birge-Hopfield, p. 29
LFM	Lyon-Fedder-Mobarry [*Lyon et al.*, 2004], p. 45
MHD	Magnetohydrodynamic, p. 17

MLAT	Magnetic latitude, p. 13
MLT	Magnetic Local Time, p. 30
OCB	Open/Closed Boundary, p. 18
R_E	Earth radii, 6371 km, p. 10
R1/R2	Region 1/ region 2 currents [*Iijima and Potemra*, 1978], p. 26
SI12	Spectrographic Imager, 121.8 nm, doppler shifted Lyman$-\alpha$, p. 29
SI13	Spectrographic Imager, measures the atomic Oxygen line a 135.6 nm, p. 29
SuperDARN	Super Dual Auroral Radar Network [*Chisham et al.*, 2007; *Greenwald et al.*, 1995], p. 45
SW	Solar Wind, p. 1
SZA	Solar Zenith Angle, p. 32
TDI	Time Delay Integration, p. 30
UVI	Ultraviolet Imager, p. 33
VIS	Visible Imaging System, p. 33
WIC	Wideband Imaging Camera, p. 29

Bibliography

Acuña, M. H., K. W. Ogilvie, D. N. Baker, S. A. Curtis, D. H. Fairfield, and W. H. Mish, The global geospace science program and its investigations, *Space Science Reviews*, *71*, 5–21, 1995. 18, 33

Anderson, B. J., K. Takahashi, and B. A. Toth, Sensing global Birkeland currents with Iridium engeneering magnetometer data, *Geophysical Research Letters*, *27*, 4045–4048, 2000. 52, 59

Aubry, M. P., C. T. Russell, and M. G. Kivelson, Inward motion of the magnetopause before a substorm, *Journal of Geophysical Research: Space Physics*, *75*(34), 7018–7031, doi:10.1029/JA075i034p07018, 1970. 8

Axford, W. I., and C. O. Hines, A unifying theory of high-latitude geophysical phenomena and geomagnetic storms, *Canadian Journal of Physics*, *39*(10), 1433–1464, 1961. 10

Baker, J. B., A. J. Ridley, V. O. Papitashvili, and C. R. Clauer, The dependence of winter aurora on interplanetary parameters, *Journal of Geophysical Research*, *108*(A4), 8009, 2003. 18

Baker, K. B., and S. Wing, A new magnetic coordinate system for conjugate studies at high latitudes, *Journal of Geophysical Research*, *94*(A7), 9139, doi:10.1029/JA094iA07p09139, 1989. 13, 59

Belon, A. E., J. E. Maggs, T. N. Davis, K. B. Mather, N. W. Glass, and G. F. Hughes, Conjugacy of visual auroras during magnetically quiet periods, *Journal of Geophysical Research*, *74*(1), 1–28, doi:10.1029/JA074i001p00001, 1969. 20

Burch, J. L., Image mission overview, *Space Science Reviews*, *91*, 1–14, 2000. 18, 29, 59

Burch, J. L., et al., IMF By -dependent plasma flow and Birkeland currents in the dayside magnetosphere: 1. Dynamics Explorer observations, *Journal of Geophysical Research*, *90*(A2), 1577, doi:10.1029/JA090iA02p01577, 1985. 10, 27

Chaston, C. C., C. W. Carlson, R. E. Ergun, and J. P. McFadden, Alfvén Waves, Density Cavities and Electron Acceleration Observed from the FAST Spacecraft, *Physica Scripta*, *T84*, 64–68, 2000. 46

Chisham, G., et al., A decade of the Super Dual Auroral Radar Network (SuperDARN): Scientific achievements, new techniques and future directions, *Surveys in Geophysics*, *28*, 33–109, doi:10.1007/s10712-007-9017-8, 2007. 60

Chisham, G., et al., Remote sensing of the spatial and temporal structure of magnetopause and magnetotail reconnection from the ionosphere, *Reviews of Geophysics*, *46*(2007), 1–27, doi:10.1029/2007RG000223, 2008. 10

Chua, D., G. Parks, M. Brittnacher, W. Peria, G. Germany, J. Spann, and C. Carlson, Energy comparison of auroral electron precipitation: A comparison of substorms and pressure pulse related auroral activity, *Journal of Geophysical Research*, *106*(A4), 5945–5956, doi:10.1029/2000JA003027, 2001. 39

Clausen, L. B. N., J. B. H. Baker, J. M. Ruohoniemi, S. E. Milan, and B. J. Anderson, Dynamics of the region 1 Birkeland current oval derived from the active magnetosphere and planetary electrodynamics response experiment (AMPERE), *Journal of Geophysical Research*, *117*(6), 1–11, doi:10.1029/2012JA017666, 2012. 10

Cnossen, I., A. D. Richmond, M. Wiltberger, W. Wang, and P. Schmitt, The response of the coupled magnetosphere-ionosphere-thermosphere system to a 25% reduction in the dipole moment of the Earth's magnetic field, *Journal of Geophysical Research*, *116*(12), 1–13, doi:10.1029/2011JA017063, 2011. 13

Cowley, S., Magnetospheric asymmetries associated with the y-component of the IMF, *Planetary and Space Science*, *29*, 79–96, doi:10.1016/0032-0633(81)90141-0, 1981a. 22

Cowley, S. W. H., Asymmetry effects associated with the x-component of the IMF in a magnetically open magnetosphere, *Planetary and Space Science*, *29*(8), 809–818, 1981b. 15, 16, 17, 44

Cowley, S. W. H., Dungey's Reconnection Model of the Earth's Magnetosphere: The First 40 Years, in *Magnetospheric Plasma Physics: The Impact of Jim Dungey's Research*, vol. 41, edited by S. Cowley FRS, Stanley W. H. and Southwood, David and Mitton, chap. 1, pp. 1–32, Springer International Publishing, doi:10.1007/978-3-319-18359-6, 2015. 8

Cowley, S. W. H., and M. Lockwood, Excitation and decay of solar wind-driven flows in the magnetosphere-ionophere system, *Annales geophysicae*, *10*(1-2), 103–115, 1992. 8, 9

Crooker, N. U., Dayside merging and cusp geometry, *Journal of Geophysical Research*, *84*(A3), 951–959, doi:10.1029/JA084iA03p00951, 1979. 7

Crooker, N. U., and F. J. Rich, Lobe Cell Convection as a Summer Phenomenon, *Journal of Geophysical Research*, *98*(A8), 13,403–13,407, doi:10.1029/93JA01037, 1993. 10, 27

Drob, D. P., R. R. Meier, J. M. Picone, D. J. Strickland, R. J. Cox, and a. C. Nicholas, Atomic oxygen in the thermosphere during the July 13, 1982, solar proton event deduced from far ultraviolet images, *Journal of Geophysical Research*, *104*(A3), 4267–4278, doi:10.1029/1998ja900064, 1999. 36

Dubyagin, S. V., V. A. Sergeev, C. W. Carlson, S. R. Marple, T. I. Pulkkinen, and A. G. Yahnin, Evidence of near-Earth breakup location, *Geophysical Research Letters*, *30*(6), 1282, doi:10.1029/2002GL016569, 2003. 18, 41

Dungey, J. W., Interplanetary magnetic field and the auroral zones*, *Physical Review Letters*, *6*, 6–7, 1961. 5, 8

Elphinstone, R. D., K. Jankowska, J. S. Murphree, and L. L. Cogger, The Configuration of the Auroral Distribution for Interplanetary Magnetic Field B z Northward, 1. IMF Bx and B Dependencies as Observed by the Viking Satellite, *Journal of Geophysical Research*, *95*(A5), 5791–5804, doi:10.1029/JA095iA05p05791, 1990. 18

Frank, L. a., and K. L. Ackerson, Observations of charged particle precipitation into the auroral zone, *Journal of Geophysical Research*, *76*(16), 3612–3643, doi:10.1029/JA076i016p03612, 1971. 46

Frank, L. A., and J. B. Sigwarth, Simultaneous images of the northern and southern auroras from the Polar spacecraft: An auroral substorm, *Journal of Geophysical Research*, *108*(A4), 1–18, doi:10.1029/2002JA009356, 2003. 32, 33, 36, 37, 38

Frank, L. A., J. B. Sigwarth, J. D. Craven, J. P. Cravens, J. S. Dolan, M. R. Dvorsky, P. K. Hardebeck, J. D. Harvey, and D. W. Muller, The visible imaging system (VIS) for the Polar Spacecraft, *Space Science Reviews*, *71*, 297–328, 1995. 33, 36

Freeman, M. P., and D. J. Southwood, The effect of magnetospheric erosion on mid- and high-latitude ionospheric flows, *Planetary and Space Science*, *36*(5), 509–522, doi:10.1016/0032-0633(88)90110-9, 1988. 8

Frey, H. U., et al., Summary of quantitative interpretation of IMAGE far ultraviolet auroral data, *Space Science Reviews*, *109*(1-4), 255–283, doi:10.1023/B:SPAC.0000007521.39348.a5, 2003. 33, 34, 35, 36, 37, 38, 41, 48

Friis-Christensen, E., and J. Wilhjelm, Polar Cap Currents for Different Directions of the Interplanetary Magnetic Field in the Y-Z Plane, *Journal of Geophysical Research*, *80*(10), 1248–1260, doi:10.1029/JA080i010p01248, 1975. 21, 27

Friis-Christensen, E., K. Lassen, J. Wilhjelm, J. M. Wilcox, W. Gonzalez, and D. S. Colburn, Critical component of the interplanetary magnetic field responsible for large geomagnetic effects in the polar cap, *Journal of Geophysical Research*, *77*(19), 3371–3376, doi:10.1029/JA077i019p03371, 1972. 21

Ganushkina, N. Y., et al., Defining and resolving current systems in geospace, *Annales Geophysicae*, *33*, 1369–1402, doi:10.5194/angeo-33-1369-2015, 2015. 18

Gérard, J., B. Hubert, M. Meurant, V. I. Shematovich, D. V. Bisikalo, H. Frey, S. Mende, G. R. Gladstone, and C. W. Carlson, Observation of the proton aurora with IMAGE FUV imager and simultaneous ion flux in situ measurements, *Journal of Geophysical Research*, *106*(A12), 28,939–28,948, doi:10.1029/2001JA900119, 2001. 34

Gérard, J.-C., B. Hubert, D. V. Bisikalo, and V. I. Shematovich, A model of the Lyman-α line profile in the proton aurora, *Journal of Geophysical Research*, *105*(A7), 15,795, doi:10.1029/1999JA002002, 2000. 34

Germany, G. A., G. K. Parks, M. Brittnacher, J. Cumnock, D. Lummerzheim, J. F. Spann, L. Chen, P. G. Richards, and F. J. Rich, Remote determination of auroral energy characteristics during substorm activity, *Geophysical Research Letters*, *24*(8), 995–998, 1997. 38

Gonzalez, W. D., and F. S. Mozer, A quantitative model for the potential resulting from reconnection with an arbitrary interplanetary magnetic field, *Journal of Geophysical Research*, *79*(28), 4186–4194, doi:10.1029/JA079i028p04186, 1974. 7

Green, D. L., C. L. Waters, B. J. Anderson, and H. Korth, Seasonal and interplanetary magnetic field dependence of the field-aligned currents for both Northern and Southern Hemispheres, *Annales Geophysicae*, *27*, 1701–1715, 2009. 12, 27

Greenwald, R. a., et al., DARN/SuperDARN, *Space Science Reviews*, *71*, 761–796, doi:10.1007/BF00751350, 1995. 60

Griffiths, D. J., and R. College, *Introduction to Electrodynamics*, 531 pp., Pearson Education, 2008. 10

Grocott, A., S. V. Badman, S. W. H. Cowley, T. K. Yeoman, and P. J. Cripps, The influence of IMF By on the nature of the nightside high-latitude ionospheric flow during intervals of positive IMF Bz, *Annales Geophysicae*, pp. 1755–1764, doi:10.5194/angeo-22-1755-2004, 2004. 27

Grocott, A., T. K. Yeoman, S. E. Milan, and S. Cowley, Interhemispheric observations of the ionospheric signature of tail reconnection during IMF-northward non-substorm intervals, *Annales Geophysicae*, *23*, 1763–1770, doi:10.5194/angeo-23-1763-2005, 2005. 27

Grocott, A., S. E. Milan, and T. K. Yeoman, Interplanetary magnetic field control of fast azimuthal flows in the nightside high-latitude ionosphere, *Geophysical Research Letters*, *35*(8), L08,102, doi:10.1029/2008GL033545, 2008. 27

Grocott, A., et al., Multi-scale observations of magnetotail flux transport during IMF-northward non-substorm intervals, *Annales Geophysicae*, *25*(2002), 1709–1720, 2007. 27

Guo, X. C., C. Wang, Y. Q. Hu, and J. R. Kan, Bow shock contributions to region 1 field-aligned current: A new result from global MHD simulations, *Geophysical Research Letters*, *35*(3), 4–7, doi:10.1029/2007GL032713, 2008. 16, 17

Haaland, S. E., G. Paschmann, M. Förster, J. M. Quinn, R. B. Torbert, C. E. McIlwain, H. Vaith, P. A. Puhl-Quinn, and C. A. Kletzing, High-latitude plasma convection from Cluster EDI measurements : method and IMF-dependence, *Annales Geophysicae*, pp. 239–253, 2007. 21, 50

Hardy, D. a., M. S. Gussenhoven, and E. Holeman, A statistical model of auroral electron precipitation, *Journal of Geophysical Research*, *90*(A5), 4229, doi:10.1029/JA090iA05p04229, 1985. 39

He, M., J. Vogt, H. Lühr, E. Sorbalo, A. Blagau, G. Le, and G. Lu, A high-resolution model of field-aligned currents through empirical orthogonal functions analysis (MFACE), *Geophysical Research Letters*, *39*, 1–6, doi:10.1029/2012GL053168, 2012. 27

Heppner, J. P., and N. C. Maynard, Empirical high-latitude electric field models, *Journal of Geophysical Research*, *92*, 4467–4489, doi:10.1029/JA092iA05p04467, 1987. 21

Hubert, B., J.-C. Gérard, D. V. Bisikalo, V. I. Shematovich, and S. Solomon, The role of proton precipitation in the excitation of auroral FUV emissions, *Journal of Geophysical Research*, *106*(A10), 2001. 34, 35

Hubert, B., J. C. Gérard, D. S. Evans, M. Meurant, S. B. Mende, H. U. Frey, and T. J. Immel, Total electron and proton energy input during auroral substorms: Remote sensing with IMAGE-FUV, *Journal of Geophysical Research*, *107*(A8), 1–12, doi: 10.1029/2001JA009229, 2002. 34, 35

Hughes, W. J., The magnetopause, magnetotail, and magnetic reconnection, in *Introduction to Space Physics*, chap. 9, pp. 227–287, Cambridge University Press, New York, 1995. 6

Hunten, D., F. Roach, and J. Chamberlain, A photometric unit for the airglow and aurora, *Journal of Atmospheric and Terrestrial Physics*, *8*(6), 345–346, doi:10.1016/0021-9169(56)90111-8, 1956. 32

Iijima, T., and T. A. Potemra, Large-Scale Characteristics of Field-Aligned Currents Associated with Substorms, *Journal of Geophysical Research*, *83*(A2), 599–615, doi: 10.1029/JA083iA02p00599, 1978. 18, 26, 46, 60

Ishimoto, M., C. Meng, G. J. Romick, and R. E. Huffman, Auroral electron energy and flux from molecular nitrogen ultraviolet emissions observed by the S3-4 satellite, *Journal of Geophysical Research*, *93*(A9), 9854–9866, 1988. 38

Khurana, K. K., R. J. Walker, and T. Ogino, Magnetospheric convection in the presence of interplanetary magnetic field By: A conceptual model and simulations, *Journal of Geophysical Research*, *101*(A3), 4907–4916, 1996. 24, 26

Koskinen, H. E. J., and E. I. Tanskanen, Magnetospheric energy budget and the epsilon parameter, *Journal of Geophysical Research: Space Physics*, *107*(A11), 1–10, doi: 10.1029/2002JA009283, 2002. 15

Laundal, K. M., Auroral Imaging as a Tracer of Global Magnetospheric Dynamics, Ph.D. thesis, University of Bergen, 2010. 34

Laundal, K. M., and N. Østgaard, Asymmetric auroral intensities in the Earth's Northern and Southern hemispheres, *Nature*, *460*(7254), 491–493, doi:10.1038/nature08154, 2009. 17, 18, 33, 44

Liou, K., and P. T. Newell, On the azimuthal location of auroral breakup: Hemispheric asymmetry, *Geophysical Research Letters*, *37*(23), doi:10.1029/2010GL045537, 2010. 21, 23, 24, 26, 50, 51, 52

Liou, K., P. T. Newell, C. I. Meng, M. Brittnacher, and G. Parks, Characteristics of the solar wind controlled auroral emissions, *Journal of Geophysical Research*, *103*, 17,543–17,557, 1998. 18, 20, 21, 27

Liou, K., P. T. Newell, D. G. Sibeck, and C.-I. Meng, Observation of IMF and seasonal effects in the location of auroral substorm onset, *Journal of Geophysical Research*, *106*(A4), 5799–5810, 2001. 40

Lui, A. T. Y., Characteristics of the cross-tail current in the Earth's magnetotail, in *Magnetospheric Currents, Geophysical Monograph Series*, vol. 1, edited by T. A. Poterma, pp. 158–170, American Geophysical Union, Washington, D. C., 1984. 20

Lukianova, R. Y., a. Kozlovskii, and F. Christiansen, Field-aligned currents in the winter and summer hemispheres caused by IMF By, *Geomagnetism and Aeronomy*, *52*(3), 300–308, doi:10.1134/S0016793212020089, 2012. 27

Lyon, J. G., J. a. Fedder, and C. M. Mobarry, The Lyon-Fedder-Mobarry (LFM) global MHD magnetospheric simulation code, *Journal of Atmospheric and Solar-Terrestrial Physics*, *66*(15-16 SPEC. ISS.), 1333–1350, doi:10.1016/j.jastp.2004.03.020, 2004. 45, 59

Lysak, R. L., Feedback instability of the ionospheric resonant cavity, *Journal of Geophysical Research*, *96*(A2), 1553–1568, doi:10.1029/90JA02154, 1991. 12

Meier, R. R., Ultraviolet spectroscopy and remote sensing of the upper atmosphere, *Space Science Reviews*, *58*, 1–185, 1991. 32, 35, 36, 37, 38

Mende, S. B., C. W. Carlson, H. U. Frey, T. J. Immel, and J.-C. Gerard, IMAGE FUV and in situ FAST particle observations of substorm aurorae, *Journal of Geophysical Research*, *108*(A4), 8010, doi:10.1029/2002JA009413, 2003a. 18, 41

Mende, S. B., C. W. Carlson, H. U. Frey, L. M. Peticolas, and N. Østgaard, FAST and IMAGE-FUV observations of a substorm onset, *Journal of Geophysical Research*, *108*(A9), 1344, doi:10.1029/2002JA009787, 2003b. 18, 41

Mende, S. B., et al., Far ultraviolet imaging from the IMAGE spacecraft. 1. System design, *Space Science Reviews*, *91*, 243–270, 2000a. 29, 30

Mende, S. B., et al., Far ultraviolet imaging from the IMAGE spacecraft. 2. Wideband FUV imaging, *Space Science Reviews*, *91*, 271–285, 2000b. 29

Mende, S. B., et al., Far ultraviolet imaging from the IMAGE spacecraft. 3. Spectral imaging of Lyman alpha and OI 135.6 nm, *Space Science Reviews*, *91*, 287–318, 2000c. 29

Milan, S. E., Sun et Lumière: Solar Wind-Magnetosphere Coupling as Deduced from Ionospheric Flows and Polar Auroras, in *Magnetospheric Plasma Physics: The Impact of Jim Dungey's Research*, vol. 41, edited by S. Cowley FRS, Stanley W. H. and Southwood, David and Mitton, chap. 2, pp. 33–64, Springer International Publishing, doi:10.1007/978-3-319-18359-6, 2015. 7, 27

Milan, S. E., G. Provan, and B. Hubert, Magnetic flux transport in the Dungey cycle: A survey of dayside and nightside reconnection rates, *Journal of Geophysical Research: Space Physics*, *112*(1), 1–13, doi:10.1029/2006JA011642, 2007. 10

Milan, S. E., J. Hutchinson, P. D. Boakes, and B. Hubert, Influences on the radius of the auroral oval, *Annales Geophysicae*, *27*(7), 2913–2924, doi:10.5194/angeo-27-2913-2009, 2009. 10

Newell, P. T., K. M. Lyons, and C.-I. Meng, A large survey of electron acceleration events, *Journal of Geophysical Research*, *101*(A2), 2599, doi:10.1029/95JA03147, 1996. 46

Newell, P. T., T. Sotirelis, and S. Wing, Diffuse, monoenergetic, and broadband aurora: The global precipitation budget, *Journal of Geophysical Research*, *114*(A9), A09,207, doi:10.1029/2009JA014326, 2009. 41

Newell, P. T., T. Sotirelis, and S. Wing, Seasonal variations in diffuse, monoenergetic, and broadband aurora, *Journal of Geophysical Research*, *115*(A3), 1–19, doi:10.1029/2009JA014805, 2010. 12, 39, 41

Nishida, A., T. Mukai, T. Yamamoto, S. Kokubun, and K. Maezawa, A unified model of the magnetotail convection in geomagnetically quiet and active times, *Journal of Geophysical Research*, *103*(97), 4409, doi:10.1029/97JA01617, 1998. 27

Ohtani, S., S. Wing, G. Ueno, and T. Higuchi, Dependence of premidnight field-aligned currents and particle precipitation on solar illumination, *Journal of Geophysical Research*, *114*(A12), A12,205, doi:10.1029/2009JA014115, 2009. 12, 41

Østgaard, N., and K. M. Laundal, Auroral asymmetries in the conjugate hemispheres and interhemispheric currents, in *Auroral Phenomenology and Magnetospheric Processes: Earth and Other Planets, Geophysical Monograph Series*, vol. 197, edited by A. Keiling, E. Donovan, F. Bagenal, and T. Karlsson, pp. 99–111, American Geophysical Union, Washington, D. C., doi:10.1029/2011GM001190, 2012. 15, 17

Østgaard, N., S. B. Mende, H. U. Frey, and T. J. Immel, Interplanetary magnetic field control of the location of substorm onset and auroral features in the conjugate hemi-

spheres, *Journal of Geophysical Research*, *109*(A7), doi:10.1029/2003JA010370, 2004. 21, 27, 40

Østgaard, N., N. A. Tsyganenko, S. B. Mende, H. U. Frey, T. J. Immel, M. Fillingim, L. A. Frank, and J. B. Sigwarth, Observations and model predictions of substorm auroral asymmetries in the conjugate hemispheres, *Geophysical Research Letters*, *32*(5), 2–5, doi:10.1029/2004GL022166, 2005. 21, 27

Østgaard, N., B. K. Humberset, and K. M. Laundal, Evolution of auroral asymmetries in the conjugate hemispheres during two substorms, *Geophysical Research Letters*, *38*(3), 1–6, doi:10.1029/2010GL046057, 2011a. 20, 21, 40

Østgaard, N., K. M. Laundal, L. Juusola, A. Åsnes, S. E. Håland, and J. M. Weygand, Interhemispherical asymmetry of substorm onset locations and the interplanetary magnetic field, *Geophysical Research Letters*, *38*(8), 1–5, doi:10.1029/2011GL046767, 2011b. 21, 27, 40

Parker, E. N., Dynamics of the Interplanetary Gas and Magnetic Fields, *The Astrophysical Journal*, *128*, 664, doi:10.1086/146579, 1958. 44

Paschmann, G., S. Haaland, and R. Treumann, *Auroral Plasma Physics*, 100–120 pp., ISSI, Bern, 2002. 18, 41

Peng, Z., C. Wang, and Y. Q. Hu, Role of IMF B x in the solar wind-magnetosphere-ionosphere coupling, *Journal of Geophysical Research*, *115*(A8), A08,224, doi:10.1029/2010JA015454, 2010. 44

Petrukovich, A. A., Origins of plasma sheet By, *Journal of Geophysical Research*, *116*(A7), A07,217, doi:10.1029/2010JA016386, 2011. 50

Pettigrew, E. D., S. G. Shepherd, and J. M. Ruohoniemi, Climatological patterns of high-latitude convection in the Northern and Southern hemispheres: Dipole tilt dependencies and interhemispheric comparisons, *Journal of Geophysical Research: Space Physics*, *115*(7), 1–15, doi:10.1029/2009JA014956, 2010. 21, 50

Pfaff Jr, R., *The FAST Mision*, Springer Science+business Media Dordrecht, doi:10.1007/978-94-010-0332-2, 2001. 46, 59

Pitkänen, T., M. Hamrin, P. Norqvist, T. Karlsson, H. Nilsson, a. Kullen, S. M. Imber, and S. E. Milan, Azimuthal velocity shear within an Earthward fast flow – further evidence for magnetotail untwisting?, *Annales Geophysicae*, *33*, 245–255, doi:10.5194/angeo-33-245-2015, 2015. 27

Reiff, P. H., and J. L. Burch, IMF By-dependent plasma flow and Birkeland currents in the dayside magnetosphere. 2. A global model for northward and southward IMF, *Journal of Geophysical Research*, *90*, 1595–1609, doi:10.1029/JA090iA02p01595, 1985. 10, 27

Reistad, J. P., N. Østgaard, K. M. Laundal, and K. Oksavik, On the non-conjugacy of nightside aurora and their generator mechanisms, *Journal of Geophysical Research: Space Physics*, *118*(6), 3394–3406, doi:10.1002/jgra.50300, 2013. vii

Reistad, J. P., N. Østgaard, K. M. Laundal, S. Haaland, P. Tenfjord, K. Snekvik, K. Oksavik, and S. E. Milan, Intensity asymmetries in the dusk sector of the poleward auroral oval due to IMF Bx, *Journal of Geophysical Research: Space Physics*, *119*, 1–11, doi:10.1002/2014JA020216, 2014. vii

Reistad, J. P., et al., Dynamic effects of restoring footpoint symmetry on closed magnetic field-lines, *Journal of Geophysical Research: Space Physics*, *121*, doi: 10.1002/2015JA022058, 2016. viii

Richmond, A. D., Ionospheric Electrodynamics Using Magnetic Apex Coordinates, *Jornal of Geomagnetism and Geoelectricity*, *47*, 191–212, 1995. 13, 30, 33

Ruohoniemi, J. M., and R. A. Greenwald, Observations of IMF and seasonal effects in high-latitude convection, *Geophysical Research Letters*, *22*(9), 1121–1124, 1995. 50, 52

Shue, J.-H., P. T. Newell, K. Liou, and C.-I. Meng, Influence of interplanetary magnetic field on global auroral patterns, *Journal of Geophysical Research*, *106*(A4), 5913–5926, 2001. 20, 21, 27

Shue, J.-H., P. T. Newell, K. Liou, C. Meng, and S. W. H. Cowley, Interplanetary magnetic field Bx asymmetry effect on auroral brightness, *Journal of Geophysical Research*, *107*(A8), 1–10, 2002. 18, 44

Siscoe, G. L., and T. S. Huang, Polar Cap Inflation and Deflation, *Journal of Geophysical Research*, *90*(A1), 543–547, doi:10.1029/JA090iA01p00543, 1985. 8

Siscoe, G. L., W. Lotko, and B. U. O. Sonnerup, A high-latitude, low-latitude boundary layer model of the convection current system, *Journal of Geophysical Research*, *96*(90), 3487–3495, 1991. 16, 18

Siscoe, G. L., N. U. Crooker, G. M. Erickson, B. U. O. Sonnerup, K. D. Siebert, D. R. Weimer, W. W. White, and N. C. Maynard, Global Geometry of Magnetospheric

Currents Inferred from MHD Simulations, in *Magnetospheric Current Systems, Geophysical Monograph Series, vol. 118*, edited by S. Othani, R. Fujii, M. Hesse, and R. L. Lysak, pp. 41–52, AGU, Washington, D. C., 2000. 15, 16, 18

Solomon, S. C., Auroral particle transport using Monte Carlo and hybrid methods, doi: 10.1029/2000JA002011, 2001. 34

Solomon, S. C., P. B. Hays, and V. Abreu, The Auroral 6300 ÅEmission: Observations and Modeling, *Journal of Geophysical Research*, *93*(A9), 9867–9882, doi:10.1017/CBO9781107415324.004, 1988. 34

Sonnerup, B. U. O., and B. G. Ledley, Ogo 5 magnetopause structure and classical reconnection, *Journal of Geophysical Research*, *84*(A2), 399, doi:10.1029/JA084iA02p00399, 1979. 8

Stenbaek-Nielsen, H. C., and A. Otto, Conjugate auroras and the interplanetary magnetic field, *Journal of Geophysical Research*, *102*(A2), 2223–2232, 1997. 19, 20, 21, 24, 27

Stenbaek-Nielsen, H. C., T. N. Davis, and N. W. Glass, Relative Motions of Auroral Conjugate Points during Substorms, *Journal of Geophysical Research*, *77*(10), 1844–1858, 1972. 20, 40

Stenbaek-Nielsen, H. C., E. M. Wescott, T. N. Davis, and R. W. Peterson, Differences in auroral intensity at conjugate points, *Journal of Geophysical Research*, *78*(4), 659–671, doi:10.1029/JA078i004p00659, 1973. 20

Strickland, D. J., R. J. Cox, R. R. Meier, and D. P. Drob, Global O/N2 derived from DE 1 FUV dayglow data: Technique and examples from two storm periods, *Journal of Geophysical Research*, *104*(A3), 4251–4266, doi:10.1029/98JA02817, 1999. 36

Tanaka, T., Field-aligned-current systems in the numerically simulated magnetosphere, in *Magnetospheric Current Systems, Geophysical Monograph Series, vol. 118*, edited by S. Othani, R. Fujii, M. Hesse, and R. L. Lysak, pp. 53–59, AGU, Washington, D. C., 2000. 18

Tenfjord, P., and N. Østgaard, Energy transfer and flow in the solar wind-magnetosphere-ionosphere system: A new coupling function, *Journal of Geophysical Research: Space Physics*, *118*(9), 5659–5672, doi:10.1002/jgra.50545, 2013. 15

Tenfjord, P., N. Østgaard, K. Snekvik, K. M. Laundal, J. P. Reistad, S. Haaland, and S. E. Milan, How the IMF By induces a By component in the closed magnetosphere and how it leads to asymmetric currents and convection patterns in the two hemispheres, *Journal of Geophysical Research: Space Physics*, *120*, doi: 10.1002/2015JA021579, 2015. viii, 19

Torr, M. R., et al., A far ultraviolet imager for the International Solar-Terrestrial Physics Mission, *Space Science Reviews*, *71*(1-4), 329–383, doi:10.1007/BF00751335, 1995. 33

Tsyganenko, N. A., A model of the near magnetosphere with a dawn-dusk asymmetry 1. Mathematical structure, *Journal of Geophysical Research*, *107*(A8), 1–17, doi: 10.1029/2001JA000219, 2002. 50

VanZandt, T. E., W. L. Clark, and J. M. Warnock, Magnetic Apex Coordinates: A Magnetic Coordinate System for the Ionospheric F2 Layer, *Journal of Geophysical Research*, *77*(13), 1972. 13, 30

Wang, H., H. Lühr, S. Y. Ma, and H. U. Frey, Interhemispheric comparison of average substorm onset locations: evidence for deviation from conjugacy, *Annales Geophysicae*, *25*(2004), 989–999, doi:10.5194/angeo-25-989-2007, 2007. 21

Waters, C. L., B. J. Anderson, and K. Liou, Estimation of global field aligned currents using the iridium® System magnetometer data, *Geophysical Research Letters*, *28*(11), 2165–2168, doi:10.1029/2000GL012725, 2001. 18

Weimer, D. R., Models of high-latitude electric potentials derived with a least error fit of spherical harmonic coefficients, *Journal of Geophysical Research*, *100*(A10), 19,595, doi:10.1029/95JA01755, 1995. 21

Wing, S., P. T. Newell, D. G. Sibeck, and K. B. Baker, A Large Statistical Study of the Entry of Interplanetary Magnetic Field Y-Component Into the Magnetosphere, *Geophysical Research Letters*, *22*(16), 2083–2086, 1995. 20

Paper II

Intensity asymmetries in the dusk sector of the poleward auroral oval due to IMF B_x

J. P. Reistad, N. Østgaard, K. M. Laundal, S. Haaland, P. Tenfjord, K. Snekvik, K. Oksavik, and S. E. Milan

Journal of Geophysical Research, Vol. 119, doi:10.1002/2014JA020216 (2014)

II

AGU PUBLICATIONS

JGR

Journal of Geophysical Research: Space Physics

RESEARCH ARTICLE
10.1002/2014JA020216

Key Points:
- Auroral intensity affected differently by IMF Bx in the two hemispheres
- Observations are consistent with increased SW dynamo efficiency in one hemisphere
- Accumulative effect might be important in total energy budget

Correspondence to:
J. P. Reistad,
Jone.Reistad@ift.uib.no

Citation:
Reistad, J. P., N. Østgaard, K. M. Laundal, S. Haaland, P. Tenfjord, K. Snekvik, K. Oksavik, and S. E. Milan (2014), Intensity asymmetries in the dusk sector of the poleward auroral oval due to IMF B_x, *J. Geophys. Res. Space Physics*, *119*, doi:10.1002/2014JA020216.

Received 23 MAY 2014
Accepted 21 OCT 2014
Accepted article online 26 OCT 2014

Intensity asymmetries in the dusk sector of the poleward auroral oval due to IMF B_x

J. P. Reistad[1], N. Østgaard[1], K. M. Laundal[1,2], S. Haaland[1,3], P. Tenfjord[1], K. Snekvik[1], K. Oksavik[1,4], and S. E. Milan[1,5]

[1] Birkeland Centre for Space Science, Department of Physics and Technology, University of Bergen, Bergen, Norway, [2] Teknova AS, Kristiansand, Norway, [3] Max-Planck Institute for Solar System Research, Göttingen, Germany, [4] Department of Geophysics, University Centre in Svalbard, Longyearbyen, Norway, [5] Department of Physics and Astronomy, University of Leicester, Leicester, UK

Abstract In the exploration of global-scale features of the Earth's aurora, little attention has been given to the radial component of the Interplanetary Magnetic Field (IMF). This study investigates the global auroral response in both hemispheres when the IMF is southward and lies in the *xz* plane. We present a statistical study of the average auroral response in the 12–24 magnetic local time (MLT) sector to an *x* component in the IMF. Maps of auroral intensity in both hemispheres for two IMF B_x dominated conditions (± IMF B_x) are shown during periods of negative IMF B_z, small IMF B_y, and local winter. This is obtained by using global imaging from the Wideband Imaging Camera on the IMAGE satellite. The analysis indicates a significant asymmetry between the two IMF B_x dominated conditions in both hemispheres. In the Northern Hemisphere the aurora is brighter in the 15–19 MLT region during negative IMF B_x. In the Southern Hemisphere the aurora is brighter in the 16–20 MLT sector during positive IMF B_x. We interpret the results in the context of a more efficient solar wind dynamo in one hemisphere. Both the intensity asymmetry and its location are consistent with this idea. This has earlier been suggested from case studies of simultaneous observations of the aurora in both hemispheres, but hitherto never been observed to have a general impact on global auroral brightness in both hemispheres from a statistical study. The observed asymmetries between the two IMF B_x cases are not large; however, the difference is significant with a 95% confidence level. As the solar wind conditions examined in the study are rather common (37% of the time) the accumulative effect of this small influence may be important for the total energy budget.

1. Introduction

To study how the Earth is coupled to space, information of how the two hemispheres respond differently to external forcing is of great interest. Simultaneous imaging from both hemispheres has been used to identify and investigate possible mechanisms responsible for the observed asymmetries of the global aurora [e.g., *Stenbaek-Nielsen and Davis*, 1972; *Craven et al.*, 1991; *Stenbaek-Nielsen and Otto*, 1997; *Sato et al.*, 1998; *Østgaard et al.*, 2003; *Fillingim et al.*, 2005; *Laundal and Østgaard*, 2009; *Østgaard et al.*, 2011; *Reistad et al.*, 2013].

Global imaging of the auroral oval represents a unique opportunity to look at footprints of a large region of the magnetosphere simultaneously. Although this has been possible for a long time on a sporadic basis from the mid-1980s, little is known about how the *x* component of the interplanetary magnetic field (IMF) can affect the aurora, especially in relation to its response in both hemispheres. Statistical studies of global auroral UV brightness dependence on solar wind (SW) and IMF in the Northern Hemisphere indicate that negative IMF B_x on average produces brighter aurora than positive IMF B_x during negative IMF B_z conditions [*Liou et al.*, 1998; *Shue et al.*, 2002; *Baker et al.*, 2003].

Largely based on global auroral imaging, *Østgaard and Laundal* [2012] proposed that nonconjugate aurora, which is aurora only appearing in one end of the magnetic field line or is significantly brighter in one hemisphere, could be caused by three different generator mechanisms: the solar wind (SW) dynamo (related to the interplanetary magnetic field (IMF) B_x), effect of IMF B_y penetration, and ionospheric conductivity. The recent study by *Reistad et al.* [2013] indicated that those three mechanisms indeed seem to play an important role in controlling the occurrence and location of nonconjugate aurorae.

AGU Journal of Geophysical Research: Space Physics 10.1002/2014JA020216

In this paper we will go one step further and investigate if there is a significant auroral intensity difference in the two hemispheres in the dusk sector due to IMF B_x. As will be outlined in the paper, we apply certain selection criteria in order to avoid effects of other possible mechanisms that can produce asymmetric aurora. We focus on the dusk sector and especially the poleward part of the oval because this is the region where we expect the effects of IMF B_x to be observable in our data. In this region we have typically upward field-aligned currents (Region 1) and precipitating electrons. As suggested earlier [*Cowley*, 1981; *Laundal and Østgaard*, 2009; *Reistad et al.*, 2013], hemispheric intensity asymmetries in the aurora in this region could be a signature of asymmetric Region 1 currents in the two hemispheres. In the discussion section we will look at our results in the light of this related work.

2. Data and Method

2.1. Global Imaging Data

To investigate how IMF B_x affects the auroral intensity and distribution in both hemispheres, we have used the Far Ultraviolet Wideband Imaging Camera (WIC) [*Mende et al.*, 2000] on board the IMAGE (Imager for Magnetopause-to-Aurora Global Exploration) satellite [*Burch*, 2000]. IMAGE was launched in 2000 into an elliptic orbit with an apogee of 7 R_E precessing over Northern Hemisphere at a rate of about 50° per year. From early 2004, the apsidal precession of the orbit allowed imaging of the Southern Hemisphere with almost the same coverage as it initially had after launch in March 2000. Thus, the IMAGE WIC data set represents a unique opportunity to study the average global response of the aurora statistically in both hemispheres with the same instrument.

The WIC instrument is sensitive to the Lyman-Birge-Hopfield band and a few N lines of the aurora in the UV range (140–190 nm) [*Mende et al.*, 2000]. In general, both precipitating electrons and protons produce these emissions and their relative influence on the resulting brightness depends primarily on their energy fluxes [*Frey et al.*, 2003]. Usually, the precipitating proton energy flux is too small to influence the WIC signal, but in some cases it can account for a significant portion of the signal [*Frey et al.*, 2001; *Donovan et al.*, 2012]. However, in the poleward part of the dusk sector oval this should not be a problem as we focus on the upward Region 1 current with limited downward proton fluxes. In the discussion we will use the intensity counts as measured by the WIC camera as a proxy for upward field-aligned current. This will be further explained in section 4.

2.2. Image Selection

We have used 1 min IMF and SW data from NASA's Space Physics Data Facility, http://omniweb.gsfc.nasa.gov [e.g., *King and Papitashvili*, 2005] represented in the Geocentric Solar Magnetospheric coordinate system. These data represent the conditions at the nose of the Earth's bow shock. To account for the additional propagation time needed for the IMF to affect the magnetosphere, we further shift the IMF data to $x = -10\ R_E$ using the present SW velocity. This is consistent with what has been done in earlier event studies, e.g., *Reistad et al.* [2013] and also what is suggested by MHD models regarding Region 1 current generation at the magnetopause [*Siscoe et al.*, 2000].

The event selection criteria are crucial when investigating the IMF B_x effects. We want to exclude contributions from other possible mechanisms [*Østgaard and Laundal*, 2012] as far as statistical sample number allows for. We start by identifying intervals during the IMAGE mission where strict criteria on IMF and seasonal variations are met. Only global imaging data that fulfils the following criteria are used: (1) $|\text{IMF } B_x| > 2$ nT, (2) $|\text{IMF } B_y| < 2$ nT, (3) IMF $B_z < 0$ nT, (4) $10° < |\text{Dipole tilt}| < 30°$, (5) > 10 min between observations, and (6) criteria must be satisfied for more than 10 min. In the identified time intervals, a global image is chosen toward the end of the interval but not less than 5 min before the end of the interval. This is to ensure that we select images that have been exposed to the favorable IMF and tilt criteria as long as possible. Using these criteria we get two sets of images in each hemisphere which will be compared: One set for IMF $B_x < -2$ nT, and one set for IMF $B_x > 2$ nT.

We want to exclude, as good as possible, other mechanisms that can produce asymmetric aurora to avoid that the IMF B_x signatures drown in other stronger signals. The selection process is therefore crucial and makes this study different from other studies that have performed statistical analysis on a much wider spectrum of geomagnetic conditions [e.g., *Shue et al.*, 2001, 2002; *Baker et al.*, 2003].

The negative IMF B_z condition is chosen to include only the intervals where magnetic flux is opened on the dayside and convected across the polar cap. At the same time we want to include only times when there is a

AGU Journal of Geophysical Research: Space Physics 10.1002/2014JA020216

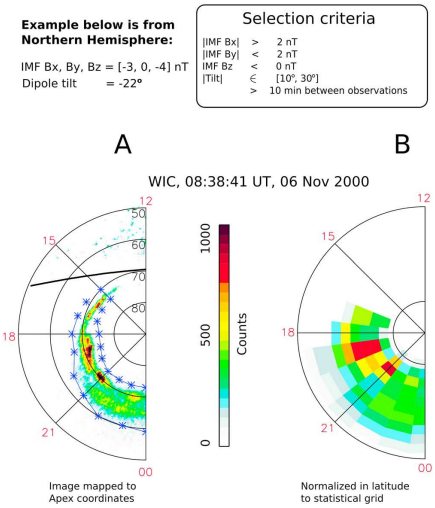

Figure 1. Selection criteria and overview of the method for image processing. (a) Example from the Northern Hemisphere after dayglow subtraction satisfying the selection criteria. Blue lines indicate the detected oval boundaries with asterisks located at the center of the 1 h MLT bin used in the statistics. (b) MLT sectors where all criteria are met get normalized to a common 10 bin latitudinal extent. The values seen in Figure 1b enter the statistical analysis.

significant x component and a small y component in the IMF to minimize signatures of IMF B_y effects. Due to seasonal effects and the offset of the geomagnetic pole from the rotational axis, the two polar ionospheres are exposed differently to solar radiation in magnetic coordinates. The difference is to the first order quantified by the dipole tilt angle. Due to a large contribution of dayglow-induced emissions in the WIC camera from regions in direct sunlight, we only use images from the local winter hemisphere. In the Northern Hemisphere we use images having dipole tilt angles from −30° to −10°, and in the Southern Hemisphere we use only images having dipole tilt angle from 10° to 30°. The use of local winter periods allows us to more accurately examine differences in a large region of the auroral oval extending to ∼ 15 MLT on the duskside in order to cover more of the Region 1 current region in the dusk sector. As mentioned in section 1, seasonal differences may lead to the occurrence of asymmetric aurora. However, these effects should not depend upon IMF B_x. When applying the same tilt criteria in both hemispheres such effects should not affect our results when having a sufficient number of samples.

The WIC images have a 2 min cadence, and consecutive images are therefore correlated. In the statistical analysis we require observations to be more than 10 min apart to be considered not correlated. This reduces the number of observations but gives a set of images where each event is weighted more equally.

2.3. Image Processing

Although we require the images to be taken during local winter as quantified by criterion (4) listed above, some regions of the auroral oval are still directly exposed to sunlight leaving dayglow-induced emissions in the WIC images. The dayglow-induced emissions, and a varying background, are therefore subtracted from each image separately. This is done by constructing a model of the dayglow emissions from pixels not influenced by aurora based on their solar zenith angle and satellite zenith angle in the mapped image. The modeled pixel intensity is then subtracted from all pixels leaving only auroral emissions in the image. This introduces an uncertainty in the regions exposed to sunlight, especially regions far into the dayside, typically the 12–14 MLT sector in our data set. Strict criteria in the dayglow removal technique and manual inspection of the performance for each image result in less data from these regions. For the chosen range of dipole tilt angles, the oval will on average be in darkness from 15 MLT and tailward on the duskside. Therefore, the analysis will focus on the 15–24 MLT region. An example of an image from the Northern Hemisphere satisfying the selection criteria after dayglow removal is shown in Figure 1a. The black line oriented in a dusk-dawn direction shows the location of the terminator. Since we investigate the possible IMF B_x influence on the duskside auroral intensity, we only show this sector as it corresponds to the upward Region 1 current and electron precipitation into the ionosphere.

As we want to study the intensity within the oval, the images are transformed into a frame following the oval. The advantage is that the statistics will be less affected by the location of the oval from event to event

AGU Journal of Geophysical Research: Space Physics 10.1002/2014JA020216

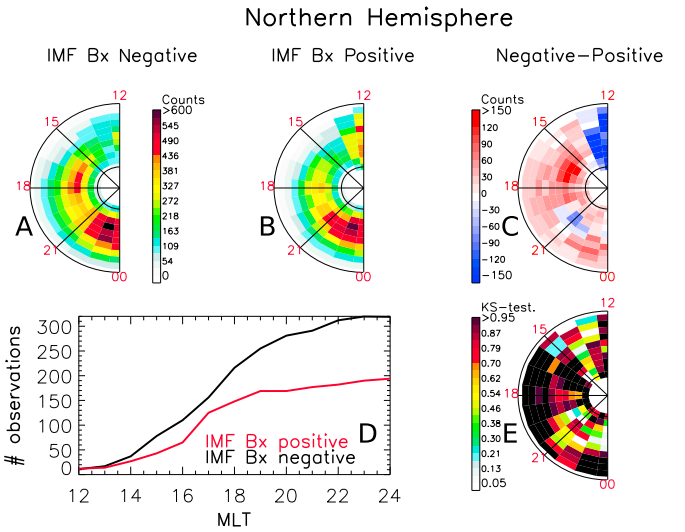

Figure 2. Results of the statistical analysis in the Northern Hemisphere. (a) Maps of median auroral intensity for the IMF B_x negative case. (b) Corresponding map for the positive IMF B_x case. (c) The intensity difference between the two IMF B_x cases. (d) Number of events across the domain. (e) The significance level of the test that the two distributions do not originate from the same distributions, using the Kolmogorov-Smirnov test. The expected increased brightness for negative IMF B_x can be seen from 16 to 19 MLT.

and minor errors in the satellite pointing direction. Previous statistical studies focusing on average auroral intensities or energies [e.g., *Shue et al.*, 2001, 2002; *Newell et al.*, 1996] superposed their data on a fixed MLT/MLAT grid. By using a normalized latitudinal width of the oval, signatures at the poleward/equatorward boundary and within the oval can be more easily identified. To do so, we determine the poleward and equatorward boundaries of the oval as shown in Figure 1a. The blue lines with asterisks indicate the oval boundary and the 1 h MLT resolution that we use in the statistical grid. The boundaries are determined by a threshold value depending on the mean and the spread of the counts in a 1 h by 1° MLT/MLAT grid. When the boundaries have been determined, the auroral signatures in MLT sectors with valid boundaries are normalized into a common latitudinal extent of 10 entries. To be considered as valid boundaries we require the poleward boundary to be between 62° and 81° latitude, and the equatorward boundary to be between 52° and 72°. In addition, we require that neighboring MLT sector boundaries within one image should not differ by more than 4° and that the total width of the oval should not exceed 15° MLAT. For the event shown in Figure 1a, all the criteria are satisfied and the corresponding aurora normalized in MLT sectors are rebinned in 10 latitudinal bins as shown in Figure 1b. As a result, each image can contribute with up to 13 MLT slices to the statistical analysis. When discussing the results, the number of events is referring to the number of such slices.

2.4. Statistical Analysis

When showing maps of auroral intensities for the two IMF B_x sets in each hemisphere, we use the median of the distribution. This will reduce the weighting of extreme events. A similar result is obtained when using the mean (not shown here). To test the hypothesis that the distribution of data for a given MLT value and latitudinal bin is different for the two different IMF B_x cases in the same hemisphere, we perform a Kolmogorov-Smirnov test [*Press et al.*, 1992]. Based on this test, we identify in which regions of the maps the hypothesis is found to be true (data are not drawn from the same distribution), given a significance level. To show how the significance level varies in the grid, we present maps of the significance level.

AGU Journal of Geophysical Research: Space Physics 10.1002/2014JA020216

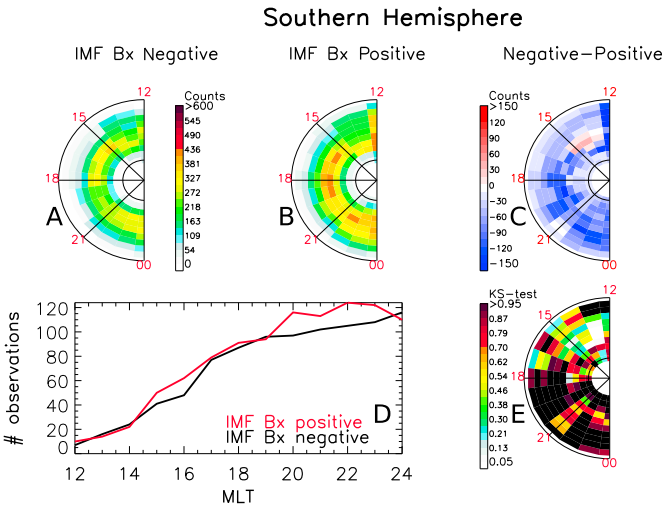

Figure 3. Results of the statistical analysis in the Southern Hemisphere. (a) Maps of median auroral intensity for the IMF B_x negative case. (b) Corresponding map for the positive IMF B_x case. (c) The intensity difference between the two IMF B_x cases. (d) Number of events across the domain. (e) The significance level of the test that the two distributions do not originate from the same distributions, using the Kolmogorov-Smirnov test. The expected increased brightness for positive IMF B_x can be seen from 16 to 20 MLT.

3. Results

Figures 2 and 3 show the results from the statistical analysis in the same format for the Northern and Southern Hemispheres, respectively. Figure 2a shows the dusk sector (12–24 MLT) median auroral intensity for the negative IMF B_x case. The corresponding plot for the positive IMF B_x case is shown in Figure 2b and their difference in Figure 2c. The map in Figure 2e shows the probability that the two distributions in every cell in Figures 2a and 2b are not drawn from the same distribution by using the Kolmogorov-Smirnov test. The color scale is chosen to show how the significance varies in regions outside the 95% (5%) confidence interval. In the black regions the hypothesis is true (there is an asymmetry), and in white regions it is falsified (there is not an asymmetry). Figure 2d shows how many events that were used in the statistics for the two cases in different MLT sectors. A line plot is here provided as there is an equal number of events in each latitudinal bin for a given MLT sector due to the oval boundary and normalization method used.

For the Northern Hemisphere results in Figure 2 the 15–19 MLT range for the IMF B_x negative case is more intense than the IMF B_x positive case. The signature is also in the poleward half of the normalized oval and is significant on a 95% confidence level in the 15–17 MLT sector. The contributions from substorm activity are clearly seen with a peak around 23 MLT, as expected. However, there are no significant asymmetries between the two IMF B_x cases in this region.

The results for the corresponding situation in the Southern Hemisphere during the same local winter conditions are seen in Figure 3 in the same format as for the Northern Hemisphere. Now the positive IMF B_x case in Figure 3b shows the most intense aurora in the 16–20 MLT sector. Taking the data spread and number of observations into account, the Kolmogorov-Smirnov test indicates that the 17–20 MLT sector is more than 95% likely to be drawn from different distributions, meaning that there is a significant IMF B_x influence in this region also in the Southern Hemisphere.

AGU Journal of Geophysical Research: Space Physics 10.1002/2014JA020216

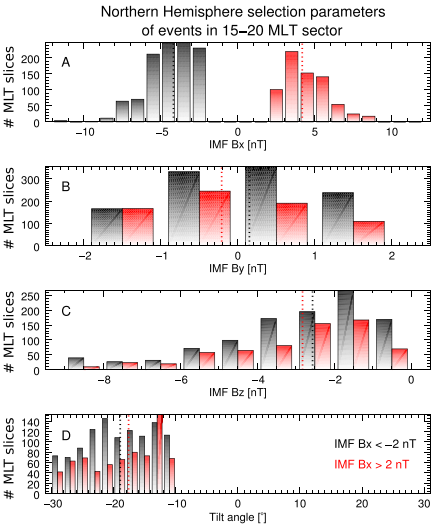

Figure 4. Distribution of IMF and dipole tilt angles for the events in the statistical study for the Northern Hemisphere. Black bars represent the negative IMF B_x case, and red bars the positive IMF B_x case. Number of MLT slices refers to the total number of events in the 15–20 MLT sector for the given parameter interval and IMF B_x case. Vertical dashed lines represent the median of the distribution. (a) IMF B_x distribution, (b) IMF B_y distribution, (c) IMF B_z distribution, and (d) dipole tilt angle distribution.

4. Discussion

As seen in Figures 2e and 3e, there is a region 15–17 MLT in Northern Hemisphere and 17–20 MLT in Southern Hemisphere, where the brightness for the two IMF B_x cases differs significantly. In the Northern Hemisphere the difference in the 15–19 MLT region is about 170 camera counts or ~0.3 kR in the WIC passband. In the Southern Hemisphere the difference is ~150 camera counts for the 16–20 MLT sector, well above the Poisson noise in the images with a standard deviation of typically 30 counts. Typical count rates can be seen in Figure 1a. This difference is a relatively small modification on the general auroral brightness, as also expected as $|\text{IMF } B_x| > 2$ nT is not a strong criterion. However, it is significant in our data set which is chosen to include the periods when IMF B_x asymmetries are believed to be most prominent. The selection criteria used to avoid IMF B_y influences on our result will also rule out periods of strong driving since such periods often have an $|\text{IMF } B_y| > 2$ nT. We also tried a different criteria, requiring IMF B_x to be twice the magnitude of IMF B_y and no limitation on their magnitude. The results were similar but slightly less significant indicating contamination from IMF B_y effects.

When comparing the two IMF $_BX$ cases it is important that both distributions on average represent the same geomagnetic conditions. In particular the IMF B_z is important when looking at the median auroral response as this will affect the overall driving of the system. In Figures 4 and 5 we present histograms for the IMF components and tilt angles concurrent with each latitudinal slice in the 15–20 MLT sector that enter into the statistics in Figures 2 and 3. The negative IMF B_x case is shown in black and positive IMF B_x in red. The median of the distributions is shown with vertical dashed lines in respective colors. In Figure 4c we see that the shape of the Northern Hemisphere distributions of IMF B_z is similar for both IMF B_x cases, and their median value differs by 0.3 nT. This is a small difference. We also notice that the IMF B_x/B_y antisymmetry is almost completely avoided due to the selection criteria. The median of the two distributions lies within ±0.2 nT as seen in Figure 4b. Hence, we conclude that the Northern Hemisphere data sets are not biased with respect to SW driving. The difference of the median dipole tilt angle is also low, about 1°. The main difference between the two cases is that there are fewer IMF B_x positive events.

In the Southern Hemisphere we see from Figures 5a and 5b that the IMF B_x/B_y antisymmetry only results in a small shift of around 0.4 nT from 0 of the median for IMF B_y. Looking at the IMF B_z distributions in Figure 5c, the difference of the median is now slightly larger for the two IMF B_x cases compared to the Northern Hemisphere (Figure 4c). The difference is here 0.5 nT in the direction of the observed asymmetry, making the Southern Hemisphere results slightly biased from this point of view. We have investigated this possible bias by looking at how the count rate depend upon IMF B_z. From every MLT slice in the 15–20 MLT sector, a scatterplot of the mean count versus IMF B_z was made. From this scatter, the median count value of points within 1 nT wide bins of IMF B_z gives a line that relates how strongly the different events respond. Such lines are shown for the Northern Hemisphere in Figure 6 for both IMF B_x cases (negative IMF B_x in black and

AGU Journal of Geophysical Research: Space Physics 10.1002/2014JA020216

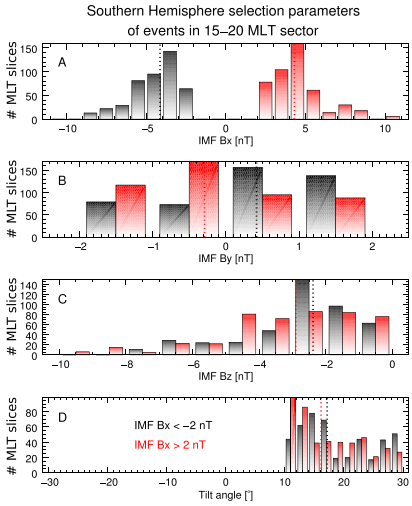

Figure 5. Distribution of IMF and dipole tilt angles for the events in the statistical study for the Southern Hemisphere. The figure is in the same format as Figure 4.

positive IMF B_x in red). We can see that the negative IMF B_x case has a stronger response for all IMF B_z, consistent with our results in Figure 2. The histogram from Figure 4c is also plotted in the same figure, and we can see how the 95% confidence level of the median [*Chen and Ratra*, 2011] increases with decreasing number of MLT slices. Looking at the corresponding plot for the Southern Hemisphere data, shown in Figure 7, one can see that the general IMF B_x difference we presented in Figure 3 is evident in the IMF $B_z \in [-4, 0]$ nT range. Looking at the IMF B_z histogram in the same plot we see that the majority of the events occur for IMF $B_z > -4$ nT. It is evident from Figure 7 that the few events having large negative IMF B_z do not affect the results in a way that will give larger intensities for the positive IMF B_x case. We hence conclude that the observed IMF B_x difference in the Southern Hemisphere cannot be explained by a bias in selection regarding IMF B_z.

As mentioned in section 2, the measured WIC signal primarily originates from precipitating electrons. In the ionosphere, the upward Region 1 current is associated with electron precipitation [e.g., *Paschmann et al.*, 2002; *Mende et al.*, 2003a, 2003b; *Dubyagin et al.*, 2003]. Hence, the dusk sector Region 1 current is of interest. However, WIC is only sensitive to the accelerated part of the electron spectra, typically 0.5–5 keV. Within this energy range the WIC counts are nearly proportional to the electron energy flux [*Frey et al.*, 2003]. In general, the current could be carried by lower energy electrons leaving little to no signatures in auroral UV brightness. Within this sector and outside the regions associated with magnetic reconnection the precipitation is characterized by so-called "inverted Vs" [*Newell et al.*, 1996; *Chaston et al.*, 2007]. The inverted-V type of precipitation is the most dominant in the local winter hemisphere dusk region [*Newell et al.*, 2009] and is believed to carry the majority of the upward field-aligned current. Another characteristic electron spectrum is the Alfvén wave accelerated spectrum, characterized by a broad energy distribution and associated bright aurora [*Chaston et al.*, 2003]. Such precipitation is found to occur typically in regions associated with magnetic reconnection [*Chaston et al.*, 2007] and substorm aurora [*Mende et al.*, 2003a; *Newell et al.*, 2009]; and hence, its signature is expected to have a fundamentally different origin. Using particle and field measurements from low-Earth orbiting satellites, [*Ohtani et al.*, 2009] have shown that the dusk sector Region 1 current density is proportional to the precipitating electron energy flux. They found the mean electron energy during these crossings in darkness to be typically between 1.5 and 2 keV which is the electron energy range the WIC instrument is most sensitive to. Hence, event observations of simultaneous global aurora [*Laundal and Østgaard*, 2009; *Reistad et al.*, 2013] showing increased ionospheric UV brightness in the 18–24 MLT region are consistent with the Region 1 current system having different intensity in the two hemispheres. Based on this we will interpret our statistical auroral response in the 15–20 MLT sector during local winter conditions as a proxy of the average Region 1 currents.

The question regarding where and how the Region 1 currents are generated at the magnetopause and coupled to the ionosphere has been investigated extensively [e.g., *Siscoe et al.*, 1991, 2000; *Song and Lysak*, 2001; *Guo et al.*, 2008; *Lopez et al.*, 2011]. MHD modeling studies such as *Siscoe et al.* [2000] and *Guo et al.* [2008] suggest that the Region 1 current at most local times tends to be driven across the magnetopause. From

AGU Journal of Geophysical Research: Space Physics 10.1002/2014JA020216

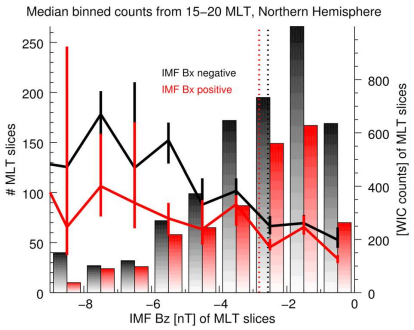

Figure 6. Line plots of WIC response for different IMF B_z values in the data set derived from median binned values of average counts for each event in the 15–20 MLT sector in the Northern Hemisphere. Histograms of IMF B_z are also shown for comparison. Black and red lines and bars represent the negative and positive IMF B_x cases, respectively. Axis to the left corresponds to the histogram, and axis to the lines corresponds to the lines.

these arguments we would expect to see a possible influence on the aurora where the Region 1 current is flowing out of the ionosphere, namely in a large portion of the 12–24 MLT sector. In Figures 2 and 3 we have chosen to include periods with substorms. These periods are associated with IMF B_z negative and therefore strong Region 1 currents. Leaving out substorm periods using the list of substorms also identified by the WIC camera [*Frey et al.*, 2004] and only use data more than 90 min after substorm onset, we get the same trends in our results but not the same significance levels. Although substorm intervals represent a contamination of our data we will argue that the Region 1 currents have a different origin and footprint than substorms. As long as we identify the difference within the 15–20 MLT sector, we can interpret our results to reflect the possible IMF B_x influences on the directly driven Region 1 currents.

In the following we will interpret our findings in the context of how the SW dynamo can have different efficiency in the two hemispheres due to an IMF B_x component. By asymmetric SW dynamo efficiency we mean that the energy transfer from the SW to the magnetosphere can be different in the two hemispheres.

As first suggested by *Cowley* [1981] and later supported by others [e.g., *Laundal and Østgaard*, 2009; *Østgaard and Laundal*, 2012; *Reistad et al.*, 2013], an *x* component of the IMF could, during negative IMF B_z conditions, lead to different magnetic tension forces acting on the open magnetic field lines being draped down tail, possibly affecting the energy transfer at the magnetopause differently in the two hemispheres. This effect is illustrated in Figures 8a and 8b for both negative and positive IMF B_x, respectively, during southward IMF B_z and small IMF B_y. Figures 8a and 8b are a remake of the original figure from *Cowley* [1981]. Here the magnitude of the magnetic tension force on open field lines is illustrated with wide black arrows where the field lines have a small curvature radius, and smaller black arrows in the opposite hemisphere experiencing a smaller tension force due to the greater radius of curvature. The SW electric field, due to the SW velocity and IMF, during the conditions illustrated in Figure 8, points out of the paper as indicated by the red arrows. In the high-latitude region tailward of the terminator the electric field and $\mathbf{j}_\perp$ point in opposite directions, hence the name SW dynamo. When neglecting particle pressure gradients in the magnetohydrodynamic (MHD) momentum equation for a quasi-neutral plasma, and rewriting the $\mathbf{j}\times\mathbf{B}$ force, we are left with one force term that depends on the curvature of the magnetic field—the magnetic tension force—and one related to the gradient in

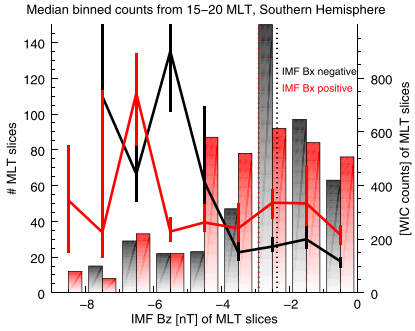

Figure 7. Line plots of WIC response for different IMF B_z values in the data set derived from median binned values of average counts for each event in the 15–50 MLT sector in the Southern Hemisphere. Histograms of IMF B_z are also shown for comparison. Black and red lines and bars represent the negative and positive IMF B_x cases, respectively. Axis to the left corresponds to the histogram, and axis to the right corresponds to the lines.

AGU Journal of Geophysical Research: Space Physics 10.1002/2014JA020216

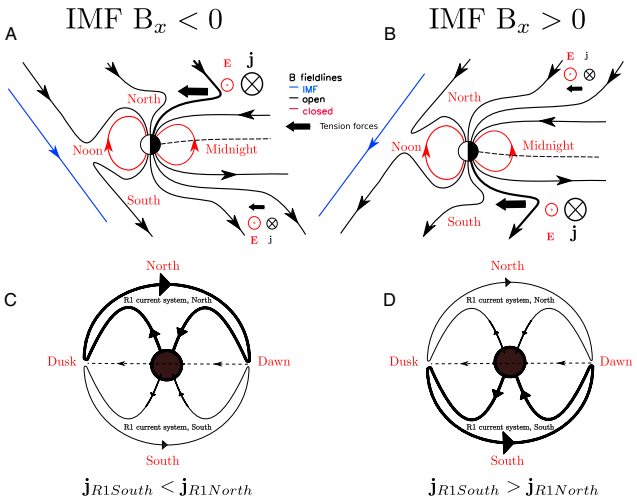

Figure 8. (a) The presence of a negative *x* component in the IMF during negative IMF B_z resulting in different magnetic tension forces (illustrated with large black arrows) on open field lines possibly affecting the energy transfer at the magnetopause different in the two hemispheres. Lines in blue, black, and red show the interplanetary, open, and closed field lines, respectively. At high latitudes, tailward of the terminator, the tension force will decelerate plasma and affect the magnetopause current density. This is indicated with the black arrow going into the figure in this region. This figure is adopted from *Cowley* [1981]. (b) Corresponding figure during positive IMF B_x. (c) Associated changes in current density for negative IMF B_x of the Region 1 current system that closes across the high-latitude magnetopause [*Siscoe et al.*, 1991; *Siscoe et al.*, 2000; *Guo et al.*, 2008]. Here the Earth is viewed from the tail. (d) Corresponding figure during positive IMF B_x.

magnetic pressure perpendicular to the magnetic field:

$$\rho_m \frac{\mathrm{d}\mathbf{v}}{\mathrm{d}t} = \mathbf{j} \times \mathbf{B} = \frac{B^2}{\mu_0 R_c}\hat{\mathbf{n}} - \nabla_\perp \left(\frac{B^2}{2\mu_0}\right), \tag{1}$$

where ρ_m is mass density, R_c is the radius of curvature of the magnetic field, $\hat{\mathbf{n}}$ is the unit normal pointing toward the center of curvature, and $\frac{\mathrm{d}\mathbf{v}}{\mathrm{d}t}$ is the total derivative of the plasma velocity. Using vector identities and Ampère's law, equation (1) takes the form

$$\mathbf{j}_\perp = \frac{\rho_m \mathbf{B} \times \frac{\mathrm{d}\mathbf{v}}{\mathrm{d}t}}{B^2}. \tag{2}$$

Applied to the SW-magnetosphere system, $\mathbf{j}_\perp$ represents the magnetopause current density normal to the magnetic field resulting from the combined effect of the two terms on the right side in equation (1). MHD modeling of magnetospheric current systems [e.g., *Siscoe et al.*, 2000; *Tanaka*, 2000; *Guo et al.*, 2008] indicates that the Region 1 currents enclosing the polar cap [*Iijima and Potemra*, 1978] indeed seem to be generated on the high-latitude magnetopause as perpendicular currents, as earlier suggested by e.g. *Siscoe et al.* [1991] in their Figure 1. This is conceptually indicated in Figures 8c and 8d where the Earth is viewed from the tail. Taking into account the possible change of magnetic tension force on the open field lines due to an IMF B_x component, this could alter the magnitude of the first term on the right side in equation (1) and hence affect **j**. For negative IMF B_x (Figure 8a) open field lines on the nightside are conceptually believed to experience a stronger magnetic tension force in the Northern Hemisphere. This can eventually increase **j** in the Northern Hemisphere relative to the Southern Hemisphere according to equation (1). For positive IMF B_x it will be the other way around as shown in Figure 8b by the black arrows going into the paper. For the

AGU Journal of Geophysical Research: Space Physics 10.1002/2014JA020216

suggested generation of Region 1 currents at the magnetopause [*Siscoe et al.*, 1991, 2000; *Tanaka*, 2000; *Guo et al.*, 2008], this asymmetric influence on **j** due to IMF B_x could affect the Region 1 currents differently in the two hemispheres. This is illustrated for both IMF B_x cases in Figures 8c and 8d by the different thickness of the lines in the two hemispheres.

The observations presented in Figure 2 are consistent with an enhanced SW dynamo in the Northern Hemisphere during IMF B_x negative as illustrated in Figures 8a and 8c. The signature is also in the poleward half of the normalized oval, consistent with the Region 1 current location. The observations presented from the Southern Hemisphere in Figure 3 are also in agreement with this idea, suggesting an enhanced SW dynamo in the Southern Hemisphere during positive IMF B_x. To the best of our knowledge, this is the first statistical observational study indicating that IMF B_x can modify the energy conversion between the SW and the magnetosphere differently in the two hemispheres in a general sense, and although the average effect is found to be small the accumulative effect may be important. The $|\text{IMF } B_x| > 2$ nT criterion is in fact met 73% of the time during IMF $B_z < 0$ conditions in the period 2000–2005.

The asymmetric SW dynamo has been suggested as a possible explanation for asymmetric aurora in earlier case studies [*Laundal and Østgaard*, 2009; *Reistad et al.*, 2013] but has not been mentioned in earlier statistical studies of aurora with regard to IMF B_x [*Liou et al.*, 1998; *Shue et al.*, 2002; *Baker et al.*, 2003]. However, the IMF B_x asymmetries found in the Northern Hemisphere in these previous statistical studies are consistent with our results, being generally stronger aurora in the Northern Hemisphere for negative IMF B_x. These results are therefore also consistent with what we would expect from increased SW dynamo action in the Northern Hemisphere during negative IMF B_x.

We emphasize that the observations and interpretation presented here are only indirect evidence of the influence of an asymmetric SW dynamo on auroral brightness. A more direct investigation during carefully selected intervals may give more insight into the importance of the IMF B_x on SW dynamo efficiency.

5. Conclusion

We have shown median auroral intensity maps from the dusk sector in both hemispheres during negative IMF B_z and dominating IMF B_x over B_y conditions. We have found that in the Northern Hemisphere the aurora is brighter in the 15–19 MLT sector during IMF B_x negative conditions. This asymmetry is most evident in the poleward half of the indicated oval. In the Southern Hemisphere we observe an opposite behavior where the aurora in the 16–20 MLT sector is brighter during IMF B_x positive conditions. In both hemispheres the two auroral distributions are significantly different with a 95% significance level within most of the indicated regions. Our results are consistent with an increased SW dynamo efficiency in the Northern Hemisphere for negative IMF B_x and in the Southern Hemisphere for positive IMF B_x. The possible modulation of SW dynamo efficiency between the hemispheres due to IMF B_x has only been suggested in earlier case studies. This is the first statistical study of observations from both hemispheres indicating that this mechanism is likely to produce general differences in auroral brightness. Although the asymmetries are weak in a general sense, the accumulative effect may be important in the total energy budget as $|\text{IMF } B_x| > 2$ nT is a common condition in the SW.

Acknowledgments
We thank S.B. Mende and the IMAGE FUV team for the use of IMAGE FUV data. We acknowledge the use of NASA/GSFC's Space Physics Data Facility for OMNI data. This study was supported by the Research Council of Norway under contract 223252/F50 and 212014/F50.

Yuming Wang thanks Jianpeng Guo and another reviewer for their assistance in evaluating this paper.

References

Baker, J. B., A. J. Ridley, V. O. Papitashvili, and C. R. Clauer (2003), The dependence of winter aurora on interplanetary parameters, *J. Geophys. Res.*, *108*(A4), 8009, doi:10.1029/2002JA009352.

Burch, J. L. (2000), Image mission overview, *Space Sci. Rev.*, *91*, 1–14.

Chaston, C. C., L. M. Peticolas, J. W. Bonnell, C. W. Carlson, R. E. Ergun, J. P. McFadden, and R. J. Strangeway (2003), Width and brightness of auroral arcs driven by inertial Alfvén waves, *J. Geophys. Res.*, *108*(A2), 1091, doi:10.1029/2001JA007537.

Chaston, C. C., C. W. Carlson, J. P. McFadden, R. E. Ergun, and R. J. Strangeway (2007), How important are dispersive Alfvén waves for auroral particle acceleration?, *Geophys. Res. Lett.*, *34*, L07101, doi:10.1029/2006GL029144.

Chen, G., and B. Ratra (2011), Median statistics and the hubble constant, *Astron. Soc. Pac.*, *123*(907), 1127–1132.

Cowley, S. W. H. (1981), Asymmetry effects associated with the x-component of the IMF in a magnetically open magnetosphere, *Planet. Space Sci.*, *29*(8), 809–818.

Craven, J. D., J. S. Murphree, L. A. Frank, and L. L. Cogger (1991), Simultaneous optical observations of transpolar arcs in the two polar caps, *Geophys. Res. Lett.*, *18*(12), 2297–2300.

Donovan, E., E. Spanswick, J. Liang, J. Grant, B. Jackel, and M. Greffen (2012), Magnetospheric dynamics and the proton aurora, in *Auroral Phenomenology and Magnetospheric Processes: Earth and Other Planets, Geophys. Monogr. Ser.*, vol. 197, edited by A. Keiling et al., pp. 99–111, AGU, Washington, D. C., doi:10.1029/2011GM001190.

Dubyagin, S. V., V. A. Sergeev, C. W. Carlson, S. R. Marple, T. I. Pulkkinen, and A. G. Yahnin (2003), Evidence of near-Earth breakup location, *Geophys. Res. Lett.*, *30*(6), 1282, doi:10.1029/2002GL016569.

AGU Journal of Geophysical Research: Space Physics 10.1002/2014JA020216

Fillingim, M. O., G. K. Parks, H. U. Frey, T. J. Immel, and S. B. Mende (2005), Hemispheric asymmetry of the afternoon electron aurora, *Geophys. Res. Lett., 32*, L03113, doi:10.1029/2004GL021635.

Frey, H. U., S. B. Mende, C. W. Carlson, J.-C. Gèrard, B. Hubert, J. Spann, R. Gladstone, and T. J. Immel (2001), The electron and proton aurora as seen by IMAGE-FUV and FAST, *Geophys. Res. Lett., 28*(6), 1135–1138.

Frey, H. U., S. B. Mende, T. J. Immel, J.-C. Gèrard, B. Hubert, S. Habraken, J. Spann, G. R. Gladstone, D. V. Bisikalo, and V. I. Shematovich (2003), Summary of quantitative interpretation of IMAGE far ultraviolet auroral data, *Space Sci. Rev., 109*, 255–283.

Frey, H. U., S. B. Mende, V. Angelopoulos, and E. F. Donovan (2004), Substorm onset observations by IMAGE-FUV, *J. Geophys. Res., 109*, A10304, doi:10.1029/2004JA010607.

Guo, X. C., C. Wang, Y. Q. Hu, and J. R. Kan (2008), Bow shock contributions to region 1 field-aligned current: A new result from global MHD simulations, *Geophys. Res. Lett., 35*, L03108, doi:10.1029/2007GL032713.

Iijima, T., and T. A. Potemra (1978), Large-scale characteristics of field-aligned currents associated with substorms, *J. Geophys. Res., 83*(A2), 599–615, doi:10.1029/JA083iA02p00599.

King, J. H., and N. E. Papitashvili (2005), Solar wind spatial scales in and comparisons of hourly Wind and ACE plasma and magnetic field data, *J. Geophys. Res., 110*, A02104, doi:10.1029/2004JA010649.

Laundal, K. M., and N. Østgaard (2009), Asymmetric auroral intensities in the Earth's Northern and Southern Hemispheres, *Nature, 460*(7254), 491–493, doi:10.1038/nature08154.

Liou, K., P. T. Newell, C. I. Meng, M. Brittnacher, and G. Parks (1998), Characteristics of the solar wind controlled auroral emissions, *J. Geophys. Res., 103*(A8), 17,543–17,557.

Lopez, R. E., V. G. Merkin, and J. G. Lyon (2011), The role of the bow shock in solar wind-magnetosphere coupling, *Ann. Geophys., 29*, 1129–1135, doi:10.5194/angeo-29-1129-2011.

Mende, S. B., et al. (2000), Far ultraviolet imaging from the IMAGE spacecraft. 2. Wideband FUV imaging, *Space Sci. Rev., 91*, 271–285.

Mende, S. B., C. W. Carlson, H. U. Frey, T. J. Immel, and J.-C. Gèrard (2003a), IMAGE FUV and in situ FAST particle observations of substorm aurorae, *J. Geophys. Res., 108*(A4), 8010, doi:10.1029/2002JA009413.

Mende, S. B., C. W. Carlson, H. U. Frey, L. M. Peticolas, and N. Østgaard (2003b), FAST and IMAGE-FUV observations of a substorm onset, *J. Geophys. Res., 108*(A9), 1344, doi:10.1029/2002JA009787.

Newell, P. T., C.-I. Meng, and K. M. Lyons (1996), Suppression of discrete aurorae by sunlight, *Nature, 381*, 766–767, doi:10.1038/381766a0.

Newell, P. T., T. Sotirelis, and S. Wing (2009), Diffuse, monoenergetic, and broadband aurora: The global precipitation budget, *J. Geophys. Res., 114*, A09207, doi:10.1029/2009JA014326.

Østgaard, N., and K. M. Laundal (2012), Auroral asymmetries in the conjugate hemispheres and interhemispheric currents, in *Auroral Phenomenology and Magnetospheric Processes: Earth and Other Planets, Geophys. Monogr. Ser.*, vol. 197, edited by A. Keiling et al., pp. 99–111, AGU, Washington, D. C., doi:10.1029/2011GM001190.

Østgaard, N., S. B. Mende, H. U. Frey, L. A. Frank, and J. B. Sigwarth (2003), Observations of non-conjugate theta aurora, *Geophys. Res. Lett., 30*(21), 2125, doi:10.1029/2003GL017914.

Østgaard, N., K. M. Laundal, L. Juusola, A. Åsnes, S. E. Haaland, and J. M. Weygand (2011), Interhemispherical asymmetry of substorm onset locations and the interplanetary magnetic field, *Geophys. Res. Lett., 38*, L08104, doi:10.1029/2011GL046767.

Ohtani, S., S. Wing, G. Ueno, and T. Higuchi (2009), Dependence of premidnight field-aligned currents and particle precipitation on solar illumination, *J. Geophys. Res., 114*, A12205, doi:10.1029/2009JA014115.

Paschmann, G., S. Haaland, and R. Treumann (2002), *Auroral Plasma Physics*, 100–120 pp., ISSI, Bern.

Press, W. H., S. A. Teukolsky, W. T. Vetterling, and B. P. Flannery (1992), *Numerical Recipes in Fortran 77: The Art of Scientific Computing*, 2nd ed., pp. 614–622, Cambridge Univ. Press, Cambridge, U. K.

Reistad, J. P., N. Østgaard, K. M. Laundal, and K. Oksavik (2013), On the non-conjugacy of nightside aurora and their generator mechanisms, *J. Geophys. Res. Space Physics*, *118*, 3394–3406, doi:10.1002/jgra.50300.

Sato, N., T. Nagaoka, K. Hashimoto, and T. Saemundsson (1998), Conjugacy of isolated auroral arcs and nonconjugate auroral breakups, *J. Geophys. Res., 103*(A6), 11,641–11,652, doi:10.1029/98JA00461.

Shue, J.-H., P. T. Newell, K. Liou, and C.-I. Meng (2001), Influence of interplanetary magnetic field on global auroral patterns, *J. Geophys. Res., 106*(A4), 5913–926.

Shue, J.-H., P. T. Newell, K. Liou, C. Meng, and S. W. H. Cowley (2002), Interplanetary magnetic field Bx asymmetry effect on auroral brightness, *J. Geophys. Res., 107*(A8), SIA 16-1–SIA 16-1, doi:10.1029/2001JA000229.

Siscoe, G. L., W. Lotko, and B. U. Ö. Sonnerup (1991), A high-latitude, low-latitude boundary layer model of the convection current system, *J. Geophys. Res., 96*(A3), 3487–3495.

Siscoe, G. L., N. U. Crooker, G. M. Erickson, B. U. O. Sonnerup, K. Siebert, D. R. Weimer, W. W. White, and N. C. Maynard (2000), Global geometry of magnetospheric currents inferred from MHD simulations, in *Magnetospheric Current Systems, Geophys. Monogr. Ser.*, vol. 118, edited by S. Othani et al., pp. 41–52, AGU, Washington, D. C.

Song, Y., and R. Lysak (2001), The physics in the auroral dynamo regions and auroral particle acceleration, *Phys. Chem. Earth Part C, 26*(1–3), 33–42, doi:10.1016/S1464-1917(00)00087-8.

Stenbaek-Nielsen, H. C., and T. N. Davis (1972), Relative motions of auroral conjugate points during substorms, *J. Geophys. Res., 77*(10), 1844–1858.

Stenbaek-Nielsen, H. C., and A. Otto (1997), Conjugate auroras and the interplanetary magnetic field, *J. Geophys. Res., 102*(A2), 2223–2232.

Tanaka, T. (2000), Field-aligned-current systems in the numerically simulated magnetosphere, in *Magnetospheric Current Systems, Geophys. Monogr. Ser.*, vol. 118, edited by S. Othani et al., pp. 53–59, AGU, Washington, D. C.

Paper III

How the IMF By induces a By component in the closed magnetosphere and how it leads to asymmetric currents and convection patterns in the two hemispheres

P. Tenfjord, N. Østgaard, K. Snekvik, K. M. Laundal, J. P. Reistad, S. Haaland, and S. E. Milan

Journal of Geophysical Research, Vol. 120, doi:10.1002/2015JA021579 (2015)

III

AGU PUBLICATIONS

JGR

Journal of Geophysical Research: Space Physics

RESEARCH ARTICLE
10.1002/2015JA021579

Key Points:
- The asymmetrically added flux to the lobes induces *By* in the closed magnetosphere
- Asymmetric FACs are created as a consequence of *y* directed tension contained in the return flow
- IMF *By* results in asymmetries in both currents, zonal flows, and auroras in the ionosphere

Correspondence to:
P. Tenfjord,
paul.tenfjord@ift.uib.no

Citation:
Tenfjord, P., N. Østgaard, K. Snekvik, K. M. Laundal, J. P. Reistad, S. Haaland, and S. E. Milan (2015), How the IMF B_y induces a B_y component in the closed magnetosphere and how it leads to asymmetric currents and convection patterns in the two hemispheres, *J. Geophys. Res. Space Physics*, *120*, 9368–9384, doi:10.1002/2015JA021579.

Received 15 JUN 2015
Accepted 16 OCT 2015
Accepted article online 19 OCT 2015
Published online 12 NOV 2015

How the IMF B_y induces a B_y component in the closed magnetosphere and how it leads to asymmetric currents and convection patterns in the two hemispheres

P. Tenfjord[1], N. Østgaard[1], K. Snekvik[1], K. M. Laundal[1], J. P. Reistad[1], S. Haaland[1,2], and S. E. Milan[1,3]

[1]Birkeland Centre for Space Science, Department of Physics and Technology, University of Bergen, Bergen, Norway, [2]Max Planck Institute for Solar System Research, Göttingen, Germany, [3]Department of Physics and Astronomy, University of Leicester, Leicester, UK

Abstract We used the Lyon-Fedder-Mobarry global magnetohydrodynamics model to study the effects of the interplanetary magnetic field (IMF) B_y component on the coupling between the solar wind and magnetosphere-ionosphere system. When the IMF reconnects with the terrestrial magnetic field with IMF $B_y \neq 0$, flux transport is asymmetrically distributed between the two hemispheres. We describe how B_y is induced in the closed magnetosphere on both the dayside and nightside and present the governing equations. The magnetosphere imposes asymmetric forces on the ionosphere, and the effects on the ionospheric flow are characterized by distorted convection cell patterns, often referred to as "banana" and "orange" cell patterns. The flux asymmetrically added to the lobes results in a nonuniform induced B_y in the closed magnetosphere. By including the dynamics of the system, we introduce a mechanism that predicts asymmetric Birkeland currents at conjugate foot points. Asymmetric Birkeland currents are created as a consequence of *y* directed tension contained in the return flow. Associated with these currents, we expect fast localized ionospheric azimuthal flows present in one hemisphere but not necessarily in the other. We also present current density measurements from Active Magnetosphere and Planetary Electrodynamics Response Experiment that are consistent with this picture. We argue that the induced B_y produces asymmetrical Birkeland currents as a consequence of asymmetric stress balance between the hemispheres. Such an asymmetry will also lead to asymmetrical foot points and asymmetries in the azimuthal flow in the ionosphere. These phenomena should therefore be treated in a unified way.

1. Introduction

The large-scale dynamics and morphology of the magnetosphere are primarily driven by dayside reconnection between the geomagnetic field and the interplanetary magnetic field (IMF) embedded in the solar wind. *Dungey* [1961] postulated that during southward directed IMF, reconnection would occur on the dayside, merging the terrestrial and the IMF and transferring magnetic flux from the dayside to the nightside. In the magnetotail, open flux transported from the dayside merges again and constitutes a second reconnection region. The cycle is completed when the flux is convected back to the dayside by the return flow. For purely southward directed IMF this mechanism can be assumed to produce symmetric ionospheric convection flows and a near-symmetric configuration in the magnetosphere between the northern and southern lobes.

The solar wind's IMF B_y component is believed to be the cause of a number of asymmetric features in both the magnetosphere and ionosphere [e.g., *Walsh et al.*, 2014]. In the presence of an IMF B_y component the location of the dayside reconnection site on the magnetopause changes (see Figures 1a and 1b or, e.g., *Wing et al.* [1995]). *Park et al.* [2006] found that for a finite IMF B_y, the dayside reconnection site moves from the subsolar point, toward high-latitude flanks, and concluded that antiparallel reconnection is dominant over component reconnection for such conditions, illustrated in Figures 1a and 1b. Also, reconnection now produces field lines which no longer convect in a purely antisunward direction but are instead deflected toward the dusk and dawn by the magnetic tension [*Cowley*, 1981]. This additional azimuthal flow on the dayside is added to the antisunward flow produced by the solar wind flow carrying open magnetic field lines.

AGU Journal of Geophysical Research: Space Physics 10.1002/2015JA021579

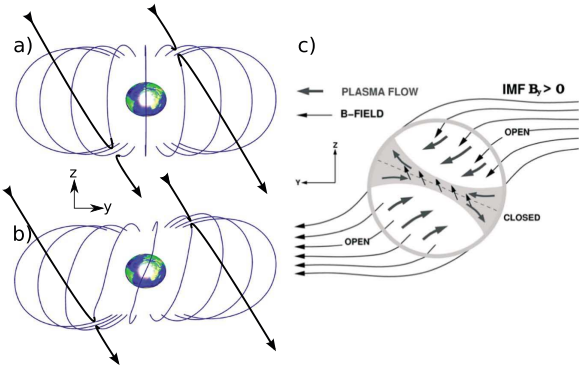

Figure 1. (a) Conceptual sketch of IMF (black lines) reconnection with the geomagnetic field (blue lines) when the IMF has a 135° clock angle. The figure serves as an illustration of the topology in the presence of IMF B_y. We assume purely antiparallel reconnection [*Park et al.*, 2006]. Reconnection produces field lines which no longer convect in a purely antisunward direction; instead, they are deflected toward the dusk and dawn by the magnetic tension. (b) Reconnection geometry altered by induced B_y on the closed dayside field lines. (c) Asymmetric entry of magnetic flux in the lobes during positive IMF B_y conditions [*Khurana et al.*, 1996; *Liou and Newell*, 2010].

In the ionosphere the original two cells are distorted into "banana"-shaped and "orange"-shaped convection regions. For positive B_y conditions a banana-shaped convection cell is observed in the dawn region and a rounder orange-shaped cell in the dusk region in the Northern Hemisphere. For negative B_y this is reversed. The convection pattern in the Southern Hemisphere is essentially a mirror image of the Northern Hemisphere with respect to the noon-midnight meridian [*Cowley*, 1981; *Provan et al.*, 2009; *Kabin et al.*, 2003]. The influence of IMF sector structure on the magnetic disturbances in the ionosphere was first shown by *Svalgaard* [1968] and *Mansurov* [1969]. Later, *Friis-Christensen et al.* [1972] attributed the observed behavior to the effect of IMF B_y.

Inside the closed magnetosphere a *y* component (or dawn/dusk) of the magnetic field arises, with the same direction as the component in the solar wind. What is often expressed as "penetration" of IMF B_y is a misleading term [e.g., *Kozlovsky*, 2003; *Petrukovich*, 2011]. Instead, we suggest to call it an *induced* B_y [e.g., *Khurana et al.*, 1996]. The term induced is used to explain the mechanism and processes leading to the B_y component inside the closed magnetosphere. A physical process such as dayside magnetic reconnection is needed to have the external B_y mapped into the system. Through plasma interactions (asymmetric lobe pressure and flux transport) a B_y component of the same sign as the external field is induced in the closed magnetosphere. By calling it induced we imply that it is not simply a result of vacuum superposition, where the magnitude in different regions is determined by the amount of "shielding" from the IMF B_y related penetration electric field, as often seen in the literature [e.g., *Kullen and Blomberg*, 1996; *Walker et al.*, 1999; *Kozlovsky*, 2003]. *Hau and Erickson* [1995] explained the asymmetric velocity v_y in the magnetosphere as due to a north-south electric field component in the solar wind which "penetrates" the tail, thereby causing the flow. The electric field has no power of penetration to drive the motion of the plasma; thus, an externally imposed electric field is unable to "penetrate" into the plasma [*Parker*, 1996; *Song and Vasyliunas*, 2011; *Vasyliunas*, 2012].

How B_y arises in the closed magnetosphere and the consequences are still debated. To our knowledge *Cowley* [1981] was the first to suggest that the post-reconnected field lines on the dayside were added preferentially to different magnetospheric regions (e.g., northern dawn and southern dusk for IMF $B_y > 0$). Whether B_y on closed field lines follows from the reconnection process in the magnetotail [*Hau and Erickson*, 1995; *Cowley*, 1981; *Stenbaek-Nielsen and Otto*, 1997; *Østgaard et al.*, 2004] or if the asymmetric loading of open flux also influences closed field lines [*Khurana et al.*, 1996] is still debated. *Khurana et al.* [1996] suggested that through asymmetric loading of flux into the different magnetospheric lobes, the shear flow (*y* directed)

AGU Journal of Geophysical Research: Space Physics 10.1002/2015JA021579

between northern and southern halves of the plasma sheet could generate a B_y component on closed field lines (see Figure 1c).

A relationship between interplanetary magnetic field (IMF) B_y and an induced B_y component in different magnetospheric regions has been established statistically [*Fairfield*, 1979; *Cowley and Hughes*, 1983; *Lui*, 1984; *Kaymaz et al.*, 1994; *Cao et al.*, 2014; *Stenbaek-Nielsen and Otto*, 1997; *Wing et al.*, 1995; *Petrukovich et al.*, 2005] and shows that the induced B_y is not distributed uniformly in the closed magnetosphere. *Wing et al.* [1995] found that a fraction of the IMF B_y component appeared at all local times but stressed that it was strongest near local noon and midnight. *Kaymaz et al.* [1994] showed that the induced B_y can be as large as 35% of the IMF B_y at the flanks, compared to 26% at the central portion of the plasma sheet. *Stenbaek-Nielsen and Otto* [1997] argued that during the evolution of a flux tube moving from the tail toward the Earth, flux will be accumulated (pileup) and thereby generate a region of enhanced B_y. We note that the asymmetries exist on both open and closed field lines.

The effects of the induced B_y have been extensively studied. The substorm onset location [*Liou and Newell*, 2010; *Liou et al.*, 2001; *Østgaard et al.*, 2011a] has been found to exhibit a longitudinal dependence on the presence of IMF B_y. A number of auroral studies have shown that there are systematic displacements and intensity differences [e.g., *Reistad et al.*, 2014; *Cowley*, 1981] in the aurora in the two hemispheres. The longitudinal displacement of aurora between the two hemispheres has been shown to correlate with IMF B_y [see *Østgaard et al.*, 2007, and references therein]. It is now generally accepted that aurora is a manifestation of Birkeland (field-aligned) currents [*Strangeway*, 2012]. Based on concurrent observations of the IMF orientation, *Stenbaek-Nielsen and Otto* [1997] have proposed a mechanism for how IMF B_y can give rise to interhemispheric currents between the two hemispheres. We present and discuss their mechanism in section 3. *Østgaard and Laundal* [2012] proposed that this mechanism could explain some of the nonconjugate auroral observations.

Milan [2015] has previously discussed the contributions of magnetic tension forces and asymmetrical loading of the lobes with new open flux to produce dawn-dusk asymmetries in flows in the magnetosphere-ionosphere system; the current paper investigates these influences from a mathematical and modeling perspective. Our motivation for the present work is to address how the presence of IMF B_y changes the dynamics and configuration in the magnetosphere. Furthermore, we investigate the consequences that follow in terms of induced B_y, asymmetric Birkeland currents, and associated convection patterns. We believe that these asymmetric azimuthal flows in both the dayside and nightside should be accompanied with nonconjugate aurora.

The paper is organized as follows: section 2 gives a theoretical background of the forces responsible for the evolution of B_y and v_y and their interdependency. Section 3 describes how IMF B_y induces B_y on closed field lines in the magnetosphere. We show how the forces are distributed and describe which forces are dominating in the different regions. We also discuss how convection cell patterns are modulated by the presence of IMF B_y. Results from our magnetohydrodynamics (MHD) model run are related to the equations introduced in section 2. In section 4 we introduce a mechanism that predicts asymmetric Birkeland currents on the same field line and argue that these are pairs of Birkeland currents instead of "interhemispheric" currents. In section 5 we present statistical data from Active Magnetosphere and Planetary Electrodynamics Response Experiment (AMPERE) and compare it to expected signatures from our mechanism. In section 6 we discuss the response time of the nightside magnetosphere with respect to the arrival of IMF B_y at the dayside magnetopause.

2. Theoretical Background

In this section we describe the governing MHD equations relevant for understanding how B_y is induced in the magnetosphere.

MHD can be expressed by a set of coupled interdependent dynamical equations. We use the momentum equation to determine how the forces can affect the flow and show how asymmetric transport of flux leads to an induced B_y. This induced B_y can again of course affect the flow, as the momentum equation is coupled with the induction equation. Apart from energy dissipation through Ohmic heating, magnetic stress remains stored in the system in the form of magnetic energy. The induced B_y in the magnetosphere can therefore be

AGU Journal of Geophysical Research: Space Physics 10.1002/2015JA021579

explained as a simple shoving match between stresses. The momentum equation can be written as [cf. *Parker*, 1996, 2007]

$$\rho\frac{\mathrm{d}v_i}{\mathrm{d}t} = \frac{\partial}{\partial x_j}M_{ij} - \frac{\partial}{\partial x_j}P_{ij} = \frac{1}{\mu_0}\left(\frac{\partial}{\partial x_j}(B_iB_j) - \frac{1}{2}\delta_{ij}\frac{\partial}{\partial x_j}B^2\right) - \frac{\partial}{\partial x_j}P_{ij} \tag{1}$$

where M_{ij}, P_{ij}, ρ, and v are the Maxwell stress tensor, pressure tensor, mass density, and velocity, respectively. The induced B_y in the magnetosphere can be understood in terms of the magnetic forces acting on plasma. In the following equations we consider how the magnetic field and the flow are modulated in the y direction. We focus on the y components since the additional forcing arising from IMF B_y acts primarily in this direction. The evolution of v_y, considering electromagnetic forces alone, is (assuming that the plasma pressure in the lobes is negligible)

$$\rho\frac{\mathrm{d}v_y}{\mathrm{d}t} = \frac{1}{\mu_0}\left(B_x\frac{\partial}{\partial x} + B_z\frac{\partial}{\partial z}\right)B_y - \frac{1}{2\mu_0}\frac{\partial}{\partial y}\left(B_x^2 + B_z^2\right) \tag{2}$$

M_{ij} has been expanded to four terms, the two first terms describe the tension along the field lines, and the two last magnetic pressure. The tension is related to the field line curvature: $\vec{T} = \frac{\partial}{\partial x_j}(B_iB_j) = B^2\frac{\hat{n}}{R_C}$, where R_C is the radius of curvature of the field line and $\hat{n}$ is unit vector pointing away from the center of curvature. For self-consistency we also need an equation to determine the evolution of the magnetic field, found by combining the Maxwell-Faraday equation with the conservation of mass:

$$\frac{\mathrm{d}\vec{B}}{\mathrm{d}t} = (\vec{B}\cdot\nabla)\vec{v} + \frac{\vec{B}}{\rho}\frac{\mathrm{d}\rho}{\mathrm{d}t} \tag{3}$$

where we have used $\vec{E} = -\vec{v}\times\vec{B}$ and the convective derivative is defined as $\frac{\mathrm{d}}{\mathrm{d}t} = \frac{\partial}{\partial t} + \vec{v}\cdot\nabla$. The y component of equation (3) can be expressed as

$$\frac{\mathrm{d}B_y}{\mathrm{d}t} = \left(B_x\frac{\partial}{\partial x} + B_y\frac{\partial}{\partial y} + B_z\frac{\partial}{\partial z}\right)v_y + \frac{B_y}{\rho}\frac{\mathrm{d}\rho}{\mathrm{d}t} \tag{4}$$

The three first terms on the right-hand side describe how v_y can change the magnetic field over time. These terms dominate when the assumption of incompressible flow holds. The assumption should be valid as long as density gradients are small (uniform flow) and the driving of the system can be considered steady (steady flow). We consider these terms to dominate in the outer magnetosphere [*Escoubet et al.*, 1997; *Laakso et al.*, 2002]. Considering regions where B_y has not yet been induced, the second term is negligible. In these regions, the induced B_y is attributed to the three remaining terms. The shear flow (flow induced by a force), v_y, is determined by equation (1).

The fourth term tells us that the change of B can be caused by compressing or expanding the plasma [*Hau and Erickson*, 1995]. This term becomes important in the inner magnetosphere. This can be used to explain what is called "pileup" of magnetic flux. As a magnetic field line is convected closer to Earth from the tail, the mass density increases with the magnetic field strength. *Stenbaek-Nielsen and Otto* [1997] suggested that since the magnetic field strength increases as the field lines convect earthward, and consequently also its B_y component, an interhemispheric current would arise due to the gradient in the x direction of the B_y. However, we will argue that this is not correct.

3. Generation of B_y in the Magnetosphere

In this section we present results from the Lyon-Fedder-Mobarry (LFM) [*Lyon et al.*, 2004; *Merkin and Lyon*, 2010] global MHD model. We interpret the results in terms of the forces acting to produce a B_y component in the magnetosphere and relate them to the equations introduced in section 2. The LFM model provides a self-consistent model of the global magnetosphere. Even though the model is based on the equations of ideal MHD, it has proven to be an extremely useful tool for studying the large-scale dynamics of the magnetospheric system [*Ridley et al.*, 2010]. Due to the lack of resistivity, magnetic reconnection does not exist in ideal MHD. Instead, diffusion is introduced by numerical effects, which comes about when magnetic field gradient scale length approaches the computational grid size [*Lyon et al.*, 2004; *Ouellette et al.*, 2010]. The model has several limitations, especially in the inner magnetosphere and in the self-consistency of the magnetosphere-ionosphere coupling [see *Ridley et al.*, 2010; *Tu et al.*, 2014].

AGU Journal of Geophysical Research: Space Physics 10.1002/2015JA021579

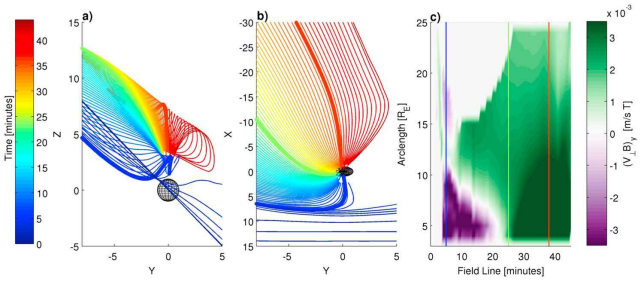

Figure 2. The evolution of a field line from the solar wind to the nightside reconnection region, (a) seen from the Sun and (b) down on the Northern Hemisphere. The color bar represents time with 30 s between each field line. Immediately after dayside reconnection, the field lines are forced dawnward by the tension (equation (2) and Figures 1a and 1b). After about 20 min the field is forced duskward by the accumulated pressure in the northern dawn lobe (Figure 1c). (c) The flux transport in the y direction, $(v_\perp B)_y$. The three vertical lines are colored in accord with the time code: blue, green, and red (shown as bold colored lines in Figures 1a and 1b) represent positions during the trace, for visualizing purpose only. The first 20 min the flux transport is directed dawnward, corresponding to the tension, followed by duskward transport due to pressure.

The solar wind conditions during the model run are $B_Z = -10$ nT and $V_X = -400$ km/s with zero dipole tilt. The IMF B_y is zero on the first 30 min of the run, followed by $B_y = 10$ nT on the remaining 2.5 h. Start time ($t = 0$) is defined as the time IMF B_y arrives at the dayside magnetopause. The data have been produced by Community Coordinated Modeling Center (CCMC) and are available as run number Paul-Tenfjord-032514-1.

We trace field lines as they evolve in time by using their perpendicular velocity at some initial time to calculate the location of the field line 30 s later. We also project the foot points of the field lines, by tracing the field lines to 3 R_E (model constraint) radius and use simple dipole mapping from this altitude. We acknowledge that the method relies on the field not departing from a dipole configuration between the surface and the 3 R_E altitude. We use the method to quantify the asymmetry of the foot points, defined to be the deviation (in ΔMLT) from a purely symmetric configuration. The deviation can be both latitudinal and longitudinal; we focus on the latter, often associated with IMF B_y. We discuss the dayside and the nightside separately.

3.1. B_y on the Dayside

In Figures 2a and 2b we follow a field line in the Northern Hemisphere from the solar wind to the nightside as it evolves over time. The colors indicate time, with 30 s between each field line. Figure 2a shows the field lines in the Y-Z plane. The solar wind approaches the magnetopause with a clock angle of 135°.

After dayside reconnection the solar wind plasma carries open magnetic field lines with it, while the foot points of these field lines remain anchored to the Earth. The transverse momentum from the solar wind flow is transmitted to the foot points such that they eventually move laterally.

Due to IMF B_y, there exists an additional tension in the field line just after the dayside reconnection. The tension (related to the field line curvature: $\vec{T} = \frac{\partial}{\partial x_j}(B_i B_j) = B^2 \frac{\hat{n}}{R_c}$; see equation (2)) is directed dawnward in the Northern Hemisphere ($\frac{dv_y}{dt} < 0$) and duskward in the Southern Hemisphere as shown in Figures 1a and 1b. Figure 2b shows the view in the Y-X plane. Due to the reconnection geometry of the terrestrial magnetic field, the tension is stronger on the dusk side compared to the dawn side in the Northern Hemisphere (Figures 1a and 1b). The tension term of equation (2) dominates over the pressure term. Immediately after dayside reconnection, the tension along x changes v_y as described by the momentum equation (for Northern Hemisphere: $B_x \frac{\partial B_y}{\partial x} < 0$, first term in equation (2)).

Figure 2c shows flux transport in the y direction along the arc length of each of the field lines. The tension acts on the newly reconnected open field lines on the dayside at about ∼10 R_E (arc length) during the first 8 min, seen in purple in Figure 2c. The part of the field lines outside the magnetosphere is not affected (top left). This purple region extends earthward; this is the tension propagating along the field line earthward

AGU Journal of Geophysical Research: Space Physics 10.1002/2015JA021579

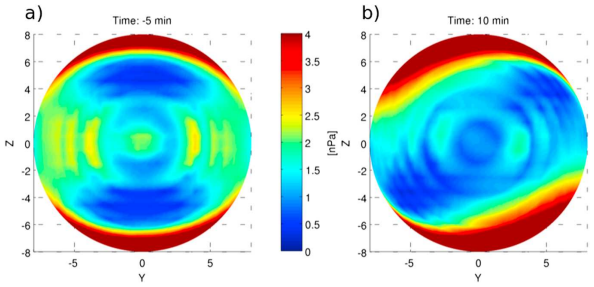

Figure 3. Magnetic pressure projected on a half sphere of size $R = 8\ R_E$, so that the center is at $X = 8\ R_E$, but the outmost values are at $X = 0\ R_E$. (a) Magnetic pressure 5 min prior to IMF $B_y = 10$ nT. (b) Ten minutes after IMF B_y arrived at magnetopause.

accelerating the plasma in the dawn direction. This Maxwell stress exerted on the ionosphere eventually moves the ionospheric foot points in the dawnward direction, seen as purple between 5 and 20 min.

After about 10 min, the magnetospheric part of the field line (arc length between 10 and 15 R_E) starts to experience the enhanced pressure in the northern lobe. The magnetic pressure in the lobes is a result of asymmetric loading of flux. The region of enhanced pressure is confined by the constant external stresses applied by the magnetosheath flow against the magnetopause, essentially maintaining a circular cross section of the magnetotail. This localized region of enhanced pressure (seen in green at about 10 min in Figure 2c) will start to force the magnetospheric plasma in the dusk direction ($(v_\perp B)_y > 0$). This transverse momentum is transmitted to the ionosphere, forcing the ionospheric foot points in the dusk direction after about 25 min. The field lines are now forced duskward and at the same time converge toward the neutral sheet (see Figure 1c). Eventually, they will reconnect with the approaching field lines from the southern lobes. The vertical colored lines in Figure 2c are added for visualization purpose only, and they represent the three field lines with larger line width in Figures 2a and 2b.

Figure 3 shows the magnetic pressure presented on a half sphere with radius 8 R_E looking from the Sun toward Earth. Figure 3a shows that the pressure distribution 5 min prior to IMF B_y has been introduced to the MHD model. Figure 3b shows that the configuration 10 min after IMF $B_y = 10$ nT. Figure 3b suggests that more flux is eroded from the northern dusk and southern dawn high-latitude regions and added asymmetrically to the northern dawn and southern dusk, respectively. The enhanced pressure in the northern dawn and southern dusk will also displace the existing closed field lines in the region. In the northern dawn and southern dusk the closed field lines will be compressed equatorward. The northern dusk and southern dawn are not affected. This asymmetric forcing will induce a latitudinal asymmetry in the foot points, as already noted in *Cowley et al.* [1991] (see their Figure 2). Also associated with these asymmetric forces are the twisting of the dayside field lines, which is analogous to an induced B_y. We agree with the conclusion of *Wing et al.* [1995] that the erosion of magnetic flux at the high-latitude flanks on the dayside, combined with the newly opened flux added to the dawn (for Northern Hemisphere, see Figure 3), will induce a B_y on the dayside. This in turn affects the dayside reconnection by changing the reconnection geometry. The altered reconnection geometry is shown in Figure 1b. The IMF reconnects with a twisted terrestrial field, causing an even greater tension on the newly reconnected field lines; see Figure 1b.

To summarize the effect of a positive IMF B_y component on the dayside, the field lines are forced both dawnward (by the tension) and at the same time tailward by the solar wind. Considerably more flux is added to the dawn side of the noon-midnight meridian compared to the dusk side in the Northern Hemisphere. The closed field lines on the dayside get twisted by the combination of erosion of flux at high-latitude flanks and by the increase of magnetic pressure in the northern dawn and southern dusk. The induced B_y on the dayside has the same sign as the IMF as sketched in Figure 1b and shown by *Burch et al.* [1985].

AGU Journal of Geophysical Research: Space Physics 10.1002/2015JA021579

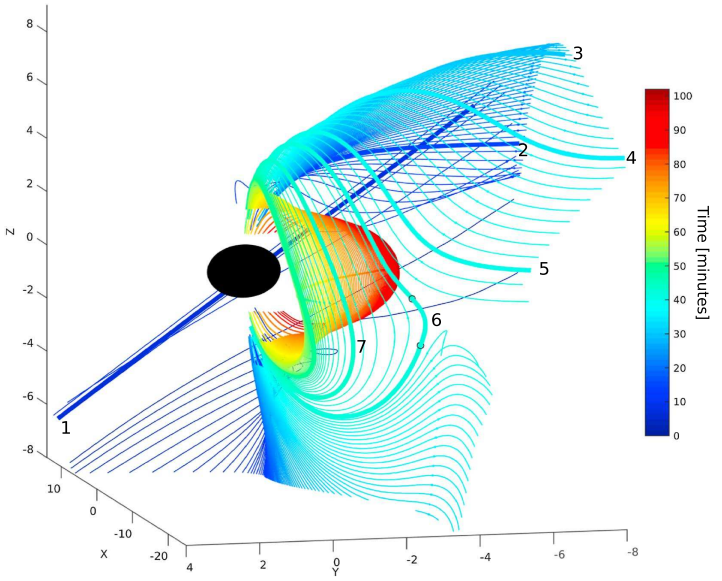

Figure 4. Illustration of a field line as it evolves over time from dayside reconnection (1), convection in the lobe (2–5), nightside reconnection (6), and earthward convection (7) (return flow) on dawn cell. Our starting point of the trace is the field line at (6); from this approximate reconnection site we trace backward in time (1–5) and forward in (6–7). Colors represent time. It takes approximately 45 min from dayside reconnection until the field reconnects again in the magnetotail. From the start of the return flow, we follow the field lines about 50 min until the foot points become symmetric again.

3.2. Nightside B_y

After this first phase, approximately after the field line has crossed the terminator plane, the magnetic pressure terms in equation (2) dominate (see Figure 2). In this second phase, the accumulated flux in the northern dawn and southern dusk dominates the evolution of v_y. For simplicity we can assume that all the y directed stress after the dayside reconnection is stored in the system as magnetic pressure (under the assumptions that the tension is removed in the passage from the dayside to the lobe, the magnetospheric pressure is confined and Joule heating is negligible).

The region of enhanced magnetic flux in the northern dawn and southern dusk is localized close to the terminator plane. The magnetic pressure localized in this region immediately forces both the incoming field lines and the surrounding field lines to move. The accelerated plasma will extend spatially as a direct result of the magnetosphere's attempt to restore pressure balance. The distribution of induced B_y in the magnetotail (and on the dayside) is a consequence of magnetic pressure accelerating the plasma. Even though it may appear that the asymmetric magnetic pressure is distributed far downtail, it is, in fact, the accelerated plasma that extends, inducing B_y as the plasma propagates. The magnetic field is transported with the plasma in the dusk (north) and dawn directions (south) in the magnetotail for IMF $B_y > 0$. At the same time the flux tubes are convected toward the neutral sheet. This means that the plasma propagates toward the neutral sheet at some angle (see Figures 4 and 1c). As this compression extends, it also affects the surrounding closed field lines, thereby inducing a B_y in the tail, independently of a reconnection process. This has previously been suggested by *Khurana et al.* [1996], as shown in Figure 1c. By the same arguments, this is also how the dayside

AGU Journal of Geophysical Research: Space Physics 10.1002/2015JA021579

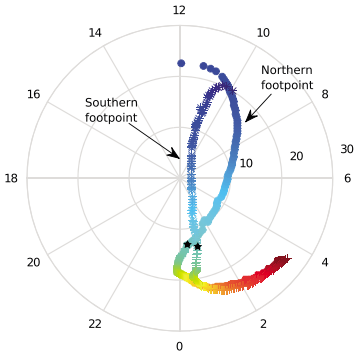

Figure 5. Corresponding foot points for Figure 5. Filled circles represent foot points in Northern Hemisphere and asterisk (∗) for Southern Hemisphere. The two black stars mark the time step when field lines go from open to close. The colors follow the colors in Figure 4. The flow (evolution of the foot point) in the north coincides with the crescent-shaped banana convection cell and is forced further toward dusk compared to the southern foot point. Eventually, as the foot points are forced toward lower latitudes (magnetospheric flow earthward), the northern foot points catch up with the southern foot points and they continue their convection toward the dawn-dusk meridian with symmetric foot points.

induced B_y arises. We also note that since the dayside field lines are twisted, the increased tension of the newly reconnected field lines results in an even greater magnetic pressure added to the lobes (see Figure 1b).

In Figure 4 we show the evolution of a newly reconnected field line (6) in the magnetotail viewed from the tail and rotated slightly toward dusk. From this approximate reconnection point we trace both backward and forward in time. Following the field lines backward in time (1–6), we trace them to the approximate same field line in the solar wind. However, we note that the convection over the Southern and Northern Hemispheres does not take the exact same amount of time, and we can therefore not claim that it is the same field line. Tracing forward in time (6–7), we observe an earthward and dawnward convection.

In Figure 5 we present the projected foot points of the field lines in Figure 4. An asterisk (∗) represents the foot points in Southern Hemisphere and filled circles the Northern Hemisphere. As mentioned the field lines start off at the approximate same field line in the solar wind. The foot points on the dayside after reconnection in Northern and Southern Hemispheres have asymmetric positions of ~2 h (12 h and 10 h magnetic local time (MLT), respectively), which is a signature of the twisted dayside magnetic field. Immediately after dayside reconnection, the foot point in the Northern Hemisphere convects dawnward, while the foot point in the Southern Hemisphere moves duskward. After about 25 min (see Figure 2c) the northern foot point moves in the duskward direction; directions are reversed in the Southern Hemisphere. As the field lines approach the neutral sheet (4–5 in Figure 4), at the angle dictated by the pressure distribution, the field lines reconnect. In Figure 5 the two black markers (~78° latitude) show the position of the start of the trace, which is a newly reconnected field line (6 in Figure 4).

They reconnect with asymmetric foot points. As they dipolarize and convect earthward (6–7 in Figure 4), the asymmetry increases, which is due to the distribution of the pressure forces. Eventually, the flux tubes are forced either dawnward or duskward by the plasma and magnetic pressure forces surrounding the Earth. As the flux tube starts to convect dawnward (green color markers), the foot point in the Northern Hemisphere is around 0 MLT, while the southern foot point is at 1 MLT. As time evolves, the foot points become more symmetric again, meaning that the azimuthal flow in the north has caught up with azimuthal flow in the Southern Hemisphere. Asymmetric azimuthal flows represent the large-scale rectifying of a twisted flux tube, which necessarily need to be accompanied by asymmetric Birkeland currents. In the next section, we will discuss how these differences in azimuthal flow relate to Birkeland currents on conjugate field lines.

Before we summarize the effects of IMF B_y on the nightside, the following question arises: how does reconnection manipulate the system, and which field lines actually reconnect? As shown above it is the force balance in the magnetosphere that dictates where the field lines from the different lobes converge. That is, the pressure distribution in the tail determines the direction in which the flow approaches the neutral sheet. As shown in Figure 5 the global MHD model suggests that they do indeed reconnect with asymmetric foot points. We acknowledge the uncertainty in both the location, tracing and of the model, in general, regarding details. There are uncertainties in the diagnostic methods which are very difficult to quantify; for instance, small errors may link two different field lines in the tracing procedure [*Song and Vasyliünas*, 2010]. The errors could also accumulate along the trace resulting in a large uncertainty. This is especially important in reconnection regions where the topology rapidly changes. Even though not able to quantify the uncertainty,

AGU Journal of Geophysical Research: Space Physics 10.1002/2015JA021579

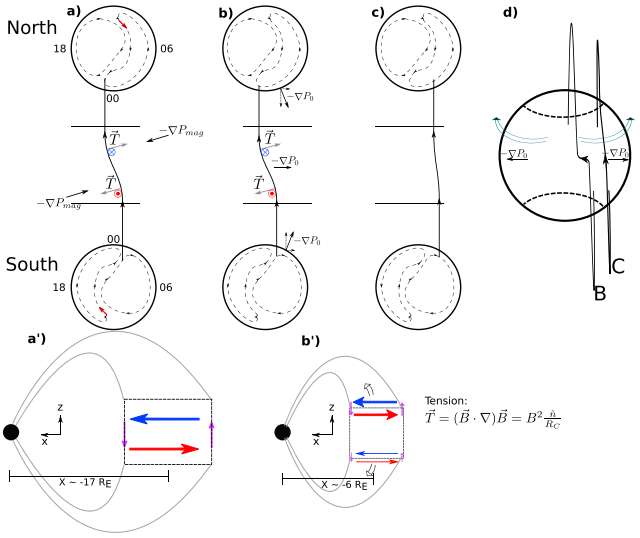

Figure 6. A flux tube on closed field lines with asymmetric foot points convecting on the dawn convection cell during IMF $B_y > 0$ conditions. (a–c) Pressure, tension, and asymmetric foot points into the dawn cell. (a′ and b′) The associated current systems seen from dusk. Figure 6a shows closed field line in midtail region around $X \sim -17\ R_E$ experiencing the asymmetric pressure from the lobes ∇P_{mag} which is balanced by the tension $\vec{T}$. Figure 6a′ shows currents closed locally. Figure 6b shows that field line convects earthward and is affected by the pressure (plasma and magnetic) surrounding Earth ∇P_0. Now the forces do not balance. In the Northern Hemisphere these forces point in the same direction. Hence, most of the stress is transmitted into this hemisphere, and the northern foot point will catch up with the southern counterpart to restore symmetry. Figure 6b′ shows a stronger current system deposited into the Northern Hemisphere, compared to the Southern Hemisphere. Figure 6c shows the Northern Hemisphere catching up with the southern foot point, making them symmetric. (d) View from magnetotail toward the Sun and shows the relaxation of the field line from Figures 6b to 6c.

we are confident that foot points in Figure 5 describe the behavior properly for the following reasons: (1) the evolution of the foot points is smooth and consistent. (2) Retracing the field lines after a small change in the location and a temporal shift reveals a comparable pattern. Nevertheless, our main point is the role of the pressure distribution, forcing the flux tubes in the *y* direction asymmetrically between the lobes. We interpret the morphology of reconnected field lines as a consequence of these asymmetric forces. We emphasize that the newly reconnected flux tube will continue to experience these forces, and in addition, the magnetic field strength increases as the field line dipolarize according to equation (4). This means that closed field lines present before IMF B_y arrived will also have an induced B_y independently of tail reconnection. In the next section we discuss this more thoroughly, including the resulting Birkeland currents.

3.3. Ionospheric Convection

In this section we review the consequences of the above asymmetric magnetospheric forcing for the properties of flows in the ionosphere. An illustration of the convection patterns for Northern and Southern Hemispheres is shown in Figure 6a for IMF $B_y > 0$. In the presence of IMF B_y the normal two-cell convection pattern is modified into what is known as banana and orange cells [*Heppner*, 1972; *Mozer et al.*, 1974; *Heppner and Maynard*, 1987; *Cowley et al.*, 1991; *Haaland et al.*, 2007; *Grocott and Milan*, 2014]. A crescent banana convection cell is seen on the dawn cell in the Northern Hemisphere, while the convection cell on the dusk side has a more rounded orange shape (opposite for Southern Hemisphere). The banana-shaped convection cell can extend into the premidnight and postnoon regions (see Figure 6a and Figure 5).

AGU Journal of Geophysical Research: Space Physics 10.1002/2015JA021579

The shape of convection cells is determined by the imposed force from the magnetosphere. On the dayside the tension on the newly opened field lines is forced dawnward in the Northern Hemisphere and southward in the Southern Hemisphere; see red arrows in Figure 6a. The associated $\vec{J} \times \vec{B}$ force is transmitted down to the ionosphere accelerating the ionospheric plasma in the direction dictated by the imposed force, resulting in the crescent dawn cell and rounded dusk cell in the Northern Hemisphere. On the nightside it is the pressure distribution in the lobes that forces the ionospheric convection duskward. When we follow a field line from the nightside reconnection region as it convects toward Earth, the pressure (∇P_0-plasma plus magnetic) surrounding Earth will force the field line to convect either on the dawn cell or the dusk cell. In the next section we discuss the associated current system required when the flow proceeds on a banana cell in the Northern Hemisphere and on an orange cell in the Southern Hemisphere. This corresponds to the dawn cell for IMF $B_y > 0$.

Finally, we notice that we have considered dayside reconnection alone as the source of the asymmetric pressure distribution in the magnetosphere, which in turn induces B_y. In fact, there are other mechanisms that can produce B_y, such as warping of the plasma sheet [*Russel*, 1972; *Tsyganenko*, 1998; *Liou and Newell*, 2010], lobe reconnection, magnetotail twisting, and tilt effects [*Petrukovich et al.*, 2005; *Petrukovich*, 2011]. Also, we have not included nor discussed any consequences of ionospheric properties such as conductivity, conductivity gradients, and/or other ion-neutral interactions. We note that the effects of these processes may amplify or mitigate the signatures of the mechanisms.

4. Generation of Birkeland Currents Due To B_y

In this section we discuss the asymmetric Birkeland currents on the nightside, arising as a consequence of an induced B_y component in the magnetosphere. By definition, Birkeland currents transmit the transverse momentum (i.e., magnetic tangential stress) and energy from the source region to the region of dissipation, along magnetic field lines [*Iijima*, 2000].

That is, the Birkeland currents are a consequence of perpendicular (to B) perturbations along the magnetic field lines. The closure current (Pedersen current) is at the wavefront of the associated Alfvèn wave. The electric current is a result of the interplay of the forces in the momentum equation. Since the associated electric fields and current play no role in the dynamics (they are created and driven by the varying B and v [*Parker*, 2007]), we argue that the ionospheric signatures are better understood in terms of forces and flows. For this reason it is reasonable to discuss the force balance in context of the Birkeland currents. The Birkeland currents transport the tangential stress from the source in the tail, which is a result of asymmetric loading of flux.

4.1. Asymmetric Birkeland Currents

We now present a framework in which we predict asymmetric Birkeland currents as a result of induced B_y.

In Figures 6a–6c we show a conceptual illustration of a field line in the magnetotail at different stages of its evolution. We consider a field line that convects along the dawn cell.

In this illustration B_y is defined as finite and positive inside the boxes (Figures 6a′ and 6b′) and zero elsewhere. The gradients of B_y along the x direction are clearly defined as step functions at the boundaries, and the resulting Birkeland currents (violet arrows) are represented as infinitesimally thin sheets (Figures 6a′ and 6b′). In reality the limits of the perturbation are not so impulse like and distributed over a larger area.

Figures 6a and 6a′ show a closed, midtail field line in the magnetotail region. The asymmetric loading of flux to the lobes exerts an asymmetric pressure on the field line, directed duskward in the northern lobe, and dawnward in the southern lobe. The foot points of the field line are asymmetric. The field line is twisted by the magnetic pressure. An opposing tension acts to balance the magnetic pressure $-\nabla P_{\mathrm{mag}}$ (Figure 6a and equation (2)). These forces could, in general, balance, resulting in a force-free configuration. The current system of such an equilibrium is shown in Figure 6a′. In this situation, the current system is locally closed, the perturbation is not propagating, and currents are dissipationless. In the midtail region, the closed field lines are highly nondipolar; magnetic tension forces the field lines earthward; see Figures 6b and 6b′. Due to the finite extent of the magnetic pressure distribution in the lobes, the force acting on the flux tube is now dominated by the combined magnetic and particle pressure surrounding Earth, $-\nabla P_0$. This force acts radially outward from Earth. The twisted field line can now start to relax. In Figure 6b, $-\nabla P_0$ is directed parallel to the tension in the northern lobes and antiparallel to the tension in the southern lobe. The current system for this situation is shown in Figure 6b′. The northern part of the field line deposits the majority of the tension stored in

AGU Journal of Geophysical Research: Space Physics 10.1002/2015JA021579

the flux tube to the Northern Hemisphere, since $-\nabla P_0$ and the tension $\vec{T}$ act in the same direction (Figure 6b). The current system propagating down to the northern ionosphere is therefore larger than in the Southern Hemisphere. We stress that the current systems illustrated here are isolated from the "normal-" driven Region 1 (R1) and Region 2 (R2) systems. If the current system belonging to Figure 6b were to be superimposed with the return flow-generated R1 and R2 currents, the result would be two current systems with equal (symmetric) direction but with different magnitude. Figure 6c shows the situation when the flux tube has relaxed and the foot points are again symmetric. In this configuration the foot point in the Northern Hemisphere has moved faster to catch up with the foot point in the south. That is because the magnetosphere imposed a stronger flow dawnward in the northern lobe (as we showed in Figure 5), resulting in a stronger Pedersen current to propagate down which in turn accelerates the ionospheric plasma. The flux tube would then continue to convect without tension and with symmetric foot points toward the dayside. Figure 6d shows the flux tube as viewed from the tail toward the Sun, corresponding to Figures 6b and 6c. Here we have emphasized that the northern foot point will move a larger distance and hence faster, compared to the Southern Hemisphere.

It is important to include the dynamics of the mechanism. During the evolution of the twisted field line it experiences different forces (varying amount of pressure gradient and curvature and Earth's surrounding pressure), and only when one views these different interactions in a unified way are we able to describe the mechanism properly.

Consequently, one would expect to observe a pair of asymmetric Birkeland currents connecting to the two hemispheres, not necessarily crossing the neutral sheet. The source of the tangential stress is in the magnetotail region, and it is oppositely directed in the northern and southern lobes. The stress from the source region is transmitted to the ionosphere via Alfvèn waves. The force balance exists between each ionosphere and the magnetotail separately. The forces and energy may be distributed asymmetrically; for IMF $B_y > 0$ a larger stress will be transmitted to the northern postmidnight region, and southern premidnight, which should result in asymmetries in both currents, azimuthal flows, and auroras.

We note that each ionosphere may respond differently to applied magnetospheric stress owing to differences in ionospheric properties [*Tu et al.*, 2014].

4.2. Interhemispheric Currents

In this section we present the proposed mechanism by *Stenbaek-Nielsen and Otto* [1997], where they suggest that observed hemispherical difference in the aurora is a consequence of interhemispheric currents. An interhemispheric current is defined as a current flowing between two conjugate ionospheres [*Lyatskaya et al.*, 2014]. We also discuss why we do not agree with their conclusions on the existence of an interhemispheric current driven by the magnetosphere.

As first suggested by *Stenbaek-Nielsen and Otto* [1997], the induced B_y is not distributed uniformly in the closed magnetosphere but tends to increase toward the Earth due to the pileup of magnetic flux toward the inner edge of the plasma sheet, as illustrated in Figure 7. This has been shown empirically. On the nightside, *Wing et al.* [1995] found that 79% of the IMF B_y induces a B_y component at $X = -6.6\ R_E$, for $-30 < X < -10\ R_E$ *Lui* [1984] found 50%, and further downtail between $-33 < X < -20\ R_E$ *Fairfield* [1979] found the induced B_y component to be 13% of the IMF B_y strength. This can be understood in terms of the forth term in equation (4); for steady flow and no shear flows the change of B_y is given by $\frac{dB_y}{dt} = \vec{v} \cdot \nabla \rho$. The second assumption would be valid if B_y on closed field lines on the nightside was due to reconnection with asymmetric foot points only [e.g., *Stenbaek-Nielsen and Otto*, 1997]. If so, as the closed field lines convect earthward, they would experience a positive gradient in the density and thereby intensify B_y (along with B_x and B_z). However, we argue that B_y is induced by the shear motion created by the asymmetric loading of flux from the dayside, and therefore, the three first terms in equation (4) should be included. This is further supported by the short response time discussed in section 6.

On field lines with L value $<\sim 6\ R_E$, the field again becomes symmetric. *Stenbaek-Nielsen and Otto* [1997] suggested that due to Ampere's law, a gradient of B_y along the x axis implies a current along the z axis (see Figure 7), forming an interhemispheric current. This mechanism is shown in Figure 7 for the case of IMF B_y positive. The direction of the currents in Figure 7 is consistent with those shown in Figures 6a′ and 6b′.

However, we do not agree with the terminology used in *Stenbaek-Nielsen and Otto* [1997], and we argue that the system can be properly understood only when the dynamics are included. We argue that the currents proposed by *Stenbaek-Nielsen and Otto* [1997] are not interhemispheric currents. They are not interhemispheric

AGU Journal of Geophysical Research: Space Physics 10.1002/2015JA021579

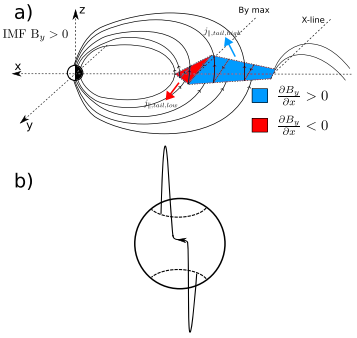

Figure 7. (a) Illustration of induced $B_y > 0$ in the closed magnetosphere and how the pileup region results in a gradient in B_y, which would according to the authors result in an interhemispheric current (remake of *Stenbaek-Nielsen and Otto* [1997, Figure 4]). (b) View from the magnetotail toward the Sun.

in the sense that they cross the neutral sheet (or equatorial plane) or that the pressure balance exists between the foot points in each hemisphere.

Instead, we consider this as two pairs of currents systems. The opposite-directed stresses from the magnetospheric source region (Figures 6a′ and 6b′ red and blue arrows) are exerted on each ionosphere. However, the force balance does not exist between the two ionospheres but between the near-Earth magnetosphere and each ionosphere separately. The magnitude of the currents in these two current systems is determined by the forces and energy flux which are asymmetrically shared between the magnetospheric source plasma and the two ionospheres. By arguments given above there should be no net Birkeland current flowing between the two hemispheres. Instead, a pair of flux tubes carrying balanced Birkeland currents closes by transverse currents in each ionosphere as well as in the source region near the equator (Figure 6). In Figure 6 the magnitude of the currents in the two systems has different magnitude due to the pressure surrounding Earth (∇P_0) opposing the stress in one hemisphere and is parallel in the other. We note that any additional ionospheric asymmetries, such as differences in conductivity between the hemispheres, could enhance or mitigate the asymmetry of the current magnitudes.

We suggest that the term interhemispheric currents should be reserved to explain situations where one ionosphere is active (source) and is driving a current to opposite ionosphere. In such a situation the force balance exists between the two foot points, and the current does, in fact, cross the equatorial plane.

5. Observation of Asymmetric Birkeland Currents

The Active Magnetosphere and Planetary Electrodynamics Response Experiment (AMPERE) provides global continuous sampling of the magnetic field perturbations [*Anderson et al.*, 2000; *Waters et al.*, 2001; *Korth et al.*, 2004; *Anderson et al.*, 2008]. We constructed statistical maps sorted by IMF $B_y > 0$. We use the stability criteria defined by *Anderson et al.* [2008], requiring only slowly changing currents. We note that the signatures discussed below are also clearly seen without the stability criteria.

The dayside R1 and R2 currents are modulated by the presence of IMF B_y. Figure 8 shows a statistical current density map for the Northern and southern Hemispheres. We discuss the Northern Hemisphere and IMF $B_y > 0$ unless stated otherwise. The magnetosphere imposes a flow dawnward on the dayside (see Figure 2). This, in turn, requires a corresponding Pedersen current. This closure current is transmitted by Alfvèn waves, and the associated Birkeland currents serve to transmit the energy and momentum to the ionosphere. Upward current corresponds to downward electrons flowing into the ionosphere, and we expect auroral signatures. Opposite behavior in the Southern Hemisphere results in asymmetric aurora. Ionospheric flows are a consequence of momentum transport from the magnetosphere and therefore must be associated with Birkeland current closing in the ionosphere. In the Northern Hemisphere, one observes a "R1" current flowing into (blue) the ionosphere around noon around $\lambda \sim 75°$ and a current flowing out of the ionosphere (red) at higher latitudes. These are signatures of an imposed dawn-directed magnetospheric flow, set up immediately after dayside reconnection by the tension along the field line. The resulting $\vec{J} \times \vec{B}$ force in the ionosphere accelerates the plasma dawnward in the Northern Hemisphere (see Figure 2) and duskward in the Southern Hemisphere. This describes the sunward part of the banana convection cell in the northern dawn region (see section 3.3). The dusk region convection cell has the characteristic orange shape.

On the nightside the signatures are seen as a rotation of the current systems between the hemispheres. The relative rotation is about 2 h MLT, represented by the dashed lines in Figure 8. In order to compare the current

AGU Journal of Geophysical Research: Space Physics 10.1002/2015JA021579

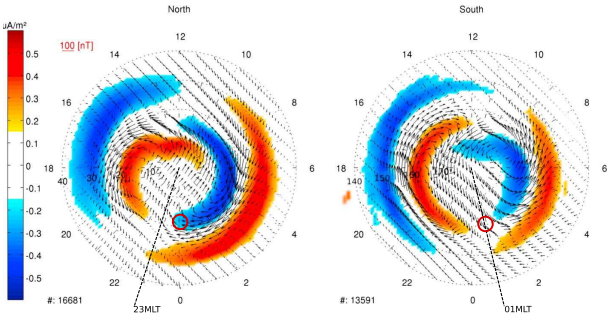

Figure 8. Statistical AMPERE maps for $B_z < 0$ and $B_y > 5$ and a stability criterion > 0.45 [see *Anderson et al.*, 2008] in the (left) Northern and (right) Southern Hemispheres. Colors indicate current density (red: away from and blue: into ionosphere), and arrows are the measured magnetic perturbations. The R1 and R2 current systems are rotated about 2 h MLT on the nightside compared to non-B_y conditions as visualized with the dashed lines at ~23 MLT and ~1 MLT. The red circles represent an example of two conjugate locations where the current density can be compared between the hemispheres.

density between the hemispheres, we must first assess the asymmetry of the conjugate foot points (Δ MLT). That is, in order to compare the current density at conjugate positions, we must first determine the asymmetry of the foot point (related to the twisting of the field) of the field lines. Studies by *Østgaard et al.* [2004, 2011b] and *Reistad et al.* [2013] suggest ΔMLT ~ 1 h; this MHD model suggests approximately the same; Tsyganenko models suggest only a fraction of that [*Østgaard et al.*, 2007].

The two red circles in Figure 8 represent two comparable regions under the assumption of ΔMLT = 1 h. With the assumption in mind, we believe that asymmetries in the nightside currents are seen in the AMPERE maps. This suggests asymmetric azimuthal flows, which have been observed with Super Dual Auroral Radar Network [e.g., *Grocott et al.*, 2007].

A study by [*Østgaard et al.*, 2011b] showed the evolution of the asymmetry of the foot points (measured by ΔMLT) during a substorm. The authors found that during the expansion phase of the substorms analyzed the asymmetry disappears. Although, we do not agree with their theoretical arguments, in particular the presence of a net field-aligned current between hemispheres and the role of $\Delta E_{\parallel}$ in the asymmetry of the ionospheric motion. Their observations are consistent with the mechanism we have presented, which is based on magnetic tension and asymmetric azimuthal flows between the two hemispheres.

6. Response Time

An important question to understand the dynamics of the system is as follows: how long does it take to produce the induced B_y in the magnetotail?

In our simulation model input the IMF B_y changes from 0 to 10 nT as a simple step function. Both the magnetosphere and ionosphere respond to the change by reconfiguring into a state consistent with the new IMF. The reconfiguration time depends on density and magnetic field strength and is therefore different in the various regions in the magnetosphere. Our estimates presented below are considered as the response time for reaching a new equilibrium.

On the dayside, the twisting of the field lines will evolve as more and more fluxes are removed from northern dusk and added to northern dawn until it saturates with some "efficiency." The closed field lines are affected on the same timescale as the open flux is added to the magnetosphere. Figure 3 shows that after only ~10 min the pressure is distributed asymmetrically; this will in turn force the closed field lines to twist effectively inducing a B_y on timescales less than 15 min. Figure 1b shows the dayside closed field lines at L ~7.5 R_E approximately 20 min after IMF B_y arrived. On the nightside we have presented model runs where we follow the field lines in time from the dayside reconnection and to the magnetotail.

AGU Journal of Geophysical Research: Space Physics 10.1002/2015JA021579

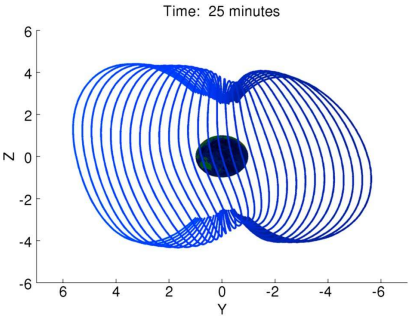

Figure 9. Closed field lines on nightside at $L = 11\ R_E$, 25 min after the arrival of IMF B_y.

The model suggests that a newly reconnected field line on the dayside undergoes tail reconnection after approximately 45 min. However, the buildup of asymmetric pressure in the lobes is established on much shorter timescales. We argue that the magnetic pressure induced by the asymmetrical loading of flux would induce a B_y on the existing closed field lines. This implies that the asymmetric pressure will induce a B_y on the already present field lines long before the actual field line reconnects in the tail. It is the compressional waves that propagate perpendicular to the magnetic field that affects existing magnetic field lines. The speed of fast-mode waves has been reported to be about 900 km/s [*Wilken et al.*, 1982]. We therefore argue that the time it takes to induce a B_y in the closed magnetosphere is significantly less than the actual convection time from dayside to nightside reconnection (see Figure 2). Figure 9 shows nightside closed field lines at $L = 11\ R_E$ just 25 min after IMF B_y arrived at the dayside magnetopause. The closed field lines are clearly twisted, and the induced B_y has been established on timescales less than the convection time from the dayside magnetopause to nightside reconnection. Observationally, the lag time of the response from the arrival of IMF at the magnetopause has been shown to be about 10 min on the nightside [*Wing et al.*, 2002]. In a study comparing the IMF clock angle and substorm onset location, *Østgaard et al.* [2011a] found highest correlation when time shifting the data <10 min, which is also consistent with what we have described and the model results. The timing of the magnetospheric and convection response has also been thoroughly discussed by *Ruohoniemi et al.* [2002]. A future project will use spacecraft data and modeling to confirm the response timing.

7. Summary

In the current work we have addressed how IMF B_y modulates the dynamics and morphology in the magnetosphere and the resulting signatures in the ionosphere.

The process of inducing B_y on nightside closed field lines originates on the dayside. When the IMF possess a B_y component, flux will be added asymmetrically to the magnetosphere via the dayside reconnection process. The governing equations describing the coupling between magnetospheric flow and magnetic tension and pressure are discussed in section 2. The asymmetric distribution of magnetic flux between the hemispheres creates shear flows, acting to restore equilibrium, and will influence existing field lines on both the dayside and nightside, effectively inducing a B_y component. The Maxwell stress exerted on the ionosphere by the tension and pressure of the displaced magnetic flux bundle distorts the ionospheric convection patterns into the characteristic banana and orange cell patterns. We have emphasized the importance of including the dynamical behavior of the system. As the field line convects from the midtail region, it initially experiences asymmetric lobe forces, which twists the field lines. At a later time in the evolution it starts to experience the pressure surrounding Earth which forces the field line to convect either dawnward or duskward, while the lobe pressure is reduced. Eventually, the field line relaxes and tension in field line (induced by the lobe pressure) is released mostly to one of the hemispheres. The result is asymmetric Birkeland currents at conjugate foot points, consistent with the convection patterns. The magnetosphere's response to the impact of IMF B_y has been discussed, and from the modeling perspective we argue that B_y is induced on dayside on timescales of a few minutes and in tens of minutes for the nightside. We presented statistical current density maps from AMPERE. We believe that asymmetric currents at conjugate foot points on the nightside are present in the statistical maps. The underlying assumption is that the rotation of the current systems is smaller than the relative shift of the conjugate foot points, since it is the current density in the conjugate foot points that must be compared. Several studies have reported on fast nightside azimuthal flows associated with IMF B_y [e.g., *Pitkänen et al.*, 2015; *Grocott et al.*, 2007, and references therein].

AGU Journal of Geophysical Research: Space Physics 10.1002/2015JA021579

Below we summarize the impact of IMF B_y on the magnetosphere and ionosphere system:

1. In the presence of IMF $B_y \neq 0$, dayside reconnection results in a asymmetrical distribution of flux between the hemispheres.
2. The asymmetric magnetic pressure in the lobes leads to asymmetric plasma flows and thereby induces B_y on closed field lines on both the dayside and nightside and forces asymmetric displacement of the ionospheric foot points.
3. In the ionosphere, asymmetric azimuthal flows arise, manifested as convection on a banana cell in one hemisphere and an orange cell in the other.
4. B_y is induced independently of nightside reconnection. It occurs on timescales less than 20 min for nightside closed field lines.
5. Asymmetric Birkeland currents (connected to different MLT locations in ionosphere) form as a consequence of the field line convecting from a region of dominating magnetic lobe pressure to an area where the pressure surrounding Earth is dominating. The tension is released into the hemisphere where the tension and Earth pressure act in the same direction.
6. For IMF $B_y > 0$ we expect stronger currents in the northern postmidnight dawn region and in the southern premidnight dusk region. For IMF $B_y < 0$ the signatures are reversed.
7. Rather than interhemispheric currents, we argue that the induced B_y results in pairs of asymmetric Birkeland currents.
8. Signatures of asymmetric currents are seen in AMPERE, primarily as relative rotation of hemispheric patterns.

Acknowledgments
We acknowledge the use of NASA/GSFC's Space Physics Data Facility for OMNI data. Simulation results have been provided by the Community Coordinated Modeling Center at Goddard Space Flight Center through their public Runs on Request system (http://ccmc.gsfc.nasa.gov). The CCMC is a multiagency partnership between NASA, AFMC, AFOSR, AFRL, AFWA, NOAA, NSF, and ONR (Paul-Tenfjord-032514-1). We thank the AMPERE team and the AMPERE Science Center for providing the Iridium-derived data products. This study was supported by the Research Council of Norway/CoE under contract 223252/F50.

References

Anderson, B. J., K. Takahashi, and B. A. Toth (2000), Sensing global Birkeland currents with Iridium engineering magnetometer data, *Geophys. Res. Lett.*, *27*(24), 4045–4048, doi:10.1029/2000GL000094.

Anderson, B. J., H. Korth, C. L. Waters, D. L. Green, and P. Stauning (2008), Statistical Birkeland current distributions from magnetic field observations by the Iridium constellation, *Ann. Geophys.*, *26*, 671–687, doi:10.5194/angeo-26-671-2008.

Burch, J. L., P. H. Reiff, J. D. Menietti, R. Heelis, W. B. Hanson, S. D. Shawhan, E. G. Shelley, M. Sugiura, D. R. Weimer, and J. D. Winningham (1985), IMF By-dependent plasma flow and Birkeland currents in the dayside magnetosphere: 1. Dynamics explorer observations, *J. Geophys. Res.*, *90*, 1577–1593.

Cao, J., A. Duan, M. Dunlop, W. Xinhua, and C. Cai (2014), Dependence of IMF B_y penetration into the neutral sheet on IMF B_z and geomagnetic activity, *J. Geophys. Res.*, *119*, 5279–5285, doi:10.1002/2014JA019827.

Cowley, S. (1981), Magnetospheric asymmetries associated with the y-component of the IMF, *Planet. Space Sci.*, *29*(1), 79–96, doi:10.1016/0032-0633(81)90141-0.

Cowley, S., and W. Hughes (1983), Observation of an IMF sector effect in the Y-magnetic field component at geostationary orbit, *Planet. Space Sci.*, *31*(1), 73–90, doi:10.1016/0032-0633(83)90032-6.

Cowley, S., J. Morelli, and M. Lockwood (1991), Dependence of convective flows and particle precipitation in the high-latitude dayside ionosphere on the X and Y components of the interplanetary magnetic field, *J. Geophys. Res.*, *96*, 5557–5564, doi:10.1029/90JA02063.

Dungey, J. W. (1961), Interplanetary magnetic field and the auroral zones, *Phys. Rev. Lett.*, *6*, 47–48, doi:10.1103/PhysRevLett.6.47.

Escoubet, C. P., A. Pedersen, R. Schmidt, and P. A. Lindqvist (1997), Density in the magnetosphere inferred from ISEE 1 spacecraft potential, *J. Geophys. Res.*, *102*(A8), 17,595–17,609, doi:10.1029/97JA00290.

Fairfield, D. H. (1979), On the average configuration of the geomagnetic tail, *J. Geophys. Res.*, *84*, 1950–1958, doi:10.1029/JA084iA05p01950.

Friis-Christensen, E., K. Lassen, J. Wilhjelm, J. M. Wilcox, W. Gonzalez, and D. S. Colburn (1972), Critical component of the interplanetary magnetic field responsible for large geomagnetic effects in the polar cap, *J. Geophys. Res.*, *77*(19), 3371–3376, doi:10.1029/JA077i019p03371.

Grocott, A., and S. E. Milan (2014), The influence of IMF clock angle timescales on the morphology of ionospheric convection, *J. Geophys. Res. Space Physics*, *119*, 5861–5876, doi:10.1002/2014JA020136.

Grocott, A., T. Yeoman, S. Milan, O. Amm, H. Frey, L. Juusola, R. Nakamura, C. Owen, H. Rème, and T. Takada (2007), Multi-scale observations of magnetotail flux transport during IMF-northward non-substorm intervals, *Ann. Geophys.*, *25*(2002), 1709–1720, doi:10.5194/angeo-25-1709-2007.

Haaland, S. E., G. Paschmann, M. Förster, J. M. Quinn, R. B. Torbert, C. E. McIlwain, H. Vaith, P. A. Puhl-Quinn, and C. A. Kletzing (2007), High-latitude plasma convection from Cluster EDI measurements: Method and IMF-dependence, *Ann. Geophys.*, *25*, 239–253, doi:10.5194/angeo-25-239-2007.

Hau, L., and G. Erickson (1995), Penetration of the interplanetary magnetic field B_y into Earth's plasma sheet, *J. Geophys. Res.*, *100*(2), 745–751.

Heppner, J. P. (1972), Polar-cap electric field distributions related to the interplanetary magnetic field direction, *J. Geophys. Res.*, *77*(25), 4877–4887, doi:10.1029/JA077i025p04877.

Heppner, J. P., and N. Maynard (1987), Empirical high latitude electric field models, *J. Geophys. Res.*, *92*, 4467–4489.

Iijima, T. (2000), Field-aligned currents in geospace: Substance and significance, in *Magnetospheric Current Systems*, edited by S. Ohtani et al., pp. 107–129, AGU, Washington, D. C., doi:10.1029/GM118p0107.

Kabin, K., R. Rankin, R. Marchand, T. I. Gombosi, C. R. Clauer, A. J. Ridley, V. O. Papitashvili, and D. L. DeZeeuw (2003), Dynamic response of Earth's magnetosphere to B_y reversals, *J. Geophys. Res.*, *108*(A3), 1132, doi:10.1029/2002JA009480.

Kaymaz, Z., G. L. Siscoe, J. G. Luhmann, R. P. Lepping, and C. T. Russell (1994), Interplanetary magnetic field control of magnetotail magnetic field geometry: IMP 8 observations, *J. Geophys. Res.*, *99*, 11,113–11,126, doi:10.1029/94JA00300.

Khurana, K. K., R. J. Walker, and T. Ogino (1996), Magnetospheric convection in the presence of interplanetary magnetic field B_y: A conceptual model and simulations, *J. Geophys. Res.*, *101*, 4907–4916.

AGU Journal of Geophysical Research: Space Physics 10.1002/2015JA021579

Korth, H., B. J. Anderson, M. J. Wiltberger, J. G. Lyon, and P. C. Anderson (2004), Intercomparison of ionospheric electrodynamics from the Iridium constellation with global MHD simulations, *J. Geophys. Res.*, *109*, A07307, doi:10.1029/2004JA010428.

Kozlovsky, A. (2003), IMF B_y effects in the magnetospheric convection on closed magnetic field lines, *Geophys. Res. Lett.*, *30*(24), 2261, doi:10.1029/2003GL018457.

Kullen, A., and L. O. Blomberg (1996), The influence of IMF on the mapping between the Earth's magnetotail and its ionosphere, *Geophys. Res. Lett.*, *23*(18), 2561–2564.

Laakso, H., R. Pfaff, and P. Janhunen (2002), Polar observations of electron density distribution in the Earth's magnetosphere: 1. Statistical results, *Ann. Geophys.*, *20*(11), 1711–1724, doi:10.5194/angeo-20-1711-2002.

Liou, K., and P. T. Newell (2010), On the azimuthal location of auroral breakup: Hemispheric asymmetry, *Geophys. Res. Lett.*, *37*, L23103, doi:10.1029/2010GL045537.

Liou, K., P. T. Newell, D. G. Sibeck, C.-I. Meng, M. Brittnacher, and G. Parks (2001), Observation of IMF and seasonal effects in the location of auroral substorm onset, *J. Geophys. Res.*, *106*, 5799–5810.

Lui, A. T. Y. (1984), Characteristics of the cross-tail current in the Earth's magnetotail, in *Magnetospheric Currents*, edited by T. A. Potemra, pp. 158–170, AGU, Washington, D. C., doi:10.1029/GM028p0158.

Lyatskaya, S., W. Lyatsky, and G. Khazanov (2014), Distinguishing high surf from volcanic long-period earthquakes, *Geophys. Res. Lett.*, *41*, 799–804, doi:10.1002/2013GL058954.

Lyon, J. G., J. A. Fedder, and C. M. Mobarry (2004), The Lyon-Fedder-Mobarry (LFM) global MHD magnetospheric simulation code, *J. Atmos. Sol. Terr. Phys.*, *66*(15–16), 1333–1350, doi:10.1016/j.jastp.2004.03.020.

Mansurov, S. M. (1969), New evidence of the relationship between magnetic field in space and on the Earth [English Translation], *Geomagn. Aeron.*, *9*, 768–773.

Merkin, V. G., and J. G. Lyon (2010), Effects of the low-latitude ionospheric boundary condition on the global magnetosphere, *J. Geophys. Res.*, *115*, A10202, doi:10.1029/2010JA015461.

Milan, S. E. (2015), Sun et lumière: Solar wind-magnetosphere coupling as deduced from ionospheric flows and polar auroras, in *Magnetospheric Plasma Physics: The Impact of Jim Dungey's Research, Astrophys. Space Sci. Proc.*, vol. 41, edited by D. Southwood, S. W. H. Cowley, and S. Mitton, pp. 33–64, Springer, Switzerland, doi:10.1007/978-3-319-18359-6.

Mozer, F. S., F. Bogott, M. C. Kelley, S. Schutz, and W. D. Gonzalez (1974), High-latitude electric fields and the three-dimensional interaction between the interplanetary and terrestrial magnetic fields, *J. Geophys. Res.*, *79*(1), 56–63, doi:10.1029/JA079i001p00056.

Østgaard, N., and K. M. Laundal (2012), Auroral asymmetries in the conjugate hemispheres and interhemispheric currents, in *Auroral Phenomenology and Magnetospheric Processes: Earth And Other Planets, Geophys. Monogr. Ser.*, edited by A. Keiling et al., pp. 99–111, AGU, Washington, D. C., doi:10.1029/2011GM001190.

Østgaard, N., S. B. Mende, H. U. Frey, T. J. Immel, L. A. Frank, J. B. Sigwarth, and T. J. Stubbs (2004), Interplanetary magnetic field control of the location of substorm onset and auroral features in the conjugate hemispheres, *J. Geophys. Res.*, *109*, A07204, doi:10.1029/2003JA010370.

Østgaard, N., S. B. Mende, H. U. Frey, J. B. Sigwarth, A. Åsnes, and J. M. Weygand (2007), Auroral conjugacy studies based on global imaging, *J. Atmos. Sol. Terr. Phys.*, *69*, 249–255, doi:10.1016/j.jastp.2006.05.026.

Østgaard, N., K. M. Laundal, L. Juusola, A. Åsnes, S. E. Håland, and J. M. Weygand (2011a), Interhemispherical asymmetry of substorm onset locations and the interplanetary magnetic field, *Geophys. Res. Lett.*, *38*, L08104, doi:10.1029/2011GL046767.

Østgaard, N., B. K. Humberset, and K. M. Laundal (2011b), Evolution of auroral asymmetries in the conjugate hemispheres during two substorms, *Geophys. Res. Lett.*, *38*, L03101, doi:10.1029/2010GL046057.

Ouellette, J. E., B. N. Rogers, M. Wiltberger, and J. G. Lyon (2010), Magnetic reconnection at the dayside magnetopause in global Lyon-Fedder-Mobarry simulations, *J. Geophys. Res.*, *115*, A08222, doi:10.1029/2009JA014886.

Park, K. S., T. Ogino, and R. J. Walker (2006), On the importance of antiparallel reconnection when the dipole tilt and IMF B_y are nonzero, *J. Geophys. Res.*, *111*, A05202, doi:10.1029/2004JA010972.

Parker, E. N. (1996), The alternative paradigm for magnetospheric physics, *J. Geophys. Res.*, *101*, 10,587–10,625, doi:10.1029/95JA02866.

Parker, E. N. (2007), *Conversations on Electric and Magnetic Fields in the Cosmos*, Princeton Univ. Press, Princeton, N. J.

Petrukovich, A. A. (2011), Origins of plasma sheet B_y, *J. Geophys. Res.*, *116*, A07217, doi:10.1029/2010JA016386.

Petrukovich, A. A., W. Baumjohann, R. Nakamura, A. Runov, and A. Balogh (2005), Cluster vision of the magnetotail current sheet on a macroscale, *J. Geophys. Res.*, *110*, A06204, doi:10.1029/2004JA010825.

Pitkänen, T., M. Hamrin, P. Norqvist, T. Karlsson, H. Nilsson, A. Kullen, S. M. Imber, and S. E. Milan (2015), Azimuthal velocity shear within an earthward fast flow further evidence for magnetotail untwisting?, *Ann. Geophys.*, *33*, 245–255, doi:10.5194/angeo-33-245-2015.

Provan, G., M. Lester, S. Mende, and S. E. Milan (2009), Statistical study of high-latitude plasma flow during magnetospheric substorms, *Ann. Geophys.*, *22*, 3607–3624, doi:10.5194/angeo-22-3607-2004.

Reistad, J. P., N. Østgaard, K. M. Laundal, and K. Oksavik (2013), On the non-conjugacy of nightside aurora and their generator mechanisms, *J. Geophys. Res. Space Physics*, *118*, 3394–3406, doi:10.1002/jgra.50300.

Reistad, J. P., N. Østgaard, K. M. Laundal, S. Haaland, P. Tenfjord, K. Snekvik, and K. Oksavik (2014), Intensity asymmetries in the dusk sector of the poleward auroral oval due to IMF B_x, *J. Geophys. Res. Space Physics*, *119*, 9497–9507, doi:10.1002/2014JA020216.

Ridley, A. J., T. I. Gombosi, I. V. Sokolov, G. Tóth, and D. T. Welling (2010), Numerical considerations in simulating the global magnetosphere, *Ann. Geophys.*, *28*(8), 1589–1614, doi:10.5194/angeo-28-1589-2010.

Ruohoniemi, J., S. Shepherd, and R. Greenwald (2002), The response of the high-latitude ionosphere to IMF variations, *J. Atmos. Sol. Terr. Phys.*, *64*, 159–171, doi:10.1016/S1364-6826(01)00081-5.

Russel, C. (1972), The configuration of the magnetosphere, in *Critical Problems of Magnetospheric Physics*, edited by E. R. Dyer, pp. 1–16, IUSTP Secretariat, Washington, D. C.

Song, P., and V. M. Vasyliūnas (2010), Aspects of global magnetospheric processes, *Chin. J. Space Sci.*, *30*(4), 289–311.

Song, P., and V. M. Vasyliunas (2011), How is the ionosphere driven by the magnetosphere?, in *General Assembly and Scientific Symposium, 2011 XXXth URSI*, pp. 1–4, IEEE., doi:10.1109/URSIGASS.2011.6050873, 13–20 Aug.

Stenbaek-Nielsen, H. C., and A. Otto (1997), Conjugate auroras and the interplanetary magnetic field, *J. Geophys. Res.*, *102*(A2), 2223–2232, doi:10.1029/96JA03563.

Strangeway, R. J. (2012), The relationship between magnetospheric processes and auroral field-aligned current morphology, in *Auroral Phenomenology and Magnetospheric Processes: Earth And Other Planets*, edited by A. Keiling et al., pp. 355–364, AGU, Washington, D. C., doi:10.1029/2012GM001211.

Svalgaard, L. (1968), Sector structure of the interplanetary magnetic field and daily variation of the geomagnetic field at high latitudes, *Geophys. Pap. R-16*, Danish Meteorol. Inst.Copenhagen, Denmark.

Tsyganenko, N. A. (1998), Modeling of twisted/warped magnetospheric configurations using the general deformation method, *J. Geophys. Res.*, *103*, 23,551–23,563, doi:10.1029/98JA02292.

AGU Journal of Geophysical Research: Space Physics 10.1002/2015JA021579

Tu, J., P. Song, and V. M. Vasyliunas (2014), Inductive-dynamic magnetosphere-ionosphere coupling via MHD waves, *J. Geophys. Res. Space Physics*, *119*, 530–547, doi:10.1002/2013JA018982.

Vasyliunas, V. M. (2012), The physical basis of ionospheric electrodynamics, *Ann. Geophys.*, *30*(2), 357–369, doi:10.5194/angeo-30-357-2012.

Walker, R. J., R. L. Richard, T. Ogino, and M. Ashour-Abdalla (1999), The response of the magnetotail to changes in the IMF orientation: The magnetotail's long memory, *Phys. Chem. Earth Part C*, *24*(1–3), 221–227, doi:10.1016/S1464-1917(98)00032-4.

Walsh, A. P., et al. (2014), Dawn-dusk asymmetries in the coupled solar wind-magnetosphere-ionosphere system: A review, *Ann. Geophys.*, *32*, 705–737, doi:10.5194/angeo-32-705-2014.

Waters, C. L., B. J. Anderson, and K. Liou (2001), Estimation of global field aligned currents using the Iridium System magnetometer data, *Geophys. Res. Lett.*, *28*(11), 2165–2168, doi:10.1029/2000GL012725.

Wilken, B., C. K. Goertz, D. N. Baker, P. R. Higbie, and T. A. Fritz (1982), The SSC on July 29, 1977 and its propagation within the magnetosphere, *J. Geophys. Res.*, *87*(A8), 5901–5910, doi:10.1029/JA087iA08p05901.

Wing, S., P. T. Newell, D. G. Sibeck, and K. B. Baker (1995), A large statistical study of the entry of interplanetary magnetic field Y-component into the magnetosphere, *Geophys. Res. Lett.*, *22*(16), 2083–2086, doi:10.1029/95GL02261.

Wing, S., D. G. Sibeck, M. Wiltberger, and H. Singer (2002), Geosynchronous magnetic field temporal response to solar wind and IMF variations, *J. Geophys. Res.*, *107*(A8), 1222, doi:10.1029/2001JA009156.

Paper IV

Dynamic effects of restoring footpoint symmetry on closed magnetic field-lines

J. P. Reistad, N. Østgaard, P. Tenfjord, K. M. Laundal, K. Snekvik, S. Haaland, S. E. Milan, K. Oksavik, H. U. Frey, and A. Grocott

Journal of Geophysical Research, Vol. 121, doi:10.1002/2015JA022058 (2016)

IV

AGU PUBLICATIONS

JGR

Journal of Geophysical Research: Space Physics

RESEARCH ARTICLE

10.1002/2015JA022058

Dynamic effects of restoring foot point symmetry on closed magnetic field lines

J. P. Reistad[1], N. Østgaard[1], P. Tenford[1], K. M. Laundal[1], K. Snekvik[1], S. Haaland[1,2], S. E. Milan[1,3], K. Oksavik[1,4], H. U. Frey[5], and A. Grocott[6]

[1]Birkeland Centre for Space Science, Department of Physics and Technology, University of Bergen, Bergen, Norway, [2]Max Planck Institute for Solar System Research, Lindau, Germany, [3]Department of Physics and Astronomy, University of Leicester, Leicester, UK, [4]University Centre in Svalbard, Longyearbyen, Norway, [5]Space Sciences Laboratory, University of California, Berkeley, California, USA, [6]Department of Physics, Lancaster University, Lancaster, UK

Key Points:
- Observed asymmetric convection and FAC on closed field lines consistent with effect of asymmetric stress release during IMF By conditions
- The event experiences a large (3 h) MLT displacement of the nightside aurora between the two hemispheres
- The restoring symmetry process can be an important mechanism in creating asymmetric FACs and convection on closed field lines

Correspondence to:
J. P. Reistad,
jone.reistad@uib.no

Citation:
Reistad, J. P., N. Østgaard, P. Tenford, K. M. Laundal, K. Snekvik, S. Haaland, S. E. Milan, K. Oksavik, H. U. Frey, and A. Grocott (2016), Dynamic effects of restoring foot point symmetry on closed magnetic field lines, *J. Geophys. Res. Space Physics*, *121*, doi:10.1002/2015JA022058.

Received 20 OCT 2015
Accepted 21 MAR 2016
Accepted article online 28 MAR 2016

Abstract Here we present an event where simultaneous global imaging of the aurora from both hemispheres reveals a large longitudinal shift of the nightside aurora of about 3 h, being the largest relative shift reported on from conjugate auroral imaging. This is interpreted as evidence of closed field lines having very asymmetric foot points associated with the persistent positive *y* component of the interplanetary magnetic field before and during the event. At the same time, the Super Dual Auroral Radar Network observes the ionospheric nightside convection throat region in both hemispheres. The radar data indicate faster convection toward the dayside in the dusk cell in the Southern Hemisphere compared to its conjugate region. We interpret this as a signature of a process acting to restore symmetry of the displaced closed magnetic field lines resulting in flux tubes moving faster along the banana cell than the conjugate orange cell. The event is analyzed with emphasis on Birkeland currents (BC) associated with this restoring process, as recently described by Tenford et al. (2015). Using data from the Active Magnetosphere and Planetary Electrodynamics Response Experiment during the same conditions as the presented event, the large-scale BC pattern associated with the event is presented. It shows the expected influence of the process of restoring symmetry on BCs. We therefore suggest that these observations should be recognized as being a result of the dynamic effects of restoring foot point symmetry on closed field lines in the nightside.

1. Introduction

When the interplanetary magnetic field (IMF) interacts with the Earth's magnetic field, a dawn-dusk component in the IMF will affect the two hemispheres differently in a number of ways. The ionospheric convection pattern is commonly attributed to represent the footprints of this interaction and has been studied in great detail in both hemispheres [*Heppner and Maynard*, 1987; *Pettigrew et al.*, 2010; *Cousins and Shepherd*, 2010; *Förster and Haaland*, 2015]. It is known that the presence of IMF B_y alters the usual two-cell convection pattern into a crescent "banana" and a round "orange" cell with locations approximately mirrored across the noon-midnight meridian in the two hemispheres. However, an outstanding challenge when comparing the two hemispheres is to resolve the true conjugate regions. Simultaneous global auroral imaging from both hemispheres has proven to be able to identify such connected regions as the aurora serves to "light up" the footprints of magnetospheric processes. A highly distinguishable feature in the nightside aurora, the substorm onset, has been studied in this way. Its hemispheric relative displacement in longitude has been shown to be largely controlled by IMF B_y [*Liou and Newell*, 2010; *Østgaard et al.*, 2005, 2011b].

It has been shown by theory [*Cowley*, 1981; *Khurana et al.*, 1996], observations [*Cowley and Hughes*, 1983; *Lui*, 1984; *Wing et al.*, 1995], and modeling [*Kullen and Janhunen*, 2004; *Guo et al.*, 2014; *Tenford et al.*, 2015] that for nonzero IMF B_y a B_y component in the same direction as IMF B_y is induced on closed field lines. Consistent with this, we observe asymmetric foot points. Although there are other processes leading to B_y in the closed magnetosphere, such as dipole tilt-related effects, B_y induced from IMF B_y is considered as the primary contributor in the plasma sheet [*Petrukovich*, 2011].

IMF B_y-related changes in the B_y component in the closed magnetosphere is well understood and explained by considering the forces acting on the magnetosphere due to IMF interacting with the terrestrial field [*Cowley*, 1981; *Guo et al.*, 2014; *Tenford et al.*, 2015; *Østgaard et al.*, 2015]. The study by *Tenford et al.* [2015]

AGU Journal of Geophysical Research: Space Physics 10.1002/2015JA022058

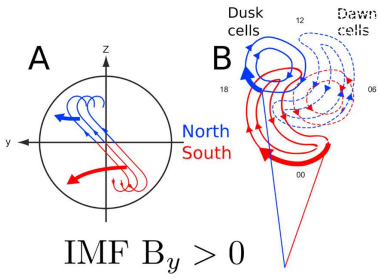

Figure 1. (a) View from deep in the magnetotail toward the Earth of magnetic field lines with displaced foot points due to IMF B_y positive. Arrows indicate the plasma flow toward the dayside in the dusk convection cells. (b) A view of how a magnetic field line in the dusk cells (seen in Figure 1a) is connected to the two hemispheres. The perspective is from above the northern magnetic pole looking through the Earth. The small numbers refer to MLT coordinates. Blue represent the Northern Hemisphere, and red represents the Southern Hemisphere. The dawn convection cells are also shown (dashed) but not with any connecting field line (after Figure 3 of *Grocott et al.* [2005]).

emphasized that the commonly used terminology "IMF B_y penetration" is misleading in this regard, as the changes in the B_y field in the magnetosphere is not a simple fraction of the IMF B_y nor can it be regarded as a vacuum superposition of external (IMF) field contributions. Using the Lyon-Fedder-Mobarry global magneto-hydrodynamic (MHD) model, they showed that B_y is induced in the closed magnetosphere as a result of the asymmetric loading of magnetic flux in the lobes during IMF B_y conditions. This gives dawn-dusk asymmetric pressure in the two lobes. The plasma convection in the two lobes will be opposite and a B_y component on closed field lines will be induced. This asymmetric forcing between the hemispheres also causes the foot points to move relatively between the hemispheres, introducing a longitudinal displacement of conjugate points from a quiet time position. Throughout the manuscript we will use the same terminology as *Tenford et al.* [2015] for the appearance of B_y in the magnetosphere due to IMF B_y, namely, *induced* B_y.

When illustrating the Earth's magnetic field lines with an induced B_y, as seen in Figure 1a, they will have asymmetric foot points in the ionosphere [*Liou and Newell*, 2010; *Østgaard et al.*, 2011b; *Motoba et al.*, 2010]. The topic of this paper is the dynamic effects when these field lines gradually relax to a more symmetric situation as they move closer to Earth and toward dawn or dusk.

The dynamics of magnetic field lines on the nightside having an induced B_y have been studied earlier with emphasis on the observed plasma convection in the magnetosphere and ionosphere. Although first suggested by *Nishida et al.* [1998], *Grocott et al.* [2004] were the first to observe the fast east/west convection in the nightside ionosphere on field lines supposedly having asymmetric foot points. What *Grocott et al.* [2004] referred to as fast flows was ~1000 m/s plasma convection in the midnight sector typically extending 2–3 h of magnetic local time (MLT) and its east/west direction determined by the sign of IMF B_y and the hemisphere. It was later shown that these plasma flow signatures, indeed, were simultaneously present in the magnetosphere and ionosphere and oppositely directed in the two hemispheres [*Grocott et al.*, 2007]. This has later been confirmed by *Pitkänen et al.* [2015], also looking at simultaneous magnetospheric and ionospheric convection in both hemispheres, indicating that restoring foot point symmetry is a fundamental process throughout the Dungey cycle, much like any physical system trying to restore a minimum energy configuration. It should be noted that the plasma flows seen by Grocott et al. were mostly occurring during northward IMF [*Grocott et al.*, 2008]. However, this mechanism should still work for southward IMF as the tail will still be asymmetrically forced by IMF B_y. One effect of restoring foot point symmetry is schematically illustrated in Figure 1 (after Figure 3 of *Grocott et al.* [2005]) during positive IMF B_y conditions. Figure 1a shows three field lines on the nightside with asymmetric foot points, seen from the magnetotail, where blue color indicates the Northern Hemispheric end, and red is used for the Southern Hemispheric end. The field lines in Figure 1a are assumed to convect around the Earth in the dusk cell (since our event is focusing on the dusk cell). Hence, their magnetospheric and ionospheric velocities (large arrows in Figures 1a and 1b) point in that direction. Since the foot points of the field line are displaced in longitude on the nightside, the Southern Hemispheric end needs to move faster in the westward direction in the dusk cell to catch up with the Northern Hemisphere

AGU Journal of Geophysical Research: Space Physics 10.1002/2015JA022058

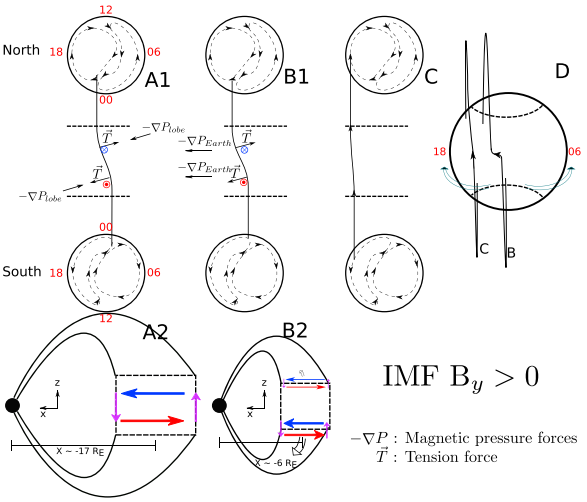

Figure 2. (a–c) Evolution of a closed field line with asymmetric foot points in the dusk convection cells during IMF B_y positive conditions. Figures 2a1, 2b1, and 2c show how a field line with asymmetric foot points connects to the dusk convection cells in the two hemispheres at three different times. (a2 and b2) The associated current systems with colored arrows, seen from the dusk side. Figure 2a1: In the midtail region the asymmetric pressure forces due to IMF B_y (P_{lobe}) and the magnetic tension forces (T) on the field line balance. Currents close locally as indicated in Figure 2a2. Figure 2b1: At a later stage the field line moves earthward and is affected by the gradient of the total pressure surrounding the Earth (plasma and magnetic field, P_{Earth}). Now the forces do not balance. In the Southern Hemisphere the indicated forces point in the same direction. Hence, most of the stress is transmitted into this hemisphere, and the southern foot point will catch up with the northern counterpart to restore symmetry, as seen in Figure 2c. (d) The situation in Figures 2b and 2c viewed from the tail.

as the field line convects toward the dayside. This is indicated in the ionospheric view in Figure 1b. Here one of the field lines from Figure 1a is shown to have asymmetric foot points and also different westward convection speeds reflected by the different lengths of the thick arrows. In the dawn cell the situation is opposite (not shown here). These asymmetric convection speeds can be explained by considering the forces acting on the field line, shown toward the end of this section when we introduce Figure 2.

The magnetospheric geometry for nonzero IMF B_y has been widely investigated. *Stenbaek-Nielsen and Otto* [1997] suggested that the modified magnetic field geometry due to induced B_y in the nightside (Figure 1) should give rise to interhemispheric currents due to the finite extent of the B_y component in the x direction (toward the Sun) in the magnetotail, explaining their observations of nonconjugate aurora. However, no explanation on how the currents could propagate all the way to the ionosphere was given. More recent observations of nonconjugate aurora [*Østgaard et al.*, 2011a; *Reistad et al.*, 2013] have used similar arguments to suggest that the field configuration due to the induced B_y could be responsible for the observed asymmetries. However, the relation of such observations to the process of restoring symmetry was only recently proposed [*Tenfjord et al.*, 2015].

The view presented by *Grocott et al.* [2005] (our Figure 1) gives a conceptual framework for understanding the plasma convection observations, both from space and from the ground. However, its relation to field-aligned currents, also known as Birkeland currents (BCs), has not been treated in a unified way until recently [*Tenfjord et al.*, 2015]. The present study largely builds on this advancement in understanding. We present an event with a large longitudinal displacement of foot points and apply the understanding of this configuration to explain the observed convection, aurora, and associated BCs in the framework of restoring foot point symmetry.

AGU Journal of Geophysical Research: Space Physics 10.1002/2015JA022058

Before we present our event we give a description of what we will refer to as the process of restoring symmetry, which takes place when a field line with asymmetric foot points relaxes gradually to a more symmetric configuration as it moves toward dusk (or dawn). Figure 2 (after Figure 6 of *Tenfjord et al.* [2015]) shows a simplified model of the evolution (and related currents) of a field line on the nightside having asymmetric foot points when considering the magnetospheric forces acting on it for the IMF B_y positive case. As pointed out by *Tenfjord et al.* [2015], the induced B_y in the tail is due to the buildup of an asymmetric magnetic pressure distribution in the two lobes as the tension forces on the newly reconnected field lines on the dayside act in opposite directions in the two hemispheres. For southward (but B_y dominated) IMF, flux is added asymmetrically, and for northward IMF, flux is rearranged asymmetrically. In both cases one will get an asymmetric magnetic pressure distribution in the two lobes which cause asymmetric plasma convection within the magnetosphere and affect also the closed field lines differently in the two hemispheres. The shear plasma flows between the northern and the southern halves of the magnetotail will eventually also displace the foot points of the field lines [*Liou and Newell*, 2010; *Guo et al.*, 2014; *Tenfjord et al.*, 2015].

The asymmetric pressure forces ($-\nabla P_{\mathrm{lobe}}$ in Figure 2a1) act on the field line in opposite directions in the two hemispheres creating asymmetric foot points. Due to this, there will be an oppositely directed tension force, $\vec{T}$, acting to balance the $-\nabla P_{\mathrm{lobe}}$ force. The illustrated field line in Figure 2a1 is a closed field line in the midtail convecting toward the Earth and returning in the dusk cell (same situation as in Figure 1). How the field line connects to the banana and the orange cell in opposite hemispheres is also indicated. Associated with this geometry, Ampère's law requires a pair of currents flowing in the x direction as indicated by red and blue arrows in and out of the plane in the middle of Figure 2a1. In Figure 2a2 the field line is seen from the side. The box in the equatorial region indicates an idealized extent of the B_y component in the x direction, meaning that B_y is zero on either side. At these edges, $\nabla \times \vec{B}$ implies a current in the z direction as indicated by the purple arrows. In this case, when the forces balance, the currents close locally, and no BCs into the ionosphere are present.

As the field line convects closer to the Earth it will experience the total pressure from Earth, $-\nabla P_{\mathrm{Earth}}$, and be less affected by $-\nabla P_{\mathrm{lobe}}$, see Figure 2b1. At this location $-\nabla P_{\mathrm{Earth}}$ has a component toward dusk along the entire field line since we have chosen to consider a field line returning in the dusk cell. In this situation the forces do not balance but are highly unbalanced as the forces are added in one hemisphere and subtracted in the other. The stress stored in the field will now be transported primarily toward the Southern Hemisphere where the forces are added. We emphasize that these considerations are based on an MHD description of how the system responds to external forcing.

Seen from the side, Figure 2b2 illustrates that this situation represents Alfvèn wavefronts carrying a pair of BCs that are launched primarily into the Southern Hemisphere. These waves act to restore foot point symmetry along the equatorward part of the banana cell as the stress is being released. Due to this, the BCs transmitted (by the waves) to the Southern Hemisphere are expected to be stronger than in the other hemisphere. This illustrates a situation where asymmetric (between hemispheres) BCs can be generated. The net effect is the same as suggested by *Stenbaek-Nielsen and Otto* [1997]. However, this modified picture puts further constraints on the location of where the asymmetric BCs should be located (dawn or dusk cell). Figure 2c illustrates a later stage when the field line has relaxed to a more symmetric configuration. Figure 2d illustrates the transition from step B to C as viewed from the tail.

To summarize, when we refer to the process of restoring symmetry, we mean the following. (1) The release of magnetic stress from the magnetosphere to the hemisphere connected to the banana cell that will gradually restore the asymmetric field lines as they convect duskward or dawnward. (2) This is consistent with faster azimuthal ionospheric plasma flow along the banana cell than along the conjugate orange cell. (3) The asymmetric release of magnetic stress also leads to asymmetric Birkeland currents into the conjugate hemispheres. The term "untwisting process/phenomenon/hypothesis" that has been used in the literature [*Pitkänen et al.*, 2015] includes only point 2 of this process. To avoid misunderstanding, we will therefore use the term 'restoring symmetry process' throughout the paper.

In the following we present a case where simultaneous global auroral imaging reveals a large longitudinal displacement of the nightside aurora indicating the asymmetric foot point configuration discussed above. Simultaneous conjugate ionospheric plasma flow measurements in the nightside convection throat region are also presented, allowing us to identify the extent of the convection cells in both hemispheres and compare with the auroral display. As no simultaneous BC measurements were available during the event, we

AGU Journal of Geophysical Research: Space Physics 10.1002/2015JA022058

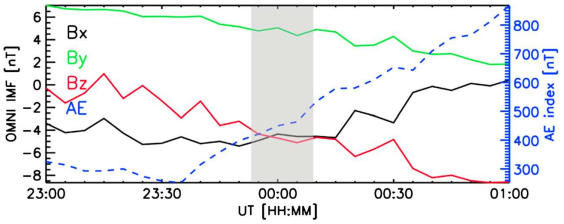

Figure 3. IMF B_x, B_y, and B_z (solid) and the *AE* geomagnetic activity index (dashed) during the event on 18–19 May 2001. The shaded grey region indicates interval of simultaneous observations presented in Figure 5.

investigate average BC maps obtained during similar conditions as the event to explore the impact of the process of restoring symmetry on BCs in the two hemispheres and compare with the model predictions from Figure 2. The emphasis will be on investigating how the observations fit our understanding of the large-scale electrodynamics in terms of the restoring foot point symmetry process.

2. Instrumentation

2.1. Imaging Data

The auroral images from the Northern Hemisphere are obtained by the far ultraviolet (FUV) Wideband Imaging Camera (WIC) [*Mende et al.*, 2000] on board the IMAGE (Imager for Magnetopause-to-Aurora Global Exploration) spacecraft [*Burch*, 2000]. The WIC camera is sensitive to the UV range 140–190 nm, including the Lyman-Birge-Hopfield band (molecular nitrogen) and a few atomic nitrogen lines. The auroral emissions at these wavelengths are mainly due to precipitating electrons [*Frey et al.*, 2003]. The images are presented in modified apex coordinates (magnetic latitude (MLAT)/MLT) with reference height 130 km [*Richmond*, 1995]. In order to get an image only containing the aurora, emissions from dayglow as well as a constant noise level were subtracted.

The auroral images from the Southern Hemisphere are taken from the Polar spacecraft [*Acuña et al.*, 1995] VIS (Visible Imaging System) Earth camera [*Frank et al.*, 1995; *Frank and Sigwarth*, 2003]. The response in this camera is mostly from the OI line at 130.4 nm. The VIS Earth images are also presented in the same apex/MLT coordinates. As the auroral zone in the Southern Hemisphere was dark during the event, no dayglow removal was needed.

2.2. Ionospheric Plasma Flow Measurements

Measurements of the ionospheric plasma flow velocity are provided by two HF coherent scatter radars part of the Super Dual Auroral Radar Network (SuperDARN) [*Greenwald et al.*, 1995; *Chisham et al.*, 2007]. SuperDARN radars operate by transmitting radio signals that refract in the ionosphere and backscatter from decameter-scale, magnetic field-aligned irregularities in the electron density. Backscattered signals from the *F* region ionosphere experience a Doppler shift that is proportional to the line-of-sight (LOS) component of the plasma drift velocity. The two radars used in this study are the Stokkseyri radar, located in Iceland at geographic coordinates 63.86°N, 22.02°W, and with a bore site direction of 59.0°W, and the Syowa-East radar, located in Antarctica at 69.0°S, 39.58°E, and bore site 106.5°E. During the interval of interest, both radars were operating in a common mode in which they scan through 16 beams of separation 3.24°, with a total scan time of 2 min. Each beam is divided into 75 range gates of length 45 km, and so in each full scan the radars cover 52° in azimuth and over 3000 km in range.

3. Observations

In this section we present simultaneous auroral images and ionospheric plasma flow measurements around the nightside convection throat region in both hemispheres of an event starting on 18 May 2001.

IMF and geomagnetic activity around the event are presented in Figure 3. The interval of observations shown in this section is highlighted with grey shade. The IMF data are from the 5 min OMNI data product from NASA's Space Physics Data Facility [*King and Papitashvili*, 2005] and are represented in the geocentric solar magnetic

AGU Journal of Geophysical Research: Space Physics 10.1002/2015JA022058

coordinate system. These data represent the IMF conditions at the Earth's bow shock nose. As the IMF shows little fluctuations during our event, any minor errors introduced by the timeshift is not important for our interpretation. Embedded in the OMNI data product is the *AE* index (provided by the World Data Center for Geomagnetism, Kyoto), also with 5 min time resolution. Figure 3 shows that the IMF B_z component declines slowly from ~0 to −5 nT during the hour preceding the simultaneous ionospheric convection and imaging measurements 23:53–00:09 UT. During this time interval the IMF B_x and B_y components are stable with values around −5 and +5 nT, respectively. The *AE* index is also shown in the same plot, indicating moderately disturbed geomagnetic conditions (~450 nT). It should be noted that the longitudinal displacement of foot point locations, ΔMLT, is expected to depend on geomagnetic activity. In the statistical study of substorm onset locations in the two hemispheres by *Østgaard et al.* [2011b], the average hemispheric difference in MLT (~ΔMLT) as a function of the IMF clock angle was found to be larger when only events with |IMF| > 5 nT were considered. This is expected as flux is added asymmetrically more efficiently for large values of IMF for the same clock angle. Although a more quiet event would be desirable to remove other disturbances, this event is unique in terms of data coverage to investigate the process of restoring symmetry and therefore represents a very interesting case. The 23:53–00:09 UT interval was chosen because of good radar coverage of the nightside convection throat region in the dusk cell.

3.1. Simultaneous Imaging of the Two Auroral Ovals

On 18 May 2001 the IMAGE FUV-WIC camera observed the Aurora Borealis from apogee, while the Polar VIS Earth camera simultaneously observed the Aurora Australis from perigee. This favorable configuration allowed simultaneous imaging of the auroral oval in both hemispheres.

A pair of simultaneous images plotted in the MLAT/MLT grid are seen in Figures 4a (Northern Hemisphere at 23:53:07 UT) and 4b (Southern Hemisphere at 23:52:55 UT). Note that the intensity scaling is chosen to best reflect the auroral variability within each hemisphere separately. The intensities cannot be directly compared between hemispheres due to the different instrumentation. Our interpretation is therefore limited to how relative differences within the images compare between the two hemispheres. The solid black curve in the Northern Hemisphere that is crossing midnight at around 70° MLAT is the contour of 90° solar zenith angle. It indicates that most of the aurora in the Northern Hemisphere is directly exposed to sunlight. However, as mentioned in section 2, the dayglow-related emissions have been removed. A distinct large-scale feature in the dusk side oval can be identified in both hemispheres, highlighted by the dashed line in Figures 4a and 4b. One can see that this feature is heavily displaced in MLT between the two hemispheres. The Southern Hemisphere part extends toward midnight, while it only extends toward 21 MLT in the Northern Hemisphere.

A correlation analysis is performed to more objectively identify the shift between the two hemispheres for the simultaneous image pairs. The images are first mapped to a rectangular grid. The VIS image (south) is held fixed, considering only the region from 18–03 MLT. The same region is extracted from the mapped WIC image including a variable shift in longitude (MLT). At 0.1 h steps, this MLT shift is varied from 0 to 4 h. Note that we use $\Delta MLT = MLT_{south} - MLT_{north}$, resulting in a positive value of ΔMLT for this case. Then ΔMLT is identified as the relative shift at which the correlation between the extracted regions peaks. We use the linear correlation between the two vectors representing the fixed VIS image and the varying WIC image. This procedure is shown in Figures 4c and 4d. Here the same images as in the polar plots in Figures 4a and 4b are shown before and after the MLT shift is applied. This analysis will produce a value of ΔMLT for each simultaneous image pair. In Figure 4e we show a time series plot of ΔMLT. We have distinguished between good (black diamonds) and uncertain (grey diamonds) fits. This evaluation is based on visual inspection of the output for each image pair. Generally, the method works better when the aurora has similar structures in the two hemispheres. During the time interval when simultaneous ionospheric convection measurements were available in the conjugate regions, we derive a ΔMLT as large as ~3 h. To our knowledge, this is by far the largest MLT shift of conjugate foot points that has been reported based on conjugate auroral observations.

We also note that ΔMLT (Figure 4e) follows a similar trend as the IMF B_y value (Figure 3), namely, that ΔMLT is decaying as IMF B_y decays. This is expected when the loading become more symmetric and consistent with statistical studies of auroral displacement and IMF B_y [*Liou et al.*, 2001; *Wang et al.*, 2007; *Liou and Newell*, 2010; *Østgaard et al.*, 2011b]. We also note that there is a broad peak of ΔMLT from about 2350 to 0030 UT of about 1 h more than the general decrease of IMF B_y implies. Although we believe that the large displacement seen in this event is due to the combined effect of positive IMF B_y and positive dipole tilt [*Liou and Newell*, 2010], we have no explanation for this broad peak. We emphasize that the restoring symmetry process occurs as closed

AGU Journal of Geophysical Research: Space Physics 10.1002/2015JA022058

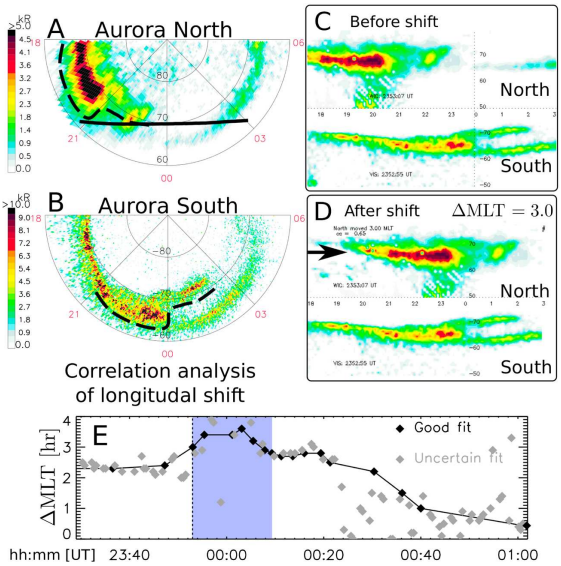

Figure 4. (a and b) Simultaneous images from WIC in the Northern Hemisphere and VIS in the Southern Hemisphere on a polar MLAT/MLT grid. (c) The same images projected on a rectangular MLAT/MLT grid before a longitudinal shift is applied. (d) Same as Figure 4c but now the Northern Hemisphere image has been shifted 3 h in the direction indicated by the arrow. (e) Time series of the longitudinal shift of the aurora between the hemispheres derived from a correlation analysis. Black diamonds indicate an accurate determination. The vertical dashed line indicates the time of the image pair presented, and the blue shaded region indicate the time interval when conjugate convection from SuperDARN is analyzed in Figures 5 and 7.

field lines convect from the tail toward the dayside and foot point symmetry is restored (ΔMLT$\rightarrow$ 0 for that particular field line). This is different from the situation when ΔMLT$\rightarrow$ 0 on the nightside, which is related to the driving mechanism disappearing (IMF $B_y \rightarrow 0$). During a constant IMF B_y interval, as shown in this paper, ΔMLT should stay the same in the nightside region.

3.2. Simultaneous Ionospheric Convection and Hall Currents

Two of the SuperDARN radars were favorably located during this event to monitor the plasma flow near the nightside convection throat. The LOS plasma flow velocity is plotted on top of the auroral images for four instances in Figures 5a–5d, with toward velocities as red and away velocities as blue. Of special interest is the nightside convection throat, which in the framework of the restoring symmetry concept needs to be a conjugate feature. Upon successful identification in both hemispheres, this will provide an independent measure of ΔMLT. We identify the nightside convection throat as the transition from away to toward velocities in the radar data when the LOS direction is in the east/west direction and echoes originate from closed field lines.

In the Southern Hemisphere, the Syowa East radar observed the nightside convection throat. The radar was located around magnetic midnight and pointing in a magnetic southeast direction. In Figure 5 the reversal is seen clearly at 23:53 UT around 02 MLT (Figure 5a, bottom). Here the transition between toward and away plasma flow occurs along a distance of only ~200 km in the LOS direction. There is also a small uncertainty regarding the actual location of SuperDARN echoes due to mapping errors [e.g., *Yeoman et al.*, 2001, 2008; *Chisham et al.*, 2008]. These studies found the mapping error at distances similar to those considered here (~1000 km and less) to be typically less than 30 km, which is smaller than one radar range gate (45 km). Hence, we claim that the Southern Hemisphere convection throat region at 23:53 UT is accurately determined to be

AGU Journal of Geophysical Research: Space Physics 10.1002/2015JA022058

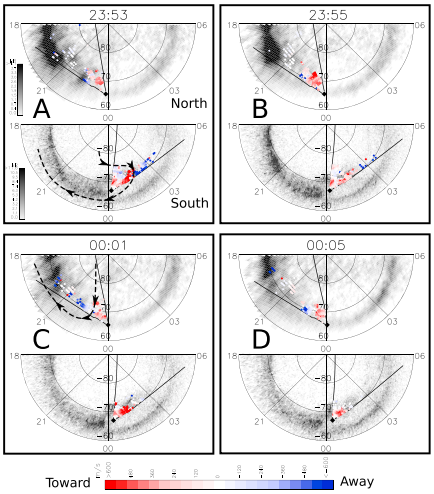

Figure 5. (A-D) SuperDARN line-of-sight velocities around the nightside reversal region plotted on top of the simultaneous conjugate auroral images at four instances during the event. Plasma flows toward the radar are shown in red; plasma flows away are shown as blue. Based on these radar data, the likely extent of the dusk convection cells is drawn with dashed lines in both hemispheres. One can see that the nightside convection throat is shifted 3.2 ± 0.6 h in MLT between the hemispheres, consistent with the auroral observations.

02 ± 0.1 MLT at 70° MLAT. We have indicated the shape of the extended dusk cell as the thick dashed curve in Figure 5a (bottom). In the later image pairs shown in Figures 5b–5d, the Southern Hemisphere convection throat is not captured as accurately due to the decreasing number of away echoes. But since the plasma flows remain westward, it indicates that 02 MLT is the minimum dawnward extent of the dusk cell.

The Stokkseyri radar in the Northern Hemisphere was located at magnetic midnight and pointing in a magnetic northwest direction. Its field of view and location are indicated by the black lines originating from the black diamond in the Northern Hemisphere plots in Figures 5a–5d (top). In the Northern Hemisphere, the nightside convection throat region is best captured at 00:01 UT, see Figure 5c (top). Here the equatorward three beams indicate a transition from plasma flows away from the radar (blue) at 22.3 MLT, through a region of small LOS magnitudes, indicating the plasma flow is primarily perpendicular to the LOS direction, to plasma flows toward the radar at 23.3 MLT. Based on this, we have sketched a possible extent of the dusk convection cell at this instance, seen as the thick dashed line in Figure 5c. From these data, the nightside convection throat in the Northern Hemisphere is likely within 22.8 ± 0.5 MLT.

We present further evidence for the nightside convection throat location in the Northern Hemisphere in Figure 6. Here magnetic perturbations from ground magnetometers from the SuperMAG network [*Gjerloev*, 2012] are shown on a MLT/MLAT map at 00:01 UT. The perturbation vectors are rotated 90° clockwise to represent the ionospheric equivalent current. Due to the high conductivity from sunlight in this hemisphere, the magnetic perturbations are likely dominated by the ionospheric Hall current overhead [*Laundal et al.*, 2015] and are therefore antiparallel to the ionospheric convection. In the auroral region, (below 70° MLAT) a transition from eastward Hall currents (seen at the Greenland NAQ station at 22.4 MLT) to westward Hall currents (seen as far west as the Iceland LRV station at 0.0 MLT) is observed, corresponding to the two cell convection pattern. This transition is centered in the same MLT region as the SuperDARN data shown in Figure 5c, strongly suggesting that the signature we see in the radar data likely is the nightside convection throat region. The SuperMAG data show only minor variations in the region of interest during the time window presented in Figure 5, indicating that the convection throat remained around 23 MLT in the Northern Hemisphere.

AGU Journal of Geophysical Research: Space Physics 10.1002/2015JA022058

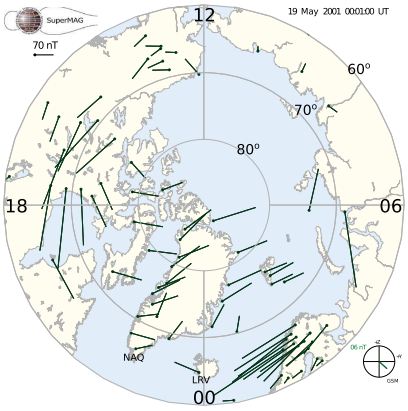

Figure 6. Ground magnetic perturbations from the SuperMAG network [*Gjerloev*, 2012] rotated 90° clockwise on a MLT/MLAT grid, representing the ionospheric Hall currents. The two-cell pattern in the Hall currents changes direction between Greenland and Iceland in agreement with our interpretation of the SuperDARN data.

When comparing the nightside convection throat location in the two hemispheres, we arrive at a very smilar longitudinal displacement between hemispheres as seen in the aurora in Figure 4. Due to the uncertainty in defining the transition region from the radar data, we conclude that the longitudinal displacement of the nightside convection throat is within 3.2 ± 0.6 h MLT during the interval presented.

In an effort to compare the velocities more directly in conjugate regions (westward of the nightside convection throat in the dusk cell), we present averaged convection velocities as a function of time in Figure 7. We consider only the return convection in the dusk cell in the vicinity of the nightside convection throat. For the Northern Hemisphere we consider echoes equatorward of 73° MLAT and closer than 21 MLT that indicate plasma flow away from the radar (blue). For these echoes, the LOS velocities are less than 10° off the apex westward direction. The average of these echoes is plotted as the blue line in Figure 7 with its corresponding standard error. The same is done in the Southern Hemisphere. Here we only consider the echoes that indicate convection toward the radar (red) in the five most equatorward beams at ranges equatorward of ~73° MLAT. In this way the LOS velocity are mostly within 20° of the apex westward direction, and the average velocity represents the westward convection on closed field lines. This is plotted in red with its corresponding standard error in Figure 7. A persistent stronger westward convection is seen in the Southern Hemisphere compared to its conjugate region in the Northern Hemisphere. This is in qualitative agreement with the expected behavior (from restoring symmetry process) in the dusk cell when ΔMLT is positive, as described in section 1.

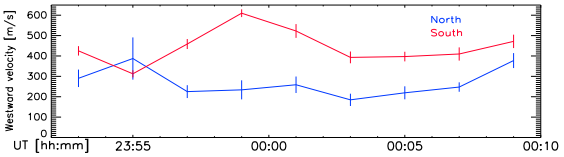

Figure 7. Averaged westward velocities in the dusk cell on closed field lines in the two hemispheres. A persistent stronger westward convection is seen in the Southern Hemisphere compared to its conjugate region, consistent with the restoring symmetry process.

AGU Journal of Geophysical Research: Space Physics 10.1002/2015JA022058

4. Discussion

4.1. Displaced Foot Points and Asymmetric Convection

From the direct comparison presented in Figure 7 we conclude that the westward ionospheric convection on closed field lines close to the nightside convection throat region in the dusk cell is stronger in the Southern Hemisphere compared to its conjugate region. This difference in ionospheric plasma flow velocity is expected for field lines with asymmetric foot points on the nightside with positive ΔMLT, and it is consistent with earlier observations [*Grocott et al.*, 2005, 2007; *Pitkänen et al.*, 2015]. It is also consistent with the concept of restoring symmetry described in section 1 and by *Tenford et al.* [2015], where the release of magnetic stress into one hemisphere causes plasma to convect faster on the equatorward part of the banana cell. It should be noted that the westward plasma flow values observed here are less intense than the fast plasma flows (~1000 m/s) reported by, e.g., *Grocott et al.* [2004]. However, individual echoes indicate velocities up to ~800 m/s in Figure 5. The discrepancies between northern and southern convection velocities are nevertheless attributed the restoring symmetry process as the sign of IMF B_y, the large ΔMLT, and the observed plasma flow direction are all consistent.

The earlier observations [*Grocott et al.*, 2005; *Pitkänen et al.*, 2015] focused on the fast plasma flows related to the restoring symmetry process, being on opposite ionospheric convection cells in the two hemispheres. Consequently, they did not focus on the plasma flow at its conjugate location as we do in this paper. Hence, identification of a longitudinal displacement of conjugate points is uncertain and difficult in their cases, making it less clear that their observed fast convection was really asymmetric at its conjugate location. However, in our case we also have simultaneous conjugate imaging in both hemispheres. Our firmly established foot point asymmetry together with the observed hemispheric difference in convection in conjugate regions demonstrate that conjugate regions are affected differently, as expected from the influence of the restoring symmetry process. We also note that this is to our knowledge the largest value of ΔMLT reported from conjugate auroral imaging. We suggest that the large value is related to the combined effect of positive IMF B_y and a positive dipole tilt. As shown in Figure 3 of *Liou and Newell* [2010], B_y related to warping of the plasma sheet and the induced B_y from the IMF will add in the premidnight sector for this situation, possibly contributing to the large value of ΔMLT observed here.

4.2. Effect on the Aurora

Having simultaneous conjugate imaging could in principle allow us to examine the impact of the restoring symmetry process on auroral brightness. Since the restoring symmetry process is proposed to be associated with stronger BCs in the hemisphere of faster convection (corresponding to the banana convection cell, see Figure 2), this could also have an effect on auroral brightness, as the aurora seen by the UV imagers is mostly due to accelerated precipitating electrons associated with upward current regions [*Waters et al.*, 2001; *Paschmann et al.*, 2002; *Mende et al.*, 2003a, 2003b; *Dubyagin et al.*, 2003]. Comparing auroral intensities between hemispheres is by no means straightforward in this case. The two cameras are sensitive to emission lines from different atmospheric species (oxygen and nitrogen). For different seasons, the atmospheric composition varies, affecting the relative intensity between the emissions observed by VIS and WIC [*Laundal and Østgaard*, 2009]. Also, the viewing geometry and the area observed in each pixel differ between hemispheres making the direct comparison challenging. However, relative differences within the images from the two hemispheres can be identified with better confidence. An example of this is the poleward structure seen in the Southern Hemisphere from 00 to 02 MLT in Figure 4b. One can see that it has an intensity similar to the main oval in the dusk sector in the same hemisphere. The same poleward structure is also seen in the Northern Hemisphere from 21 to 23 MLT in Figure 4a. Here the intensity is less than the main dusk oval in the same hemisphere. Hence, this poleward structure appears more distinct in the Southern Hemisphere than its conjugate counterpart. This can be expected from stronger BCs associated with the restoring symmetry process we observe in the dusk cell in this region. However, we cannot rule out other mechanisms responsible for the observed asymmetry, such as parallel potential drops only in the dark hemisphere [*Newell et al.*, 1996]. To further investigate the suggested influence on BC from the restoring symmetry process, we will in the following look directly at BC signatures rather than associated auroral emissions.

4.3. Birkeland Currents Associated With the Restoring Symmetry Process

As we do not have any measurements of the BCs in the region where the plasma flows associated with the restoring symmetry process are seen in the presented event, we have made an effort to investigate the average large-scale BC distribution during the same conditions as in our event. This is done using the Active Magnetosphere and Planetary Electrodynamics Response Experiment (AMPERE) [*Anderson et al.*, 2000] with

AGU Journal of Geophysical Research: Space Physics 10.1002/2015JA022058

data from January 2010 to May 2013. Based on global sampling of the magnetic field perturbations at 700 km by the Iridium satellites, global instantaneous maps of BCs from both hemispheres are derived every 2 min based on a 10 min sliding average window [*Waters et al.*, 2001].

We present average maps of BCs from both hemispheres during conditions similar to the event presented in section 3. We select only observations having the IMF B_y and B_z values in the range that was observed during the hour prior to our event, being [5, 7] nT for IMF B_y and [−5, 0] nT for IMF B_z. The IMF values were calculated using a 50 min average (from 40 min prior to 10 min later) of the 5 min OMNI IMF to allow the closed magnetosphere to reconfigure. This long averaging interval combined with the large average value (5–7 nT) will ensure that the IMF B_y forcing has been substantial prior to the selected measurements. To ensure stability of IMF B_y, we also require that all individual 5 min values are within the range 4–8 nT for each event. Furthermore, we only include observations from the same season as the event. This is done by selecting only AMPERE observations when the dipole tilt is greater than 10°(dipole tilt is defined as positive for northern summer/southern winter). We also use the stability criteria defined by *Anderson et al.* [2008] to avoid periods when the Birkeland current pattern is rapidly changing. The stability criteria are a measure of relative overlap between consecutive patterns, quantified by a coefficient between 0 and 1. We use the same threshold value as *Anderson et al.* [2008], 0.45, but since the AMPERE data are now available at higher time resolution, our coefficients are based on current maps separated by 20 min, rather than the 1 h used by *Anderson et al.* [2008]. Selecting only stable current patterns for the averaging ensures that the current has had time to reconfigure in response to the IMF orientation. Furthermore, we only present observations from the nightside (18–06 MLT) as this is the region of interest for this paper. The number of individual current maps used in the statistics is indicated in each subplot, as well as the maximum and minimum average current density value in the premidnight and postmidnight regions separately (printed in red and blue).

The expected BCs related to the restoring symmetry process are sketched in Figure 2. It suggests that for IMF B_y positive, the Southern Hemisphere dusk side should experience a pair of upward/downward BCs at a poleward/equatorward location, respectively. This is the same polarity as the large-scale region 1/region 2 (R1/R2) pattern. Hence, one would expect to see an enhancement of both. Applying the same reasoning to a closed field line on the dawn cell, the Northern Hemisphere dawn side R1/R2 should also be enhanced during IMF B_y positive. In Figure 8a we show the average nightside BC maps from both hemispheres representing the large-scale BC pattern during the event presented in section 3 when plasma flows associated with the restoring symmetry process are seen. An apparent dawn-dusk asymmetry in current density can be seen in Figure 8a, consistent with the proposed influence from the restoring symmetry process, namely, stronger Southern Hemisphere dusk cell BCs and stronger Northern Hemisphere dawn cell BCs. The differences are strongest in the R1 currents especially in Northern Hemisphere, but also seen in the R2 currents. Also, a ~3 h ΔMLT is seen from the extent of the R1/R2 pairs between hemispheres (indicated with the black dashed line in Figure 8a), in good agreement with both auroral and nightside convection throat observations during the event. We suggest that this large average rotation of the nightside R1/R2 current pattern for these specific conditions is related to the combined effect of positive dipole tilt and positive IMF B_y as shown in Figure 3 of *Liou and Newell* [2010]. For opposite conditions (negative dipole tilt and negative IMF B_y) the average AMPERE BC pattern resemble mirror images of Figure 8a indicating a similar (but opposite) value for ΔMLT. This is shown in Figure 8c where the same IMF criteria (but opposite sign of IMF B_y) are used. We also show the case when both IMF B_y and dipole tilt are small (less than 2 nT and 5°, respectively) in Figure 8b, indicating no major dawn-dusk asymmetries in the BC strength and also no significant ΔMLT in the nightside, as expected when there is no loading (B_y) or warping of the neutral sheet (tilt). The effect on BCs of increasing versus decreasing IMF B_y was also investigated by separating the events (selected without the IMF stability criterion) into the two categories (not shown). No significant difference in the average BCs could be seen between the two categories.

In Figures 8a and 8c it is evident that signatures of the restoring symmetry process is not only seen in the immediate vicinity of the nightside convection throat but extends toward the dayside (here only shown toward 18 and 06 MLT). If these signatures are related to the restoring symmetry process, it indicates that this process is present along a large portion of the return convection region toward the dayside. From the MHD modeling study by *Tenfjord et al.* [2015], it was shown that B_y is induced also on the dayside closed field lines in a similar manner (same direction as IMF B_y). Their analysis indicated that this also affects the foot point locations, leading to a negative ΔMLT on the dayside in response to a positive IMF B_y. This suggests that the initial displaced field lines on the nightside (positive ΔMLT) will be displaced in the opposite direction

AGU Journal of Geophysical Research: Space Physics 10.1002/2015JA022058

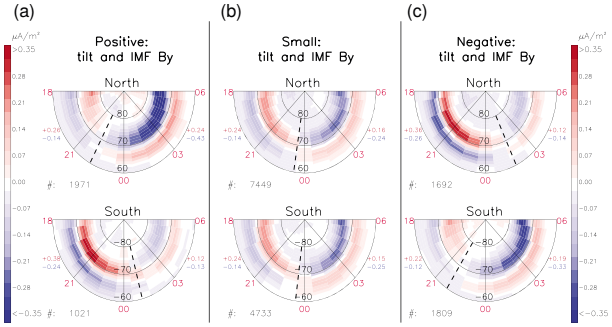

Figure 8. (a) Average maps of BC from AMPERE corresponding to the event presented in section 3 (positive IMF B_y and negative IMF B_z). Northern summer and southern winter is presented by selecting observations only when dipole tilt >10°. Dawn-dusk asymmetries in current density is seen, consistent with the expected influence from the restoring symmetry process. The number of individual current maps is indicated in each subplot, as well as the maximum and minimum average current density value both premidnight and postmidnight (printed in red and blue). The dashed black line indicate the approximate location where the R1/R2 currents change polarity, suggesting a ΔMLT ~3 h also from the AMPERE data. (b) Similar average BC maps during small (< 2 nT) IMF B_y and small (<5°) dipole tilt showing no major differences between the two hemispheres. (c) Same as Figure 8a but for negative IMF B_y and negative dipole tilt. The average dawn-dusk asymmetry and rotation of current pattern appear to be a result of the combined effect of dipole tilt and IMF B_y, consistent with observations by *Liou and Newell* [2010] and *Petrukovich* [2011]. This asymmetry is in qualitative agreement with influence from the restoring symmetry process.

(negative ΔMLT) before arriving at the dayside, pointing to a location of ~0 ΔMLT somewhere in the dusk (dawn) sector, likely centered around 18 (06) MLT. The location of 0 ΔMLT on the dusk side can be estimated for the event studied in this paper by using the observed convection velocities in the nightside convection throat region presented in Figure 7, assuming that the velocities stay constant during the restoring symmetry process. Assuming that the Southern Hemisphere foot point moves 300 m/s faster at 70° MLAT, it will take 95 min to catch up with the 3 h ΔMLT. During that time the Northern Hemisphere end will have moved 3 h in MLT at 300 m/s. This suggests a total extent of ~6 h in MLT of the restoring symmetry process, in reasonable agreement with the predicted location at ~18 MLT. Such a large extent of the restoring symmetry process is in agreement with the large region of dawn/dusk asymmetries in BCs seen in Figure 8, hence supporting the understanding of the dynamic effects of restoring magnetic foot point symmetry.

Since IMF B_y is known to lead to asymmetric foot points on closed field lines in the nightside, the restoring symmetry process might be of importance in a more general sense. It is therefore of interest to look at previous relevant work during conditions favorable for the restoring symmetry process to occur.

Green et al. [2009] used the Iridium satellites to investigate the global BC response to IMF and season. Although their selection criteria were less strict regarding the IMF B_y magnitude than we use in Figure 8, their local winter maps show the same trend as discussed for Figure 8 (but less distinct) regarding a dawn-dusk intensity asymmetry of the BC pattern related to IMF B_y. However, they did not comment on this feature.

The MFACE (model of field-aligned BCs though empirical orthogonal functions) empirical BC model based on CHAMP magnetic field data [*He et al.*, 2012] also captures a dawn-dusk asymmetry in the R1/R2 current pattern depending on IMF B_y. Although the signatures in their static model are weak [*He et al.*, 2012, Figure 3], they are consistent between hemispheres for both signs of IMF B_y.

Using ground magnetometers in the Northern Hemisphere, *Friis-Christensen and Wilhjelm* [1975] observed a stronger westward electrojet during winter conditions for positive IMF B_y compared to negative IMF B_y. They did comment on this feature, only to conclude that it was most likely not an observational bias and that it most likely was related to IMF B_y. We suggest that the increased westward electrojet they observed due to IMF B_y could be related to increased BCs in the dawn cell, consistent with the restoring symmetry process. Influence

AGU Journal of Geophysical Research: Space Physics 10.1002/2015JA022058

on ground magnetometers from BCs has recently been suggested to be important when the conductivity is low [*Laundal et al.*, 2015].

The material presented in this paper indicates that the large-scale behavior seen in the nightside by asymmetric foot points (Figure 4), asymmetric plasma flows (Figure 7), and asymmetric BCs (Figure 8a) can be explained in the framework of the restoring symmetry process as described in section 1 and by *Tenford et al.* [2015]. We emphasize that our description of the dynamic restoring symmetry process is broadly consistent with the electrostatic description of the large-scale convection pattern, where the ionospheric convection electric field can be expressed as the gradient of a potential, $\vec{E} = -\nabla\Phi$. This is expected since the average BC patterns presented in Figure 8 represent a steady state. In the electrostatic description, the ionospheric electric potential and BCs are related through $j_{\parallel} \sim \nabla^2\Phi$ when neglecting conductivity gradients. This is often further simplified to $j_{\parallel} \sim \nabla \times \vec{v}$ [*Sofko et al.*, 1995] where $\vec{v}$ is the convection field. It is therefore not surprising that the observed dawn-dusk asymmetries in the BC pattern are in good agreement with the differently shaped (different vorticity) convection cells in dawn and dusk known to be largely controlled by IMF B_y. What is new, however, is the dynamic description of how this situation is first established and then maintained. This is what we explain as the asymmetric loading process (described in the introduction and by *Tenford et al.* [2015]) and then the restoring symmetry process, affecting closed field lines in the nightside portion of the two convection cells. Hence, our main conclusion is to recognize that these presented observations are likely a result of the dynamic effects of restoring foot point symmetry on closed field lines in the nightside.

5. Conclusion

We have presented an event where a large longitudinal shift of the aurora between the hemispheres is seen. This is interpreted as evidence of closed field lines in the nightside having very asymmetric foot points associated with the persistent positive IMF B_y before and during the event. This large hemispheric shift of field line foot point, being 3 h in MLT, is to our knowledge the largest value of ΔMLT reported on from conjugate auroral imaging. Simultaneous ionospheric convection measurements in the nightside convection throat region indicate that the conjugate foot points respond to the asymmetric configuration set up by the solar wind-magnetosphere interaction by imposing faster convection in one hemisphere, consistent with the restoring symmetry process described here.

Average BC patterns during similar conditions as the event are shown. It indicates that the event under consideration experienced dawn/dusk asymmetries in the large-scale BCs consistent with the expected influence from the restoring symmetry process.

The presented material is interpreted as evidence that the asymmetric foot point, the asymmetric plasma flows, and the asymmetric BCs all can be explained in the framework of the restoring symmetry process. Hence, our main conclusion is to recognize that these presented observations are likely a result of the dynamic effects of restoring foot point symmetry on closed field lines in the nightside.

Acknowledgments
We thank S.B. Mende and the IMAGE FUV team at the Space Sciences Laboratory at UC Berkeley for the WIC data. The WIC images were processed using the FUVIEW3 software (http://sprg.ssl.berkeley.edu/image/). We thank Rae Dvorsky and the Polar VIS team at the University of Iowa for the VIS Earth data. The VIS Earth images were downloaded from NASA's Space Physics Data Facility (ftp://cdaweb.gsfc.nasa.gov/pub/data/polar/vis/vis_earth-camera-full/) and processed using the XVIS 2.40 software (http://vis.physics.uiowa.edu/vis/software/). We acknowledge the use of NASA/GSFC's Space Physics Data Facility (http://omniweb.gsfc.nasa.gov) for OMNI data. We also thank Brian Anderson and the AMPERE team for sharing their data. Operation of the SuperDARN radars is supported by the national funding agencies of the U.S., Canada, the U.K., France, Japan, Italy, South Africa, and Australia. For the ground magnetometer data we gratefully acknowledge: Intermagnet; USGS, Jeffrey J. Love; CARISMA, PI Ian Mann; CANMOS; The S-RAMP Database, PI K. Yumoto and Dr. K. Shiokawa; The SPIDR database; AARI, PI Oleg Troshichev; The MACCS program, PI M. Engebretson, Geomagnetism Unit of the Geological Survey of Canada; GIMA; MEASURE, UCLA IGPP and Florida Institute of Technology; SAMBA, PI Eftyhia Zesta; 210 Chain, PI K. Yumoto; SAMNET, PI Farideh Honary; The institutes who maintain the IMAGE magnetometer array, PI Eija Tanskanen; PENGUIN; AUTUMN, PI Martin Connors; DTU Space, PI Dr. Juergen Matzka; South Pole and McMurdo Magnetometer, PI's Louis J. Lanzarotti and Alan T. Weatherwax; ICESTAR; RAPIDMAG; PENGUIn; British Artarctic Survey; McMac, PI Dr. Peter Chi; BGS, PI Dr. Susan Macmillan; Pushkov Institute of Terrestrial Magnetism, Ionosphere and Radio Wave Propagation (IZMIRAN); GFZ, PI Dr. Juergen Matzka; MFGI, PI B. Heilig; IGFPAS, PI J. Reda; University of LAquila, PI M. Vellante; SuperMAG, PI Jesper W. Gjerloev. This study was supported by the Research Council of Norway under contract 223252 and the Peder Sather Center for Advanced Study. A.G. was supported by Science and Technology Facilities Council (STFC) grant ST/M001059/1. H.U.F. was supported by NSF through the grant GIMNASTAGS-1004736. S.E.M. was supported by the STFC, UK, grant ST/K001000/1.

References

Acuña, M. H., K. W. Ogilvie, D. N. Baker, S. A. Curtis, D. H. Fairfield, and W. H. Mish (1995), The Global Geospace Science Program and its investigations, *Space Sci. Rev.*, *71*, 5–21.

Anderson, B. J., K. Takahashi, and B. A. Toth (2000), Sensing global Birkeland currents with Iridium engeneering magnetometer data, *Geophys. Res. Lett.*, *27*, 4045–4048.

Anderson, B. J., H. Korth, C. L. Waters, D. L. Green, and P. Stauning (2008), Statistical Birkeland current distributions from magnetic field observations by the Iridium constellation, *Annales Geophysicae*, *26*(3), 671–687, doi:10.5194/angeo-26-671-2008.

Burch, J. L. (2000), IMAGE mission overview, *Space Sci. Rev.*, *91*, 1–14.

Chisham, G., et al. (2007), A decade of the Super Dual Auroral Radar Network (SuperDARN): Scientific achievements, new techniques and future directions, *Surv. Geophys.*, *28*, 33–109, doi:10.1007/s10712-007-9017-8.

Chisham, G., et al. (2008), Remote sensing of the spatial and temporal structure of magnetopause and magnetotail reconnection from the ionosphere, *Rev. Geophys.*, *46*, 1–27, doi:10.1029/2007RG000223.

Cousins, E. D. P., and S. G. Shepherd (2010), A dynamical model of high-latitude convection derived from SuperDARN plasma drift measurements, *J. Geophys. Res.*, *115*, A12329, doi:10.1029/2010JA016017.

Cowley, S. (1981), Magnetospheric asymmetries associated with the Y -Component of the IMF, *Planet. Space Sci.*, *29*, 79–96, doi:10.1016/0032-0633(81)90141-0.

Cowley, S. W. H., and W. J. Hughes (1983), Observation of an IMF sector effect in the Y magnetic field component at geostationary orbit, *Planet. Space Sci.*, *31*(1), 73–90, doi:10.1016/0032-0633(83)90032-6.

Dubyagin, S. V., V. A. Sergeev, C. W. Carlson, S. R. Marple, T. I. Pulkkinen, and A. G. Yahnin (2003), Evidence of near-Earth breakup location, *Geophys. Res. Lett.*, *30*(6), 1282, doi:10.1029/2002GL016569.

Förster, M., and S. Haaland (2015), Interhemispheric differences in ionospheric convection: Cluster EDI observations revisited, *J. Geophys. Res. Space Physics*, *120*, 5805–5823, doi:10.1002/2014JA020774.

Frank, L. A., and J. B. Sigwarth (2003), Simultaneous images of the northern and southern auroras from the Polar spacecraft: An auroral substorm, *J. Geophys. Res.*, *108*(A4), 8015, doi:10.1029/2002JA009356.

Frank, L. A., J. B. Sigwarth, J. D. Craven, J. P. Cravens, J. S. Dolan, M. R. Dvorsky, P. K. Hardebeck, J. D. Harvey, and D. W. Muller (1995), The Visible Imaging System (VIS) for the Polar Spacecraft, *Space Sci. Rev.*, *71*, 297–328.

Frey, H. U., et al. (2003), Summary of quantitative interpretation of IMAGE far ultraviolet auroral data, *Space Sci. Rev.*, *109*(1–4), 255–283, doi:10.1023/B:SPAC.0000007521.39348.a5.

Friis-Christensen, E., and J. Wilhjelm (1975), Polar cap currents for different directions of the interplanetary magnetic field in the Y -Z plane, *J. Geophys. Res.*, *80*(10), 1248–1260, doi:10.1029/JA080i010p01248.

Gjerloev, J. W. (2012), The SuperMAG data processing technique, *J. Geophys. Res.*, *117*, 1–19, doi:10.1029/2012JA017683.

Green, D. L., C. L. Waters, B. J. Anderson, and H. Korth (2009), Seasonal and interplanetary magnetic field dependence of the field-aligned currents for both Northern and Southern Hemispheres, *Ann. Geophys.*, *27*, 1701–1715.

Greenwald, R. A., et al. (1995), DARN/SuperDARN, *Space Sci. Rev.*, *71*, 761–796, doi:10.1007/BF00751350.

Grocott, A., S. Badman, S. Cowley, T. K. Yeoman, and P. Cripps (2004), The influence of IMF By on the nature of the nightside high-latitude ionospheric flow during intervals of positive IMF B_z, *Ann. Geophys.*, *22*, 1755–1764, doi:10.5194/angeo-22-1755-2004.

Grocott, A., T. K. Yeoman, S. E. Milan, and S. Cowley (2005), Interhemispheric observations of the ionospheric signature of tail reconnection during IMF-northward non-substorm intervals, *Ann. Geophys.*, *23*, 1763–1770, doi:10.5194/angeo-23-1763-2005.

Grocott, A., S. E. Milan, and T. K. Yeoman (2008), Interplanetary magnetic field control of fast azimuthal flows in the nightside high-latitude ionosphere, *Geophys. Res. Lett.*, *35*, L08102, doi:10.1029/2008GL033545.

Grocott, A., et al. (2007), Multi-scale observations of magnetotail flux transport during IMF-northward non-substorm intervals, *Ann. Geophys.*, *25*(2002), 1709–1720.

Guo, J., C. Shen, and Z. Liu (2014), Simulation of interplanetary magnetic field B_y penetration into the magnetotail, *Phys. Plasmas*, *21*(January 1998), 72901, doi:10.1063/1.4882243.

He, M., J. Vogt, H. Lühr, E. Sorbalo, A. Blagau, G. Le, and G. Lu (2012), A high-resolution model of field-aligned currents through empirical orthogonal functions analysis (MFACE), *Geophys. Res. Lett.*, *39*, L18105, doi:10.1029/2012GL053168.

Heppner, J. P., and N. C. Maynard (1987), Empirical high-latitude electric field models, *J. Geophys. Res.*, *92*, 4467–4489, doi:10.1029/JA092iA05p04467.

Khurana, K. K., R. J. Walker, and T. Ogino (1996), Magnetospheric convection in the presence of interplanetary magnetic field B_y: A conceptual model and simulations, *J. Geophys. Res.*, *101*, 4907–4916.

King, J. H., and N. E. Papitashvili (2005), Solar wind spatial scales in and comparisons of hourly Wind and ACE plasma and magnetic field data, *J. Geophys. Res.*, *110*, A02104, doi:10.1029/2004JA010649.

Kullen, A., and P. Janhunen (2004), Relation of polar auroral arcs to magnetotail twisting and IMF rotation: A systematic MHD simulation study, *Ann. Geophys.*, *22*(3), 951–970, doi:10.5194/angeo-22-951-2004.

Laundal, K. M., and N. Østgaard (2009), Asymmetric auroral intensities in the Earth's Northern and Southern Hemispheres, *Nature*, *460*(7254), 491–493, doi:10.1038/nature08154.

Laundal, K. M., et al. (2015), Birkeland current effects on high-latitude ground magnetic field perturbations, *Geophys. Res. Lett.*, *42*, 7248–7254, doi:10.1002/2015GL065776.

Liou, K., and P. T. Newell (2010), On the azimuthal location of auroral breakup: Hemispheric asymmetry, *Geophys. Res. Lett.*, *37*, L23103, doi:10.1029/2010GL045537.

Liou, K., P. T. Newell, D. G. Sibeck, and C.-I. Meng (2001), Observation of IMF and seasonal effects in the location of auroral substorm onset, *J. Geophys. Res.*, *106*(A4), 5799–5810.

Lui, A. T. Y. (1984), Characteristics of the cross-tail current in the Earth's magnetotail, in *Magnetospheric Currents*, *Geophys. Monogr. Ser.*, vol. 1, edited by T. A. Poterma, pp. 158–170, AGU, Washington, D. C.

Mende, S. B., C. W. Carlson, H. U. Frey, T. J. Immel, and J.-C. Gerard (2003a), IMAGE FUV and in situ FAST particle observations of substorm aurorae, *J. Geophys. Res.*, *108*(A4), 8010, doi:10.1029/2002JA009413.

Mende, S. B., C. W. Carlson, H. U. Frey, L. M. Peticolas, and N. Østgaard (2003b), FAST and IMAGE-FUV observations of a substorm onset, *J. Geophys. Res.*, *108*(A9), 1344, doi:10.1029/2002JA009787.

Mende, S. B., et al. (2000), Far ultraviolet imaging from the IMAGE spacecraft. 2. Wideband FUV imaging, *Space Sci. Rev.*, *91*, 271–285.

Motoba, T., K. Hosokawa, N. Sato, A. Kadokura, and G. Bjornsson (2010), Varying interplanetary magnetic field By effects on interhemispheric conjugate auroral features during a weak substorm, *J. Geophys. Res.*, *115*, A09210, doi:10.1029/2010JA015369.

Newell, P. T., C.-I. Meng, and K. M. Lyons (1996), Suppression of discrete aurorae by sunlight, *Nature*, *381*(6585), 766–767, doi:10.1038/381766a0.

Nishida, A., T. Mukai, T. Yamamoto, S. Kokubun, and K. Maezawa (1998), A unified model of the magnetotail convection in geomagnetically quiet and active times, *J. Geophys. Res.*, *103*(97), 4409–4418, doi:10.1029/97JA01617.

Østgaard, N., J. Moen, S. B. Mende, H. U. Frey, T. J. Immel, P. Gallop, K. Oksavik, and M. Fujimoto (2005), Estimates of magnetotail reconnection rate based on IMAGE FUV and EISCAT measurements, *Ann. Geophys.*, *23*, 123–134.

Østgaard, N., B. K. Humberset, and K. M. Laundal (2011a), Evolution of auroral asymmetries in the conjugate hemispheres during two substorms, *Geophys. Res. Lett.*, *38*, L03101, doi:10.1029/2010GL046057.

Østgaard, N., K. M. Laundal, L. Juusola, A. Åsnes, S. E. Håland, and J. M. Weygand (2011b), Interhemispherical asymmetry of substorm onset locations and the interplanetary magnetic field, *Geophys. Res Lett.*, *38*, L08104, doi:10.1029/2011GL046767.

Østgaard, N., J. P. Reistad, P. Tenf ord, K. M. Laundal, K. Snekvik, S. E. Milan, and S. Haaland (2015), What are the mechanisms that produce auroral asymmetries in the conjugate hemispheres?, in *Auroral Dynamics and Space Weather, Geophys. Monogr. Ser.*, edited by Y. Zhang and L. Paxton, pp. 1–34, AGU, Washington, D. C.

Paschmann, G., S. Haaland, and R. Treumann (2002), *Auroral Plasma Physics*, ISSI, pp. 100–120 pp., Bern, Switz.

Petrukovich, A. A. (2011), Origins of plasma sheet B_y, *J. Geophys. Res.*, *116*, A07217, doi:10.1029/2010JA016386.

Pettigrew, E. D., S. G. Shepherd, and J. M. Ruohoniemi (2010), Climatological patterns of high-latitude convection in the North- em and Southern Hemispheres: Dipole tilt dependencies and interhemispheric comparisons, *J. Geophys. Res.*, *115*, A07305, doi:10.1029/2009JA014956.

Pitkänen, T., M. Hamrin, P. Norqvist, T. Karlsson, H. Nilsson, A. Kullen, S. M. Imber, and S. E. Milan (2015), Azimuthal velocity shear within an Earthward fast flow âĂŞ further evidence for magnetotail untwisting?, *Ann. Geophys.*, *33*, 245–255, doi:10.5194/angeo-33-245-2015.

Reistad, J. P., N. Østgaard, K. M. Laundal, and K. Oksavik (2013), On the non-conjugacy of nightside aurora and their generator mechanisms, *J. Geophys. Res.*, *118*, 3394–3406, doi:10.1002/jgra.50300.

Richmond, A. D. (1995), Ionospheric electrodynamics using magnetic apex coordinates, *J. Geomagn. Geoelectr.*, *47*, 191–212.

AGU Journal of Geophysical Research: Space Physics 10.1002/2015JA022058

Sofko, G. J., R. Greenwald, and W. Bristow (1995), Direct determination of large-scale magnetospheric currents with SuperDARN, *Geophys. Res. Lett.*, *22*(15), 2041–2044.

Stenbaek-Nielsen, H. C., and A. Otto (1997), Conjugate auroras and the interplanetary magnetic field, *J. Geophys. Res.*, *102*(A2), 2223–2232.

Tenfjord, P., N. Østgaard, K. Snekvik, K. M. Laundal, J. P. Reistad, S. Haaland, and S. E. Milan (2015), How the IMF By induces a By component in the closed magnetosphere and how it leads to asymmetric currents and convection patterns in the two hemispheres, *J. Geophys. Res. Space Physics*, *120*, 9368–9384, doi:10.1002/2015JA021579.

Wang, H., H. Lühr, S. Y. Ma, and H. U. Frey (2007), Interhemispheric comparison of average substorm onset locations: Evidence for deviation from conjugacy, *Ann. Geophys.*, *25*, 989–999, doi:10.5194/angeo-25-989-2007.

Waters, C. L., B. J. Anderson, and K. Liou (2001), Estimation of global field aligned currents using the iridium System magnetometer data, *Geophys. Res. Lett.*, *28*(11), 2165–2168, doi:10.1029/2000GL012725.

Wing, S., P. T. Newell, D. G. Sibeck, and K. B. Baker (1995), A large statistical study of the entry of interplanetary magnetic field Y-component into the magnetosphere, *Geophys. Res. Lett.*, *22*(16), 2083–2086.

Yeoman, T. K., D. M. Wright, A. J. Stocker, and T. B. Jones (2001), An evaluation of range accuracy in the SuperDARN over-the-horizon HF radar systems, *Radio Sci.*, *36*(4), 801–813, doi:10.1029/2000RS002558.

Yeoman, T. K., G. Chisham, L. J. Baddeley, R. S. Dhillon, T. J. T. Karhunen, T. R. Robinson, A. Senior, and D. M. Wright (2008), Mapping ionospheric backscatter measured by the SuperDARN HF radars—Part 2: Assessing SuperDARN virtual height models, *Ann. Geophys.*, *26*(4), 843–852, doi:10.5194/angeo-26-843-2008.